SIMULATION OF VORTICITY DYNAMICS IN SWIRLING FLOWS, MIXING AND VORTEX BREAKDOWN

by

Jean-Claude J. Saghbini

B.S., Mechanical Engineering
University of Massachusetts Dartmouth, 1994

Submitted to the Deprtment of Mechanical Engineering
in partial fulfillment of the requirements for the Degree of

MASTER OF SCIENCE IN MECHANICAL ENGINEERING

at the

MASSACHUSETTS INSTITUTE OF TECHNOLOGY

JUNE 1996

Signature of Author: ______________________________
Department of Mechanical Engineering
June, 1996

Certified by: ______________________________
Ahmed F. Ghoniem
Professor of Mechanical Engineering
Thesis Supervisor

Accepted by: ______________________________
Ain A. Sonin
Professor of Mechanical Engineering
Chairman, Departmental Graduate Committee

Simulation of Vorticity Dynamics in Swirling Flows, Mixing and Vortex Breakdown

by

Jean-Claude J. Saghbini

Submitted to the Department of Mechanical Engineering
in partial fulfillment of the requirements for
the Degree of Master of Science in
Mechanical Engineering

ABSTRACT

The objectives of this study are to (1) gain a better understanding of the dynamics leading to a vortex breakdown in a strongly swirling axial flow; (2) determine the effect of the circulation number on the state of the post-breakdown flow; (3) clarify some aspects of the breakdown that previous experimental and numerical works have failed to identify or explain; and (4) formulate a hypothesis explaining both the axisymmetric and the non-axisymmetric dynamics of the breakdown region, and the unsteadiness that has been observed in experimental studies of this flow.

A highly efficient massively parallel implementation of the three dimensional vortex element method at high Reynolds number has been developed and a series of simulations over a wide range of circulation numbers has been obtained and analyzed for this purpose. Results indicate that depending on the circulation number, three regimes exist. In the first regime, $\Omega < 3.2$, breakdown is not observed and the vortex lines remain axially aligned in the domain. In the second regime, $3.2 < \Omega < 3.5$, breakdown occurs but then washes out and the flow regains its axial vorticity. For higher values of the circulation number, breakdown is observed to form and then drift in the flow until it reaches an equilibrium region where it remains stagnant for the length of the simulation. The stability of the breakdown is attributed to a mainly inviscid set of self-sustaining dynamics. A negative axial velocity gradient accompanied by the bulging of the filaments near the breakdown region creates a negative axial vorticity gradient. This leads to a tilting of the axial vorticity lines into the azimuthal direction, which in turn self feeds the mechanism with a negative axial velocity contribution, resulting in a stagnation point and the formation of a recirculation zone. The dynamics leading to the formation of the breakdown are axisymmetric in nature. The frequency of the internal velocity fluctuations of the bubble structure which can be related linearly to the circulation number and which match the frequency of the periodic oscillations in the wake of the breakdown, are attributed to the asymmetry of the vorticity filaments near the tail of the breakdown structure. The non-axisymmetric features near the tail of the bubble are responsible for redirecting the vorticity into the axial direction in the post-breakdown region.

Thesis Supervisor: Ahmed Ghoniem
Title: Professor of Mechanical Engineering

To “teta” Nathalie

ACKNOWLEDGEMENT

I would like to present my first “thank you” to Prof. Ahmed Ghoniem. His help and guidance were crucial to what I have accomplished at MIT over the past two years.

My reasearch benefited from discussions with Adrin Gharakhani, Marios Soteriou, Van Luu and Issam Lakkis. To Aaron Golub, my office mate: “Dude, you made it fun !!!”, and to Pat Condon: “thanks for your help and friendship”.

Beyond research, the socio-political discussions that I had with Aaron and Adrin helped me maintain a broader view on life, in an environment where technology is predominant. A very special thank you also goes to my best-friend over the past two years, Rima Askalan. Thanks for being there for me during the difficult times.

Above all, I am deeply indepted to my parents Jacques and Leila Saghbini, as well as to my brother Christian. I wouldn't have been able to make it without their unconditional love and unfailing support.

This work is partially supported by the Air Force Office of Scientific Research Grant AFOSR 84-0356. Computer support was provided by the Pittsburgh Supercomputing Center.

TABLE OF CONTENTS

1. Overview

1.1 Introduction

Forty years after the first reported vortex breakdown observation, the origin of this phenomenon is still surrounded by contradicting theories. Moreover, there are still differences in the interpretation of experimental observations attempting to provide a detailed map of the internal dynamics of the breakdown structure. This work is primarily concerned with the analysis of the vortex breakdown phenomenon in swirling flows, with the goal of shedding some light on the complex and not yet fully understood dynamics involved. The objectives are to explain the underlying vorticity dynamics of the flow; to determine the parameters characterizing the swirling flow and their effect on breakdown and mixing; and to formulate an explanation for the occurrence and sustainability of vortex breakdown showing the origin of this phenomenon.

The term “vortex breakdown” is used to characterize the abrupt change in the dynamics of a longitudinal vorticity core in a high swirl axial flow. One of the most widely reported types of vortex breakdown is the “bubble” type, in which the vortex core expands to form a stagnant bubble-like structure (figure 1). The internal dynamics of the structure are dominated by a zone of recirculating flow. Perhaps the most commonly known and generally accepted definition of a vortex breakdown is the one given by Leibovich [27]. He defines it as “a disturbance characterized by the formation of an internal stagnation point on the vortex axis, followed by a reversed flow in a region of limited axial extent” .

Vortex breakdown is manifested in a multitude of high swirl flow applications such as in swirl stabilized combustors, or in the shedding and roll-up of a vortex sheet from the leading edge of a delta wing. These two instances of vortex breakdown fall under the two major categories of vortex control: control by vortices and control of vortices, respectively (Bushnell [9]). In the first example, vorticity is used to enhance/suppress mixing in the recirculating breakdown region, thus reducing the size of the combustor or minimizing NOx formation. In the second example, which is a control of vortices case, the attempt is to control the formation of leading edge vortices and their subsequent breakdown whose effect is an abrupt change in lift and drag, accompanied by unsteadiness, poor control and buffeting (Peake and Tobak [33]).

The difficulty in the mathematical modeling, and in obtaining a complete understanding and characterization of the breakdown of the flow using laboratory experiments calls for the use of numerical methods. The results obtained form the simulations should be considered as complimentary to previous experimental and theoretical work in clarifying the features of the phenomenon and explaining the dynamics behind its occurrence.

1.2 History

The first reported occurrence of a vortex breakdown was made by Peckham and Atkinson in 1957 [34]. They observed the breakdown of a leading edge vortex above a Gothic wing. Later on, observations of leading edge vortex breakdown above a delta wing were made by Elle[12] and Werle[42] in 1960, and Lambourne and Bryer[26] in 1961. Batchelor[2] (plate 22) shows a photograph by Lambourne of a vortex breakdown over a delta wing (figure 2). A series of subsequent experimental visualizations of the breakdown phenomenon were made by Sarpkaya[37] in 1971, Faler and Leibovich[16,17] in 1977 and 1978, Escudier, Bornstein, and Zehdner[13] in 1980, and Escudier and Zehdner[14] in 1982. They reported three distinct types of the breakdown. The first two and most commonly known types are the axisymmetric bubble type (figure 1) and the spiral type (figure 3). The third type of vortex breakdown is the double helix shown in figure 4. It was observed by Sarpkaya in 1971, and it is less common that the first two. Whether or not the different forms of breakdown are fundamentally governed by the same dynamics is still an unresolved matter.

Since the time of its discovery until now, vortex breakdown has captured wide attention. Several review papers were published on the subject, e.g. Hall[21] in 1972, Leibovich[27] in 1978 and Escudier[15] in 1988. That is in addition to a book on swirling flows in 1982 by Gupta, Lilley, and Syred[20], and a chapter by Althaus et al. entitled "Breakdown of Slender Vortices" which appeared in Sheldon Green's "Fluid Vortices"[19]. There were also two conferences on vortex breakdown; the first in Aachen, Germany in 1985, and the second in Baden, Switzerland in 1987.

The following is a chronological list of some of the important manuscripts published on vortex breakdown. The list does not encompass all available literature, it is limited to the works that, in the author's view, are the most important, to offer a comprehensive look at all experimental findings and theoretical formulations.

Year	Author(s)	Title or Remarks
1971	Sarpkaya, T.	Visual analysi
1974	Sarpkaya, T.	Effect of pressure gradient, Reynolds number, and swirl number on vortex breakdown
1977	Faler, J. H. And Leibovich, S.	Visualization study of 7 mode of vortex breakdown
1978	Leibovich, S.	Survey of previous work
1978	Faler, J. And leibovich, S.	An Experimental Map of the Internal Structure of a Vortex Breakdown

1979	Garg, A.K. and Leibovich, S.	Spectral Characteristics of Vortex Breakdown Flowfields
1980	Escudier, M., Bornstein, J. And Zehdner, N.	Visualization and LDA measurements of vortex flows and breakdown
1982	Escudier, M. P. And Zehdner,N.	Dependence of the breakdown on Reynolds number and the swirl number
1983	Leibovich, S.	Vortex Breakdown and Stability: Survey and Extension
1988	Escudier, M.	Extensive survey on experiments and theoretical explanations of vortex breakdown
1990	Spall, R. And Gatski, T.	A Computational Study of the Taxonomy of Vortex Breakdown
1992	Bushnell, D. M.	Longitudinal Vortex Control - techniques and applications. (Contains an extensive references list)
1992	Brucker, C. And Althaus, W.	Internal map and velocity profiles of a bubble type vortex breakdown
1993	Breuer, M. And Hanel, D.	3D numerical simulation of vortex breakdown
1993	Brucker, C.	Internal map and velocity profiles of a spiral type vortex breakdown
1995	Althaus, W., Brucker, C., and Weimer, M.	Extensive survey of experimental, theoretical and numerical work on vortex breakdown analysis

1.3 Characteristics of Vortex Breakdown

There are three major types of vortex breakdown: the bubble type (B-type) breakdown, the spiral type (S-type) breakdown, and the double-spiral type (DS-type) breakdown. The latter is a rare occurrence that was reported by Sarpkaya [37], while the other two are the more commonly reported types. Again we re-iterate that it is still unclear whether the three observed types of breakdown are based on the same fundamental dynamics or not, and what parameters determine the demarcation between these regimes; but nevertheless, the following are some of the experimental results regarding that matter. DS-type breakdown is mainly observed for low Reynolds number and high circulation number cases (Sarpkaya[37]). For the other two types, while Sarpkaya has reported than in a divergent confined flow setting, the B-type occurs at higher Reynolds number and circulation number than the S-type, Althaus and Krause[1] have reported exactly the opposite dependence on the Reynolds number. In their experiments of swirling flow inside a constant diameter pipe, B-type breakdown occurs at a lower Reynolds number than the S-type. This contradiction could however be attributed to the fact that Sarpkaya bases the Reynolds number on the diameter of the test section, while Althaus and Krause base it on the diameter of the vorticity core, which was proven by Leibovich [28] to be a better representation of the Reynolds number. In what follows we present the main experimental characteristics and observations of vortex breakdown in strongly swirling flows.

A visual examination of what is labeled a bubble type breakdown shows the longitudinal vortex core bulging into a quasi-stationary structure (figure 5). A Particle

Tracking Velocimetry (PTV) or Laser Doppler Anemometry (LDA) analysis of the internal structure of the bubble reveals a recirculation region in which part of the flow has a negative axial velocity component with respect to the mean flow velocity (Brucker and Althaus[5]). The approach flow upstream of the breakdown can be either steady and laminar or turbulent. Downstream of the breakdown, the flow has a wakelike profile similar to the wake behind a bluff body. The velocity is minimal near the axis of the longitudinal vortex and increases as one moves radially outward. The wake behind the bubble is also characterized by a low frequency periodic oscillation not surpassing 10 Hz. Visually, the breakdown bubble appears to be axisymmetric, but Brucker and Althaus' experiments reveal that in fact the breakdown is neither axisymmetric nor steady.

A mapping of the bubble shows the presence of an azimuthal vortex structure responsible for the creation of the reversed flow; this structure however is not symmetric about the axis of the vortex core, but rather girates around it so that a time averaged portrait is symmetric. While Brucker and Althaus[5] have reported the presence of a single vortex ring inside the bubble as shown in figure 6, others such as Sarpkaya and Escudier have reported the presence of a pair of counter-rotating rings inside the bubble. The outer ring is responsible for filling the bubble, while the inner ring handles emptying it (figure 7). The difference between one and two rings also creates a difference in the induced axial velocity profile in the breakdown region. In the case of the single ring, the axial velocity near the centerline inside most of the bubble is negative. On the other hand, the twin-ringed structure induces positive velocity near the centerline. The negative axial velocity in this case is located at a distance radially outward from the centerline.

Two non-dimensional numbers are often used to characterize a swirling flow; the first being the Reynolds number defined as:

$$\mathbf{Re} = \frac{\mathbf{U_o D_c}}{\nu} \tag{1.1}$$

where $\mathbf{U_0}$ is the average inlet axial velocity, ν is the kinematic viscosity, and $\mathbf{D_c}$ is the vortex core diameter at which the inlet azimuthal velocity is maximum. The second is the circulation number Ω defined as

$$\Omega = \frac{\mathbf{\Gamma_c}}{\mathbf{U_o D_c}} \tag{1.2}$$

where Γ_c is the circulation of the vortex core. Note that the Reynolds number is based on the vortex core rather than the tube diameter. This is not the case, however, in all the experimental work done on vortex breakdown, which makes it difficult to compare between various studies. An increase in either the Reynolds number or the circulation number has the effect of shifting the breakdown structure upstream closer to the inlet of the domain as shown in figure 8. Moreover, Sarpkaya[37] has reported that at a fixed Reynolds number, an increase in the circulation number transforms a spiral type breakdown into a bubble type. In some instances, these two types were also observed to randomly interchange under steady inlet flow conditions (Sarpkaya [37]).

There are also other parameters that affect the flow. The presence of an axial pressure gradient created by an expanding confinement, for example, plays an important role in enhancing the occurrence of breakdown at low values of the circulation number. Other equally important factors shaping the flow are the velocity profile and the vorticity distribution at the inlet of the domain.

1.4 Thesis Organization

This thesis is concerned with a numerical modeling of the vortex breakdown phenomenon using a massively parallel implementation of the vortex element method in three dimensions. Chapter 2 includes a brief description the numerical scheme. It starts with the governing equations followed by the discretization and a description of the implementation of the scheme to model vortex breakdown in a swirling flow. The results of the numerical simulation are shown in Chapter 3. The results are analyzed and then compared to experimental observations and theoretical results to validate their correctness and at the same time gain more insight into the dynamics of the flow, in an effort to explain the fundamentals behind the occurrence and sustainability of the vortex breakdown. Chapter 4 describes the massively parallel implementation of the code along with its parallel efficiency characteristics and speedup over conventional serial-vector implementations. The conclusions are summarized in chapter 5, with an assessment of the adequacy of the method in capturing the dynamics of vortex breakdown, and a look at future work to shed more light on the similarities and differences in fundamental dynamics between the various observed types of breakdown.

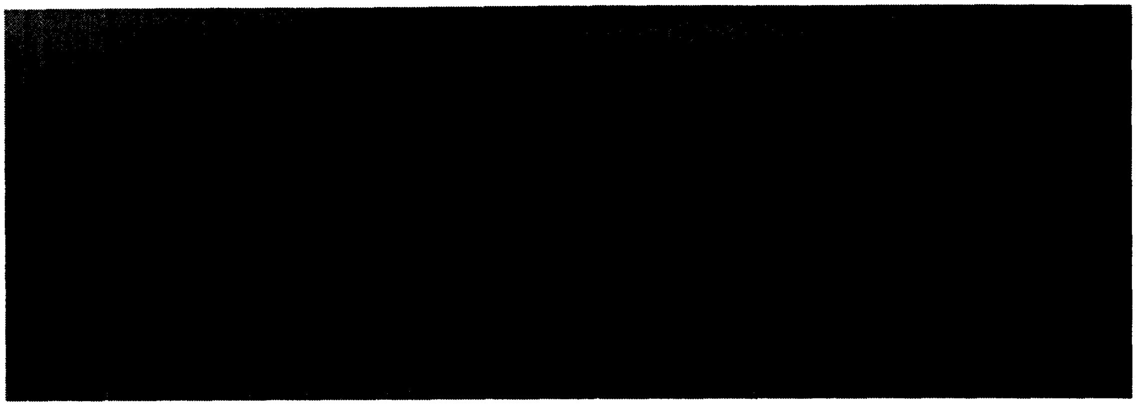

Figure 1.1: Bubble type vortex breakdown. (Faler and Leibovich, 1977).

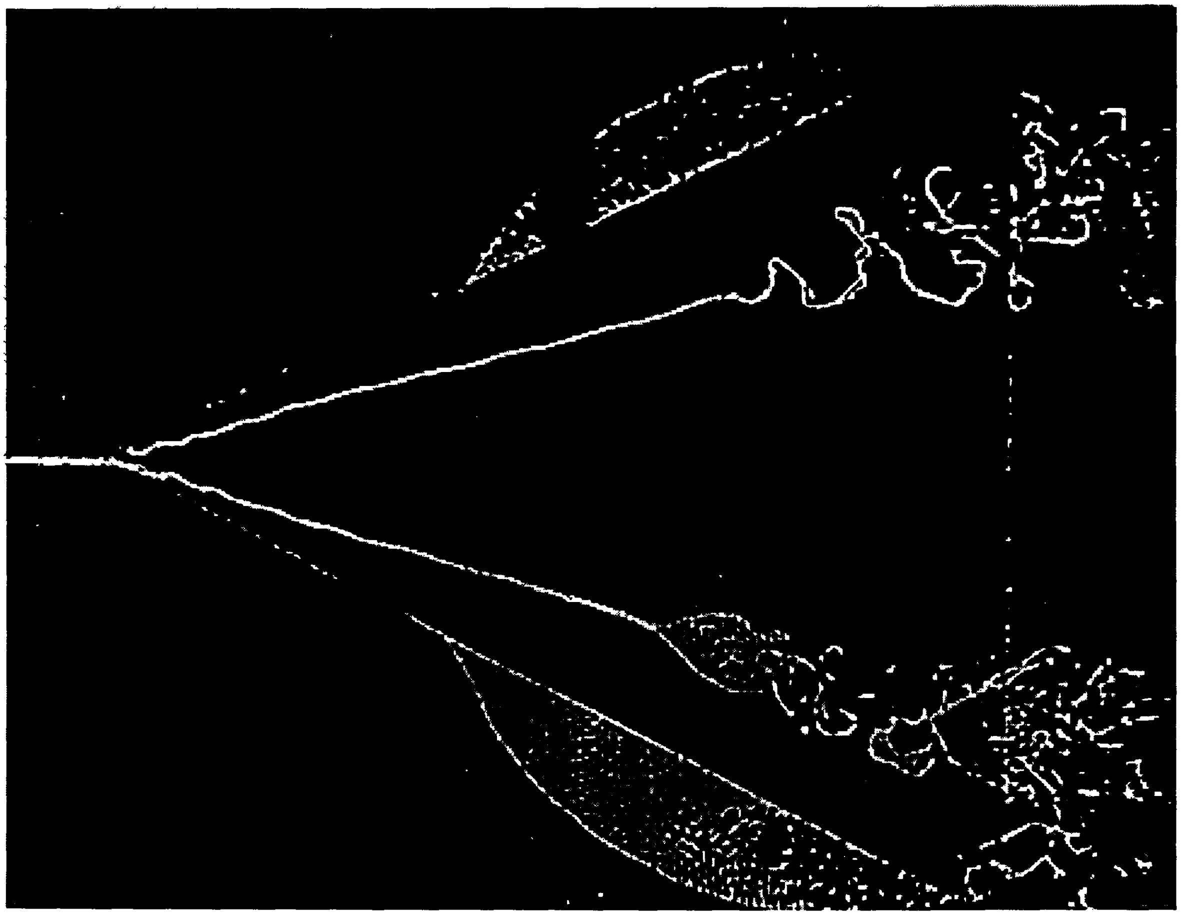

Figure 1.2: Bubble and Spiral type breakdown above a delta wing. (Lambourne and Bryer, 1961).

Figure 1.3: Spiral type vortex breakdown. (Escudier and Zehdner, 1981).

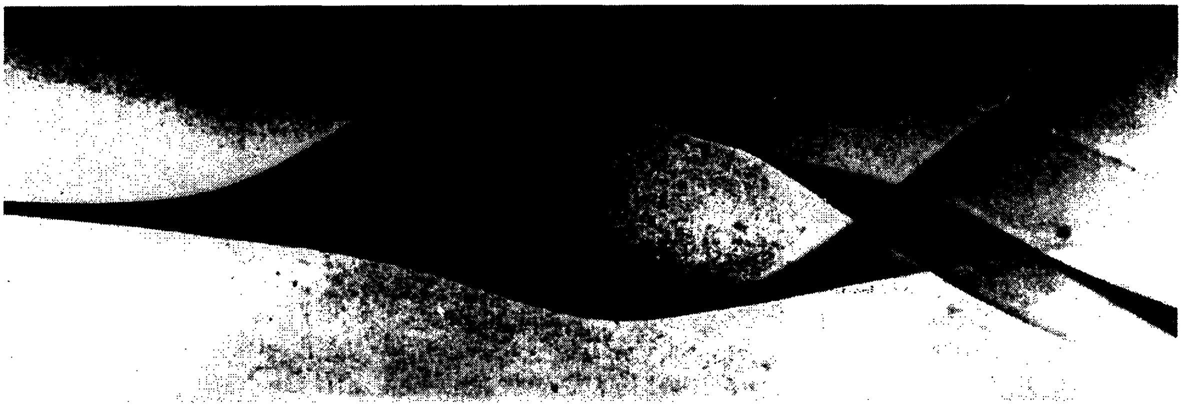

Figure 1.4: Double–Spiral type vortex breakdown. (Sarpkaya, 1971).

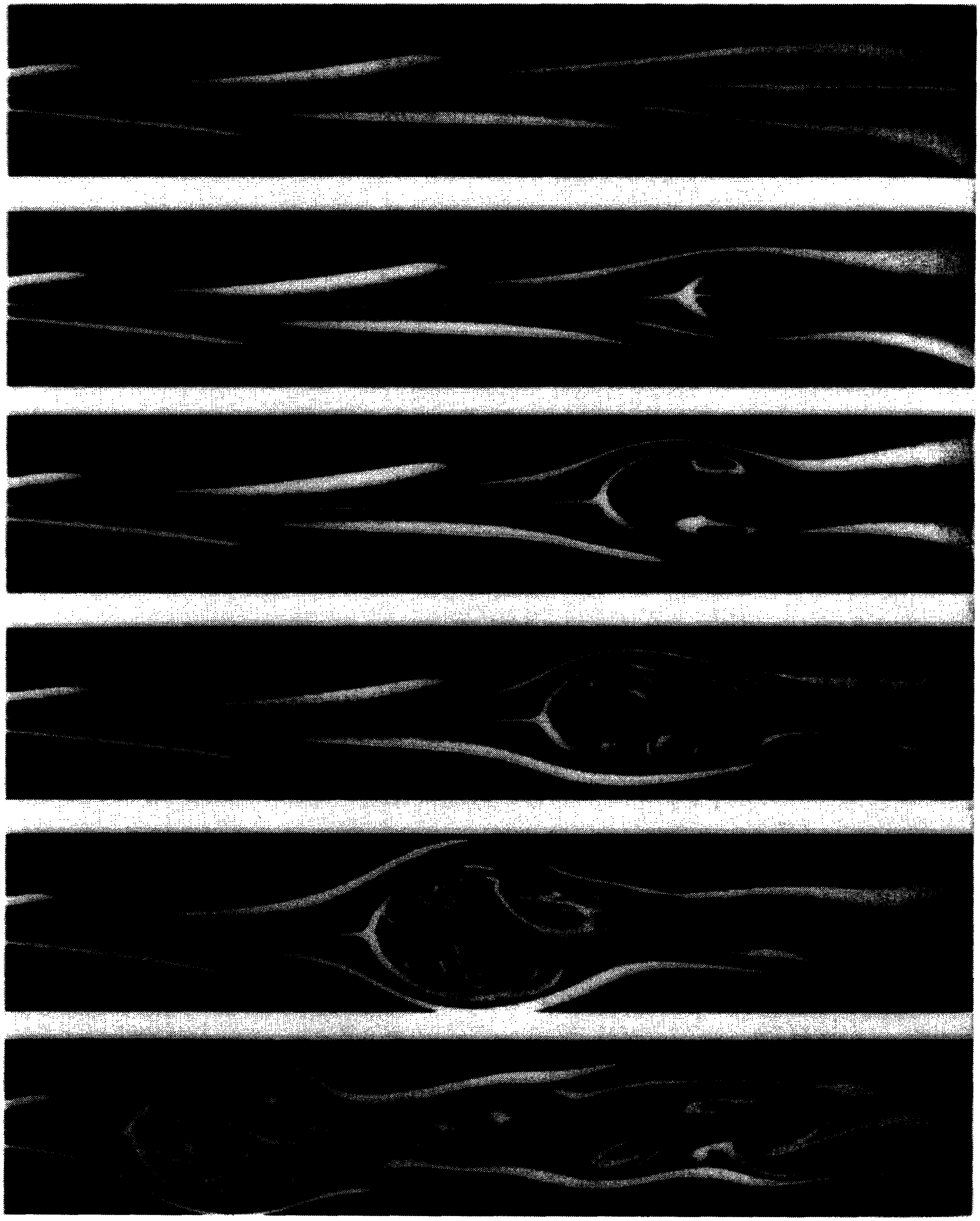

Figure 1.5: Evolution of a bubble type breakdown. (Escudier, 1988).

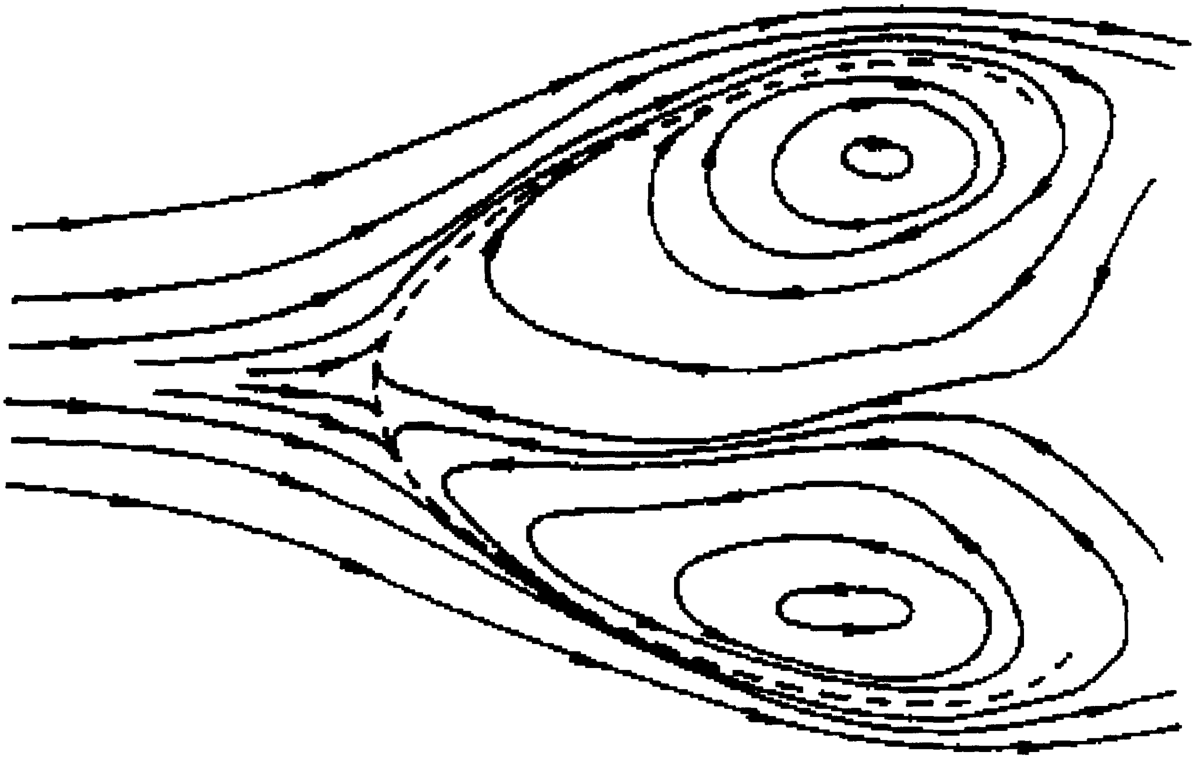

Figure 1.6: 2D streamlines showing one eddy–like structure in each half of the bubble. (Althaus, 1992).

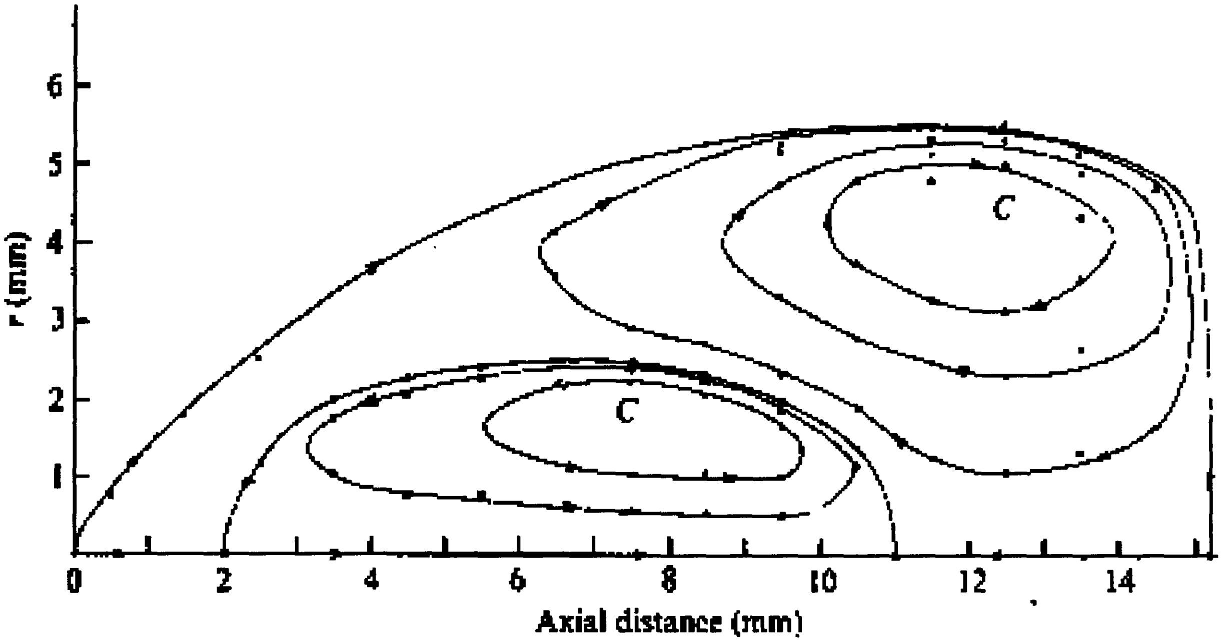

Figure 1.7: 2D streamlines showing two counter–rotating eddy–like structures in each half of the bubble. (Faler and Leibovich, 1977).

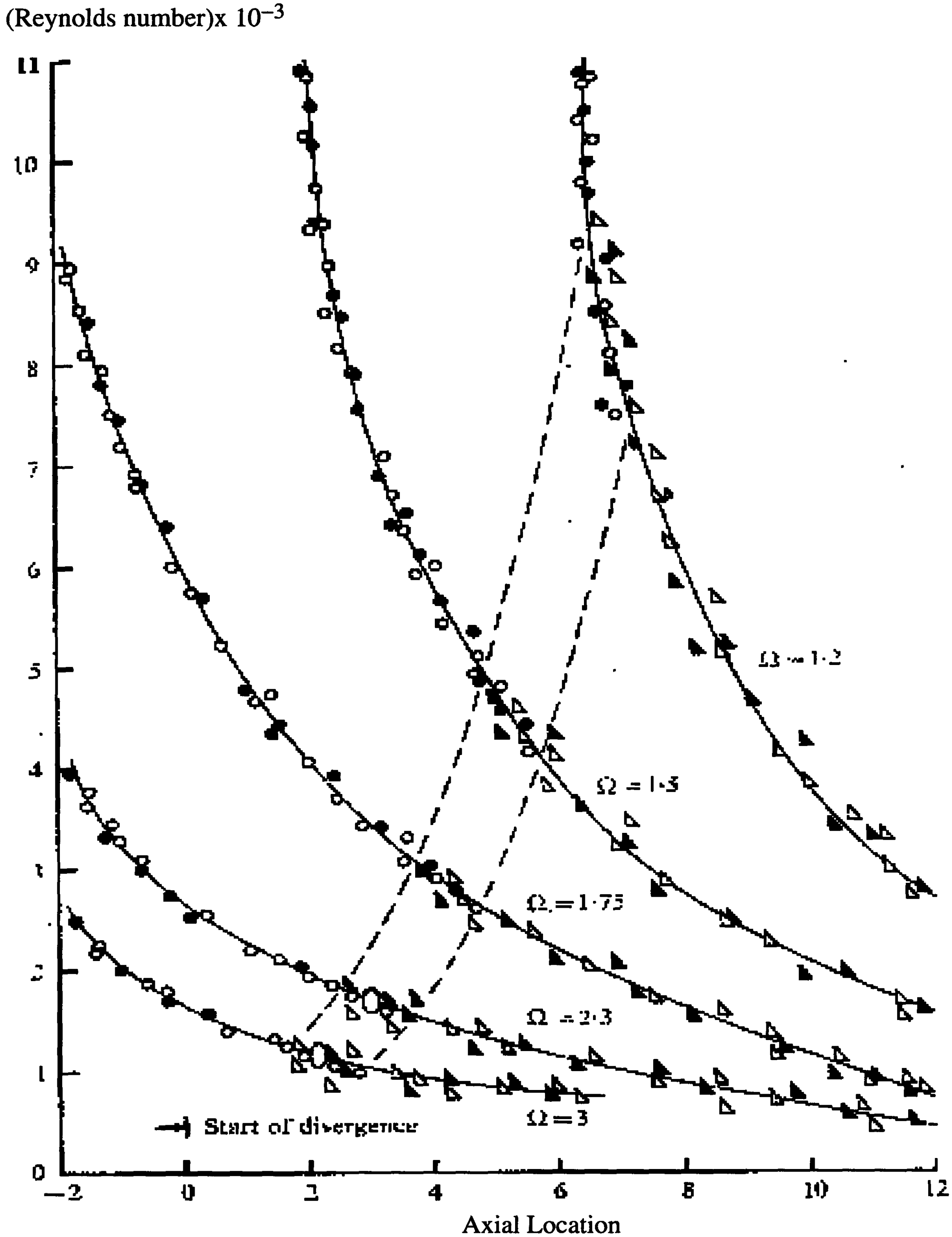

Figure 1.8: Vortex breakdown position as a function of Reynolds number and circulation number. (Sarpkaya, 1971).

2. Numerical Scheme to Simulate Vortex Breakdown

2.1 Introduction

In this chapter, we describe a numerical scheme to model the dynamics of swirling flows. The method we use is the vortex element method (VEM), attributed to the ideas of Rosenhead[36], and later used by Chorin[10,11] in the study of vortex sheets and wakes behind cylinders. The VEM, as applied in this work (Knio[23], Knio and Ghoniem[24,25]), is a three dimensional, Lagrangian, grid-free method. It is based on tracking the vorticity field in Lagrangian coordinates. The vorticity remains confined to a small portion of the flow; it is transported along particle trajectories at the inviscid limit, while being distorted and stretched by the evolving strain field. The ultimate goal is to use this computational method to analyze the vorticity dynamics of swirling flows, especially in the vortex breakdown region.

2.2 Governing Equations

2.2.1 The Transport Equation

We start with the following two equations that govern the motion of an incompressible fluid; the conservation of mass equation

$$\nabla \cdot \mathbf{u} = 0 \tag{2.1}$$

and the conservation of momentum equation

$$\frac{\partial \mathbf{u}}{\partial \mathbf{t}} + \mathbf{u} \cdot \nabla \mathbf{u} = -\nabla \mathbf{p} + \nu \nabla^2 \mathbf{u} \tag{2.2}$$

where **u=(u,v,w)** is the three dimensional velocity vector, **p** is the pressure, **t** is time, ν is the kinematic viscosity defined as $\nu=\mu/\rho$, and $\nabla=(\partial/\partial \mathbf{x}, \partial/\partial \mathbf{y}, \partial/\partial \mathbf{z})$ is the gradient operator. The vorticity is defined as the curl of the velocity vector

$$\omega = \nabla \times \mathbf{u} \tag{2.3}$$

By taking the curl of the momentum equation (2), and by using equation (1) along with the definition of vorticity (3) and the fact that the vorticity vector is solenoidal $(\nabla.\omega=\mathbf{0})$, we obtain the following vorticity transport equation:

$$\frac{\partial \omega}{\partial t}+\mathbf{u}\cdot\nabla\omega=\omega\cdot\nabla\mathbf{u}+\nu\nabla^2\omega \tag{2.4}$$

which can be reduced to

$$\frac{\partial \omega}{\partial t}+\mathbf{u}\cdot\nabla\omega=\omega\cdot\nabla\mathbf{u} \tag{2.5}$$

in the inviscid limit, where the kinematic viscosity tends towards zero. Similarly to the previous equation, Batchelor[2] shows that for an infinitesimal element $\delta\chi$ in an incompressible inviscid flow, the evolution equation is given by

$$\frac{\partial}{\partial t}\delta\chi+\mathbf{u}\cdot\nabla\delta\chi=\delta\chi\cdot\nabla\mathbf{u} \tag{2.6}$$

A comparison of equations (5) and (6) indicates that for an inviscid flow, the evolution of vorticity follows that of a material element (Helmholtz). Equation (5) itself, shows that the vorticity is stretched and tilted by the strain field $\nabla\mathbf{u}$, as it moves along particle paths.

2.2.2 Conservation of Circulation

A set of vortex lines that cross a certain surface **S** form what is called a vortex tube. The strength of the tube is obtained by integrating the vorticity over the surface **S**

$$\Gamma=\int_S \omega\cdot\mathbf{d\,S} \tag{2.7}$$

where Γ is the circulation, which characterizes the strength of the vortex tube. Using Stoke's theorem, we can write the circulation equation as

$$\Gamma=\int_{l} \mathbf{u}\cdot d\mathbf{l} \tag{2.8}$$

where **dl** is a differential element of the curve **l** bounding the surface. Along with our inviscid assumption that yielded equation (5), if we assume that **dl** is a material element, and we integrate the vorticity transport equation, we obtain

$$\frac{d\Gamma}{dt}=0 \tag{2.9}$$

Equation (9) indicates that a vortex tube in an inviscid flow conserves its circulation.

2.2.3 The Velocity Equation

The velocity vector is decomposed into three parts as follows:

$$\mathbf{u}=\mathbf{u}_{\omega}+\mathbf{u}_{\mathbf{p}}+\mathbf{u}_{\mathbf{e}} \tag{2.10}$$

where $\mathbf{u}_{\omega}$ is the vortical component obtained from the vorticity field; $\mathbf{u}_{\mathbf{p}}$ is the potential component that satisfies the boundary conditions, it is irrotational ($\nabla\times\mathbf{u}_{\mathbf{p}}=\mathbf{0}$) ; and $\mathbf{u}_{\mathbf{e}}$ is the expansion component of the velocity due to compressibility; it is also irrotational. We define a vector stream function ψ that satisfies

$$\mathbf{u}_{\omega}=\nabla\times\psi \tag{2.11}$$

Using the definition of vorticity in equation (3), we can relate the stream function to the vorticity by

$$\nabla^2\psi=-\omega \tag{2.12}$$

for which

$$\psi(\mathbf{x})=\int G(\mathbf{x}-\mathbf{x}')\,\omega(\mathbf{x}')\,d\mathbf{x}' \tag{2.13}$$

is the solution. In equation (13), **x** is the evaluation point, **x'** is the position of element **dx'** and **G(x-x')** is the Green function of the Poisson equation defined as

$$\mathbf{G}(\mathbf{x}) = \frac{1}{4\pi|\mathbf{x}|} \tag{2.14}$$

Assuming an unbounded domain in which the potential component of velocity is zero; then from the solution for the vector stream function given in equation (13), and using equation (7), we obtain the following equation for the velocity component $\mathbf{u}_\omega$

$$\mathbf{u}(\mathbf{x}) = \int \frac{-(\mathbf{x}-\mathbf{x}')}{4\pi|\mathbf{x}-\mathbf{x}'|^3} \times \omega(\mathbf{x}')\, \mathbf{dx}' \tag{2.15}$$

which is known as the Biot-Savart equation.

2.3 Discretization

At time zero, the initial vorticity field $\omega(\mathbf{x},\mathbf{0})$ is discretized into *N* vortex elements of volume **dVi** and vorticity ω_i. The distribution of vorticity on each element follows a radially symmetric core function $\mathbf{f}_\delta$. The general form of the discretization of a vorticity field ω(**x,t**) is given by the following equation:

$$\omega(\mathbf{x},\mathbf{t}) = = \sum_{i=1}^{N} \omega_i(\mathbf{t})\, \mathbf{dV}_i\, \mathbf{f}_\delta(\mathbf{x}-\mathbf{X}_i) \tag{2.16}$$

where ω_i is the vorticity of element **Xi**, and **dVi** its volume. The core function $\mathbf{f}_\delta$ is a symmetric function used to smooth the distribution of the vorticity field. The spherical core has a radius δ beyond which the vorticity decays rapidly. Four conditions are imposed on the core function. It must be non-singular at the center of the element, it must converge to the Dirac Delta function as δ goes to zero, it must decay fast enough so that its effect in the far field is equivalent to a singular point vortex, and finally, it must satisfy $\int f_\delta(\mathbf{x})\, \mathbf{dx} = \mathbf{1}$. In this work, we use a third order Gaussian core function defined as:

$$f_\delta(r) = \frac{3}{4\pi\delta^3} e^{-r^3} \tag{2.17}$$

following the work of Knio[23]. Along with the choice of the core function, the accuracy of the discretization is affected by the size of the core radius. It has already been established that the core radius must be larger than the distance between two neighboring elements. This condition is enforced by an element splitting mechanism. It is based on splitting an element in two, when its characteristic length $\delta\chi_i$ exceeds its core radius δ. Each one of the new elements has a length $\delta\chi = \delta\chi_i/2$. Core overlap between neighboring elements is therefore maintained at all times; however this approach, which is essentially a mesh refinement mechanism, results in a continuous increase in the number of elements.

To enforce the divergence free requirement of the continuous vorticity field, $\nabla\cdot\omega=0$, computational vortex filaments maintain their connectivity: the terminals of vortex elements are the same as those of their neighbors on both sides. Each element takes the form of a stick, with two end-points A and B, such that $\mathbf{A}i \equiv \mathbf{B}i\text{-}1$ and $\mathbf{B}i \equiv \mathbf{A}i\text{+}1$. The length of the element is therefore given by

$$\delta\chi_i = (\chi_B - \chi_A) \tag{2.18}$$

We can rewrite equation (16) as

$$\omega(\mathbf{x},t) = = \sum_{i=1}^{N} \Gamma_i \, \delta\chi_i \, \mathbf{f}_\delta(\mathbf{x}-\mathbf{X}_i) \tag{2.19}$$

where Γ_i is the circulation associated with element **i** and with the filament to which this element belongs. Based on that, we can write the velocity equation (15) in a discrete form (Biot-Savart) as

$$\mathbf{u}(\mathbf{x}) = -\sum_{i=1}^{N} \frac{\Gamma_i}{4\pi} \frac{(\mathbf{x}-\mathbf{X}_i) \times \delta\chi_i}{|\mathbf{x}-\mathbf{X}_i|^3} (1-e^{-r^3}) \tag{2.20}$$

where

$$\mathbf{r} = \frac{|\mathbf{x} - \mathbf{X}_i|}{\delta}$$

In the next section, we describe the time stepping of the second order time integration (Knio[23]) and the use of the above discretization in the VEM algorithm.

2.4 Time Stepping

Equation (18) shows that the length of element **i** is the difference in the coordinates of points **Ai** and **Bi**, which are the end-points of the element. Thus, even though an element **i** does not have actual (computational) coordinates to its center, we can track its motion through its two end-points by taking the average of their location. In the following equations, the subscript **i**, even though it refers to the element itself, could be assumed to refer to any one of the element's end-points.

In our implementation of the VEM, we use a second order time integration (Knio[23]) to track the motion of the vortex elements - or their end points -:

$$\mathbf{X}_i^* = \mathbf{X}_i(t) + \mathbf{u}(\mathbf{X}_i,t)\,\Delta t \tag{2.21}$$

$$\mathbf{X}_i(t+\Delta t) = \mathbf{X}_i(t) + \frac{\mathbf{u}(\mathbf{X}_i,t) + \mathbf{u}(\mathbf{X}_i^*,t)}{2}\,\Delta t \tag{2.22}$$

The algorithm for the code is therefore the following:

```
Begin
    Loop j=1,Nc
        $\mathbf{u}(\mathbf{x}_j,t) = -\sum_{i=1}^{N} \frac{\Gamma_i}{4\pi} \frac{(\mathbf{x}_j - \mathbf{X}_i) \times \delta\chi_i}{|\mathbf{x}_j - \mathbf{X}_i|^3} \left(1 - e^{-\left(\frac{|\mathbf{x}_j - \mathbf{X}_i|}{\delta_i}\right)^3}\right)$
        $\mathbf{x}_j^* = \mathbf{x}_j(t) + \mathbf{u}(\mathbf{x}_j,t)\,\Delta t$
    EndLoop

    Update the vorticity of the elements

    Loop j=1,Nc
```

```
            $u(x_j^*,t) = -\sum_{i=1}^{N} \frac{\Gamma_i}{4\pi} \frac{(x_j^*-X_i) \times \delta\chi_i}{|x_j^*-X_i|^3} (1-e^{-(\frac{|x_j^*-X_i|}{\delta_i})^3})$
            $x_j(t+\Delta t) = x_j(t) + \frac{u(x_j,t) + u(x_j^*,t)}{2} \Delta t$
        EndLoop

        Update the vorticity of the elements
        $t=t+\Delta t$
    Goto Begin
```

Note than N is the number of vortex elements in the computational domain, and Nc is the number of active points, end points, by which we track the motion of the vortex elements. Because element connectivity is maintained within a vorticity line, the number of active points on a filament (vorticity line) exceeds by one the number of elements on that filament. If we define *Nfil* as the number of filaments in the computational domain, then the number of active points Nc can be given by $Nc = N + (1*Nfil)$.

2.5 Mesh Refinement

A good study of mixing in swirling flows requires an accurate modeling of the vortex breakdown region. Experimental evidence suggests that one form of vortex breakdown involves the formation of a recirculation zone (bubble type breakdown) in which negative axial velocities near the axis of the vortex core are encountered. Inside this recirculation zone, the flow is highly convoluted. The vortex filaments are therefore expected to be subjected to a high degree of strain that continuously stretches the vortex elements. To maintain the accuracy of the scheme, a mesh refinement mechanism is used. It consists of splitting an element in two when its length, along the filaments direction, exceeds a certain characteristic value. This value is set to be the size of the core radius of the element, thus ensuring a continuous core overlap between any two neighboring elements. When a parent element **i** of length $\delta\chi_i$ and vorticity ω_i is split in two, each one of the child elements will be of length $\delta\chi = \delta\chi_i/2$ as shown in figure 1. The circulation value associated with the filament at hand is constant, and therefore each child element will have the same value of vorticity that the parent element had, $\omega = \omega_i$, thus satisfying both the conservation of mass and the conservation of momentum constraints. It is important to note that this scheme results in a continuous increase in the number of elements N needed to model the flow. The rate of increase dN/dt is proportional to the number of elements, which makes N an exponential function of time (figure 2)

2.6 Slightly Viscous Flows

The implementation of the three dimensional vortex element method in an inviscid flow model results in a rapid increase in the number of elements as the flow evolves. The reason for that is the fact that elements connectivity is maintained and an accurate solution can only be obtained if the mesh refinement mechanism described in the previous section is implemented. The absence of vorticity diffusion from the flow increases the convolution of the flow and subsequently the stretch of the vorticity filaments, which in turn increases the number of computational elements in the domain. Moreover, totally inviscid flows are not realizable in reality because viscous diffusion cannot be completely eliminated. A scheme is implemented to capture some of the effects of diffusivity in the flow. The flow model remains a high Reynolds number model, but closer to experimental flows than the inviscid model. Another advantage of the slightly viscous model is that it ensures the ability to run the simulation to later stages within our computational capabilities.

The implementation of the vorticity diffusion in three dimensions is based on a scheme introduced by Leonard and Chua[30]. A large eddy simulation is performed by calculating the effect of the subgrid-scale eddies on the large scale structures in the flow. This is accomplished through a non-linear core expansion mechanism following the equation given by Leonard and Chua:

$$\frac{d\delta^2}{dt} = 4\nu_{SGS} - \delta^2 \frac{1}{\omega}\frac{d\omega}{dt} \qquad (2.23)$$

where $(1/\omega)(d\omega/dt)$ is the local vorticity stretching rate, and ν_{SGS} is the subgrid-scale viscosity defined as

$$\nu_{SGS} = \max\left[0, C\delta^2 \frac{1}{\omega}\frac{d\omega}{dt}\right] \qquad (2.24)$$

where C is a constant. Note that equation (24) is similar to the Smagorinsky model used in finite difference calculations for large-eddy simulations. The core expansion model of equation (23) is governed by the same general parameters as the fundamental viscous diffusion of a line vortex (Sherman[39]) :

$$\delta^2 = \frac{\nu}{A} + (\delta_o^2 - \frac{\nu}{A})e^{-At} \qquad (2.25)$$

where δ_o is the initial core radius at t=0, ν is the kinematic viscosity of the fluid, and **A** is the local stretching rate. Taking the derivative of equation (25) with respect to time yields:

$$\frac{d\delta^2}{dt} = \nu e^{-At} - A\delta_o^2 e^{-At} \qquad (2.26)$$

A comparison between equations (23) and (26) shows similarity. In both cases, the core expansion is governed by a combination of viscous and inviscid effects represented by the two terms on the right-hand side of the equations. The first term is the viscous diffusion contribution to the core expansion. In equation (23), it is proportional to the subgrid-scale viscosity which in turn is dependant on the local vorticity stretching rate and a constant **C** to be determined later. The second term on the right-hand side of the core expansion equations represents the inviscid change in core size due to the local stretching rate. This term competes with the viscous diffusion term and has the effect of concentrating the voriticity.

The constant **C** is chosen semi-arbitrarily. If **C** is too low, diffusion is very slow and the flow behavior is similar to the inviscid case. On the other hand, too high of a value leads to high diffusivity and suppresses some of the dynamics of the flow. In our model, we chose a value of **C** equal to 0.5.

2.7 Modeling of a Swirling Axial Flow

We model a three dimensional axial swirling flow, where the x-axis is in the axial direction of the flow while the y-axis and the z-axis are in the other two transverse directions. The vorticity field is represented by **NL** concentric vorticity sleeves, each made of **NR** vortex filaments distributed symmetrically around the periphery of the sleeve. Figure 3 is a schematic of the filaments at the inlet of the domain. The vorticity core is discretized into three sleeves. The innermost sleeve is concentric with the voriticty center and consists of a single filament, while the others have $2\pi R_s/(0.8\delta_o)$ filaments each, where $\mathbf{R_s}$ is the radius of the sleeve and δ_0 is the initial core radius of the elements as they enter the domain. This ensures that the distance between two adjacent filaments on a particular layer is less than the initial core radius of the elements, which automatically enforces core overlap of the corresponding elements. The initial length of the elements as they enter the domain is $\delta\chi=\mathbf{0.8}\delta_0$. This also ensures core overlap between two adjacent elements pertaining to the same filament.

2.7.1 Domain Conditions and Inlet

We model an unconfined vortex flow, comparable to a confined flow in which the confinement has minimal vortical effect on the behavior of the vortex core and its subsequent breakdown. The vortex core is therefore a slender core compared to the diameter of the pipe (Althaus, Brucker and Weimer[19]). Leibovich[28] argues that the Reynolds number should be based on the vortex core diameter rather than on the diameter of the pipe; which undermines even more the importance of the actual diameter of the test tube, as long as it is large enough for the slender vortex approximation to hold.

The inlet axial velocity distribution has a plug flow profile, i.e. the velocity is constant, $\mathbf{U_0}$, independent of the radial and azimuthal location. $\mathbf{U_0}$ is taken as the reference velocity scale while $\mathbf{D_0}$, the diameter of the outer sleeve, is taken as the reference length scale. Based on that, the diameter of the inner sleeve is equal to 0.5, the radius δ_0 of the spherical core is 0.25, and the initial length of the filaments in the domain is chosen to be equal to 10.5. The time step $\Delta t=0.05$ is determined from the convergence test shown in figure 4.

The inlet azimuthal velocity profile, shown in figure 5, corresponds to solid body rotation. A set of fixed vortex filaments, similar to those that enter the domain, extend axially from x=0 to negative infinity. These filaments model the vorticity carried by the flow upstream of the domain (test section), and its effects on the elements in the domain. Figure 6 is the result of a convergence test to determine the required length of these filaments in the numerical simulation. In our model, the length of these filaments is set to 6, which results in an error of 0.4% from the ideal solution in which they extend to infinity.

The strength of the vortex filaments at the inlet of the domain is characterized by the circulation number Ω defined as

$$\Omega = \frac{\Gamma_c}{U_0 D_c} \tag{2.27}$$

where Γ_c is the total circulation of the vortex core, and $\mathbf{D_c}$ is its diameter. The diameter of the vortex core is defined as the diameter at which the azimuthal component of velocity reaches its maximum (figure 5); this results in a value of $\mathbf{D_c/D_0}$ equal to 1.25. The circulation value associated with each individual filament is therefore

$$\Gamma_f = \frac{\Gamma_c}{\sum_{i=1}^{NL} NR_i} \tag{2.28}$$

where **NR** is the number of filaments on a certain vorticity layer, and **NL** is the number of layers in the flow.

New elements entering the domain get appended to the beginning of their respective filaments. The inlet location of these elements is not fixed. Their radial position is equal to the radius of the sleeve they belong to, but their azimuthal position changes constantly. After a certain time, the first element of each filament would have moved both in the positive x direction as well as azimuthally. When the x coordinate of the A point of an element has exceeded $\mathbf{0.8\delta_0}$, a new element is inserted. The B point of the new element is the same as the A point of the previous one, to ensure connectivity. The A point of the new element is located at a radial location equal to the radius of the sleeve it belongs to. The theta coordinate is that of the previous element, while the x coordinate is zero. This scheme ensures that the elements entering the domain are carrying vorticity purely in the axial direction.

2.7.2 Exit Boundary Condition

There is no explicit boundary condition implemented at the exit of the computational domain apart from an element deletion scheme to reduce the number of elements. Computationally, the domain extends to infinity. As the filaments are being stretched by the evolving strain field in the domain, the cores of individual vortex elements grow, following equation (23), because of viscous dissipation. The core radius of an element can reach the point where the diffused vorticity of the element has a minimal effect on the rest of the flow. A subsequent elimination of this element from the flow is hence expected to have a minimal effect on the dynamics of the flow. Based on this observation, an element deletion scheme, called CLIP10, is implemented. Because of the constraint of maintaining connectivity between elements, individual elements cannot be removed. Instead an entire sets of elements representing a continuous filament is removed. The filaments are traversed; whenever an element whose core radius has exceeded 10 times its initial radius is encountered, all the elements starting from this element up to the end of the filament are removed from the domain. This scheme extends the limit on the size of the domain and the length of the run by more than an order of magnitude by considerably reducing, in real time, the number of elements required to model the flow, while minimally affecting the dynamics of the flow near the region of interest. Figure 7 shows a comparison after 200 time steps between a run where CLIP10 is implemented and another where it is not. There is a remarkable similarity between the two flows, confirming our early assertion that removing "aged" elements has a negligible effect on the flow. The plot in figure 8 presents the error obtained, 200 time steps after implementing CLIP10, in the calculation of axial and azimuthal velocities along a part of the domain. In the region of interest, the breakdown region, CLIP10 clearly maintains an accurate solution. The spikes in figure 8 correspond to zero velocity locations, where the velocity can numerically vary by an order of magnitude, but for all practical purposes remains zero.

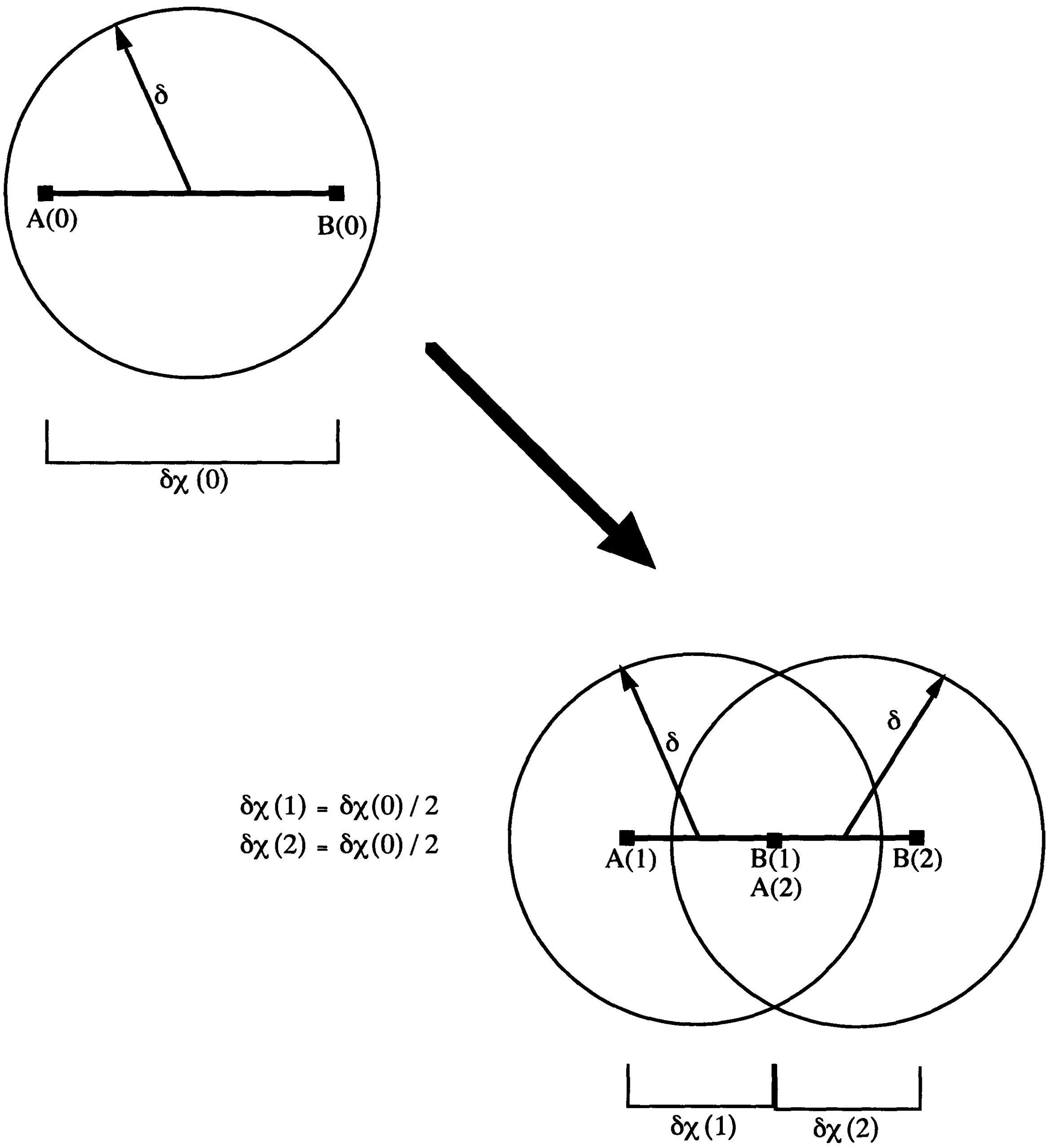

Figure 2.1: Implementation of the element splitting mechanism to maintain core overlap between neighboring elements.

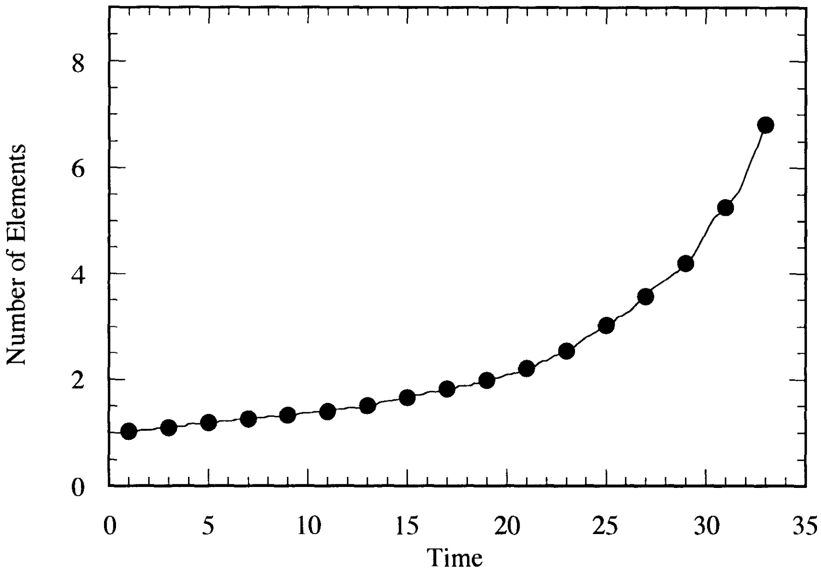

Figure 2.2: The total number of vortex elements in the computational domain, as a function of time. The number of elements is normalized by its original value at t=0

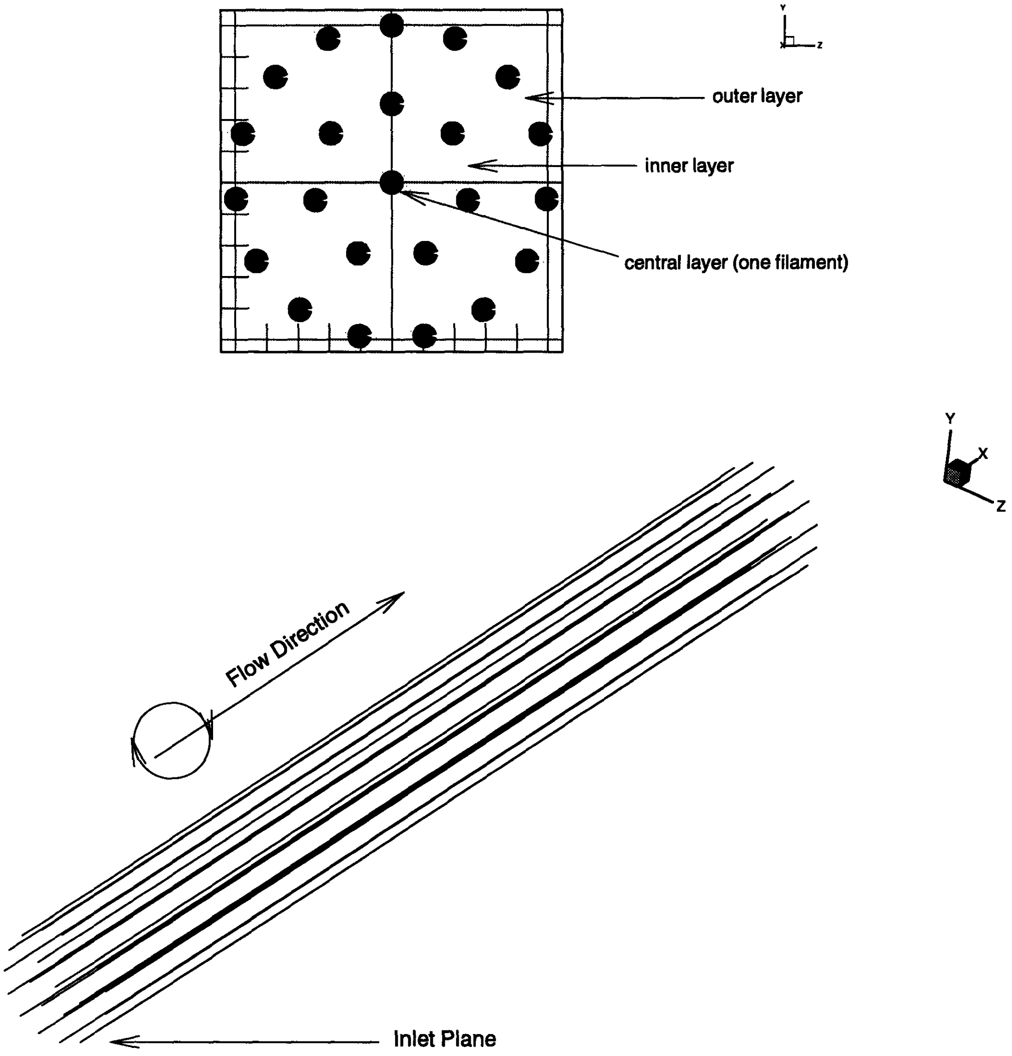

Figure 2.3: Two-dimensional and three-dimensional visualizations of the vorticity layers and the vorticity filaments at t=0.

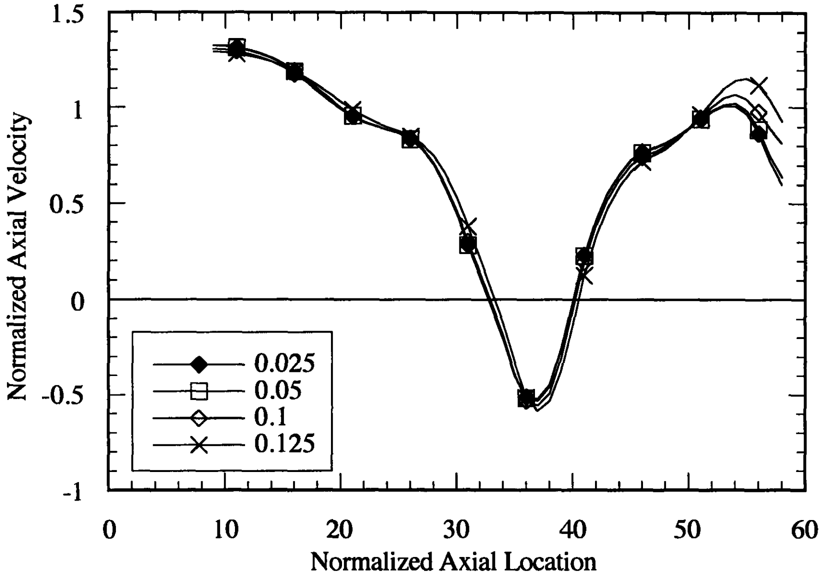

Figure 2.4: Comparison of centerline velocity profile for runs with different time step size: 0.025, 0.05, 0.1, and 0.125.

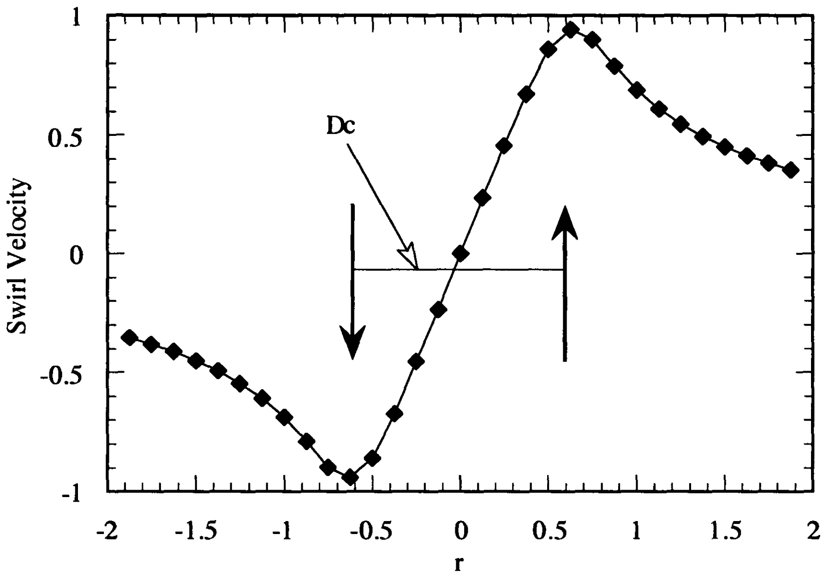

Figure 2.5: Inlet tangential velocity profile. (r represents the radial location)

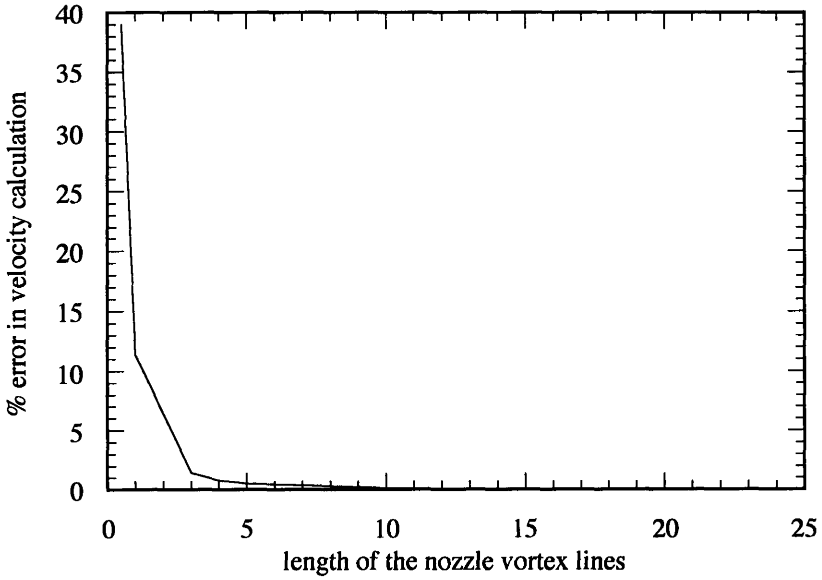

Figure 2.6: Plot of the % error in the velocity calculation versus the non-dimensional length of the vortex lines that form the nozzle.

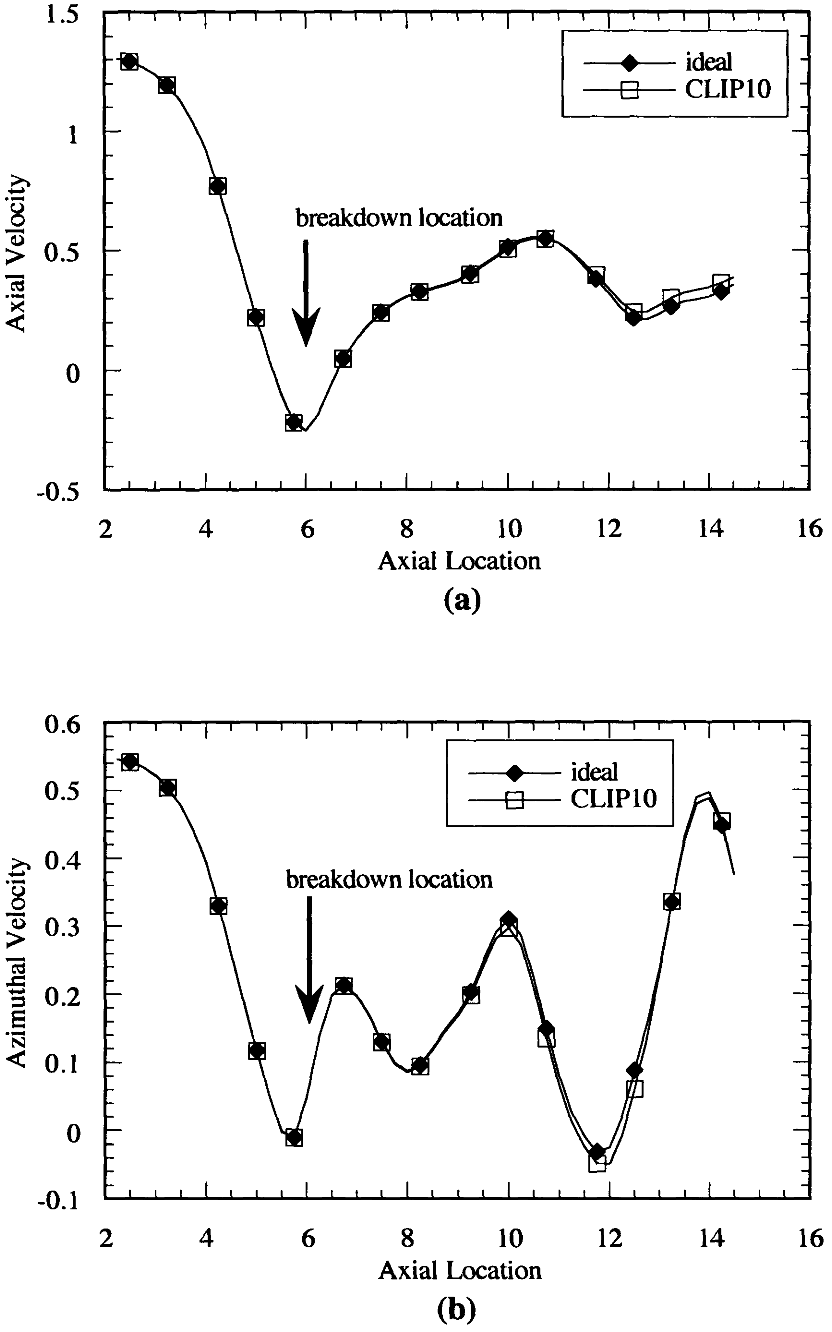

Figure 2.7: Comparison between the velocity profiles of a run in which CLIP10 was not implemented and another in which it was. The velocities are computed on a set of points, 200 time steps after the implementation of CLIP10.
(a) Axial velocity comparison.
(b) Azimuthal velocity comparison.

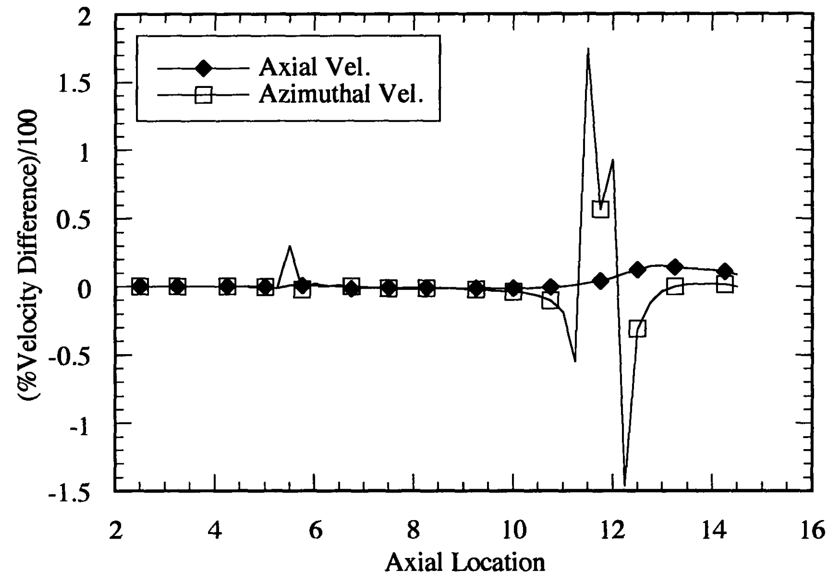

Figure 2.8: Difference in axial and azimuthal velocities between the "ideal" case and the "CLIP10" case of figure 2.7.

3. Vortex Breakdown Results and Discussion

3.1 Introduction

The objectives of this work are to: (1) gain a better understanding of the dynamics leading to vortex breakdown in strongly swirling flows; (2) determine the effect of the circulation number on the behavior of the breakdown region and the post-breakdown flow in terms of the bubble size, the bubble location, and the wake fluctuations; (3) clarify some aspects of the breakdown that previous experimental and numerical works have failed to either identify or explain; and (4) formulate an explanation for both the axisymmetric and the non-axisymmetric dynamics of the breakdown region, and the resulting unsteadiness that was observed in experimental studies. A series of simulations over a wide range of circulation numbers has been performed in order to achieve these objectives.

This chapter is divided into three major sections. In the first section, the main characteristics of the breakdown, including velocity profiles, velocity fluctuations, and dependence on the circulation number, are examined. The next section involves a three-dimensional study of the internal structure of the breakdown zone using a map of the continuous vorticity field as well as the discrete field represented by the vortex filaments. This study encompasses both axisymmetric and non-axisymmetric features of the breakdown. The last section includes an explanation for the occurrence of vortex breakdown while stressing the point that the fundamental dynamics leading to breakdown are axisymmetric in nature, and that non-axisymmetric features only affect the post-breakdown region.

3.2 Characteristics of the Vortex Breakdown

3.2.1 Onset of the Breakdown

Figures 1, 2, and 3 show the startup of a swirling flow from an initially axial vorticity distribution until the formation of a steady vortex breakdown. The value of the circulation number for this run is $\Omega=3.52$, as defined in equation (2.25). In examining figure 2, however, it is important to note that what is shown is a two dimensional projection of a longitudinal cut of the flow. The cut has a thickness of 0.2 and is centered around the midplane. The vectors in the figure represent the two dimensional velocity of the elements encompassed by the cut. This figure gives a qualitative representation of the behavior of the flow, and more specifically of the dynamics inside the breakdown structure. A different portrait of the flow in the midplane is given by figure 3 in which the velocity is directly computed, using the Biot-Savart law, on a set of fixed computational grid points.

At time step zero, a negative axial vorticity gradient is present due to the initial discretization of the flow field. As described in chapter two, the vorticity lines are semi-infinite, ending at a certain location in space downstream from the inlet of the domain. This axial vorticity gradient is also equivalent to a negative axial gradient in the azimuthal velocity of the elements. As the flow starts to develop from an initial stage where all the vorticity is carried by the vortex lines in the axial direction, the tips of the vortex lines get tilted azimuthally in the direction opposite to the rotation of the flow as shown at t=4.0 in figure 1. This tilting of the axial vorticity creates an azimuthal component of vorticity with a negative axial velocity contribution. The azimuthal vorticity created also results in a negative axial velocity gradient and in the bulging of the incoming elements which in turn slows down their rotation and self feeds the mechanism of bulging-slowdown-tilting. As the flow develops, more of the axial vorticity gets transformed, by filament tilting, into azimuthal vorticity. This contributes to the increase in magnitude of the adverse axial velocity component, which results in a stagnation point on the centerline axis of the flow, and to the subsequent formation of an axisymmetric bubble-like structure characterized by an internal recirculation zone as shown at t=15.0 in figures 2 and 3. The bubble grows axisymmetrically with time; it then picks up a perturbation and loses its symmetry (Figures 2 and 3, t=25.0) but maintains its main characteristics as far as the counter-rotating two dimensional eddy-like structures which cause the recirculation . Figure 3 at t=60.0, 85.0, and 100.0 clearly shows this asymmetry as well as the counter-rotating eddies that were reported by Brucker and Althaus[5] from experimental PTV measurements. Note that the asymmetry is mainly apparent near the tail of the breakdown and in the wake of it, while the nose part maintains its global symmetry throughout the simulation. With time, the bubble drifts in the flow until it reaches an equilibrium position around which it remains stationary for the duration of the simulation. Figures 1, 2, and 3 show a flow behavior that is in good agreement with experimental observations (Sarpkaya[37], Escudier and Zehdner [14], Faler and Leibovich[16]). A longitudinal cut of the flow clearly shows the bulging of the vortex core as well as the presence of a very well defined stagnant bubble-like structure. The stagnation of the centerline filament is visible in figures 2 and 3 starting from t=6.0. This point will hereafter be referred to as the front stagnation point.

3.2.2 Filling and Emptying of the Bubble

Another important observation can be made by looking at the cross-sectional cut of the flow in figures 2 and 3 at time t=85 for example. The velocity field and shape of the breakdown agree with both Sarpkaya's [37], and Faler and Leibovich's [16] experimental observations regarding the filling and emptying of the bubble. They noted that the filling and emptying of the bubble happen at two diametrically opposite locations, and that the rear of the bubble is tilted so that the filling location is upstream of the emptying location as shown in figure 1.1. The results in figures 2 and 3 offer an explanation for that observation. At t=15.0, the breakdown is still developing and the bubble has not reached its stationary state. The symmetric cross sectional velocity field clearly shows the filling and emptying process. The filling occurs near the centerline between the two-dimensional eddies, while the emptying happens at the periphery, near the tail of the bubble. In the asymmetric stage when the bubble has reached stability (t=85.0), the dynamics do not seem to contradict the above noted observations. The filling of the bubble still takes place between the two eddies, but because of the asymmetry and the size difference of the eddies, it is more apparent on one side of the bubble near the larger eddy. Similarly, the emptying still occurs around the periphery but is more apparent near the weaker eddy, at a location diametrically opposite from the filling side. This analysis shows that even though the filling-emptying process of the bubble appears to by asymmetric, it is not fundamentally based on asymmetric dynamics. A further analysis of the symmetry of the breakdown region and of the nature of the asymmetric instabilities and the extent of their role in shaping the flow behavior is presented at the end of this chapter.

3.2.3 Note on the Sense of the Spirals

It is interesting to notice, from the three dimensional visualization of the flow in figure 1, that the direction of winding of the filaments is clearly opposite to that of the rotation of the flow. Moreover, the winding of the wake behind the bubble is also opposite to the rotation. This observation is attributed to the negative axial gradient in azimuthal velocity, which forces elements downstream to rotate at a slower rate than the elements upstream and results in the observed winding. The above analysis can be used to shed some light on some earlier observations made by Escudier and Zehdner[14] regarding the spiral type breakdown. They also noted that the winding of the spiral was opposite to the rotation of the flow while the entire spiral structure was in fact rotating with the flow. This point had caused some controversy between Sarpkaya [37] and Faler and Leibovich's [16] observations on one hand, and Escudier's observations on the other. It can however clearly be thought of as an effect of the same dynamics that produced the counter-winding of the individual filaments, observed in figure 1.

3.2.4 Velocity Profiles

Other important aspects to examine in order to get a better understanding of the dynamics of the flow are the axial and azimuthal velocity profiles in the domain. Figure 4 shows the distribution of these two components of velocity on a two dimensional longitudinal cut of the flow spanning the pre-breakdown region, the inside of the bubble-like structure, and the wake of the breakdown. The velocity profiles inside the bubble are in good agreement with the experimental findings of Brucker and Althaus[5] obtained experimentally from Particle Tracking Velocimetry (Figure 5). In the approach flow, upstream of the breakdown, the axial profile is plug-flow like, while the azimuthal velocity profile is a solid body rotation inside the vorticity core and slowly decays outside of it. As the breakdown is approached, the centerline axial velocity decreases until it reaches a clearly defined stagnation point at the nose of the bubble. Past that stagnation point, the centerline velocity takes negative values inside the bubble, which creates the recirculating flow reported earlier. Similarly, the azimuthal velocity profile inside the bubble shows a slowdown in rotation. The increase in negative axial velocity and the decrease in tangential velocity can be related to the same phenomenon. They are caused by a change of direction of the vorticity lines at the nose of the bubble, as shown in figure 1, from the axial direction that they had upstream, to being mostly in the theta direction. The total vorticity of the core is then changed from being in the axial direction, which creates strong rotation, to wrapping around azimuthally creating a negative axial velocity component. Further downstream, in the wake of the breakdown region, the centerline axial velocity recuperates to a positive value, but the flow maintains a wake-like profile with periodic oscillations as reported by Brucker and Althaus[5] and Leibovich[28]. The azimuthal velocity also partially recuperates its strength as shown in figure 6; and the vorticity core which goes back to being mostly in the axial direction is weaker than it was upstream of the breakdown, with a larger diameter. The diameter of the core increases by a factor of 1.4.

3.2.5 Dependence on the Circulation Number

Next, the dependence of the breakdown on the circulation number Ω is examined. The center of the bubble-like breakdown structure is characterized as the point with maximum negative axial velocity, and the location of the center is plotted versus time for different values of the circulation number. From figure 7, three distinct regimes of flow behavior are noticeable. For very low values of the circulation number, $\Omega < 3.2$, the flow behaves as shown in figure 8 for Ω=1.5. The point of minimum velocity that gets formed because of the initial axial vorticity gradient at the end of the filaments, continuously drifts downstream leaving the flow inside the domain breakdown free. There is an intermediate range of circulation numbers, $3.2 < \Omega < 3.5$, where the flow develops a stagnant recirculation bubble at the early stages of the simulation (Figure 9). The bubble then moves downstream in the flow until it washes out of the domain, and the steady flow becomes similar to the one observed for low Ω, with most of the vorticity in the axial direction. The third regime is identified when the circulation number is higher than a certain value, $\Omega >$ 3.5. In this case, the bubble that gets formed initially, drifts in the domain until it stabilizes in a certain equilibrium region and remains in it for the duration of the simulation. The steady location of the bubble in this regime agrees with Sarpkaya's[37] observations (Figure 8) that the location of the bubble moves upstream with increasing circulation number. For a very high circulation number, $\Omega = 4.27$ for example, the breakdown bubble drifts upstream until it stabilizes at the inlet of the domain as shown in figure 10. Its main internal characteristics remain similar to the ones described earlier for $\Omega = 3.52$.

The circulation number also has an effect on the mixing rate in the post-breakdown flow. This is a very important factor in the case of swirl combustors for example, where good mixing is required to ensure cleaner and more efficient burning. Since most of the mixing happens inside the breakdown bubble through the filling and emptying mechanisms described in section 3.2.2, it makes sense to use the size of the bubble as the parameter to characterize the mixing in the flow. To relate the mixing to the strength of the swirling flow or the circulation number in this case, the time averaged bubble diameter is plotted as a function of the circulation number. The bubble diameter is defined as the maximum diameter of the outer sleeve in the breakdown region; which is obtained from the maximum radial location of a filament, averaged over all the filaments that form the sleeve. This plot is shown in figure 11; it indicates an increase in the size of the bubble, and hence of mixing, with an increasing Ω.

3.2.6 Breakdown Fluctuations

In order to examine the structural fluctuations inside the breakdown region, the velocity field is computed and plotted on a two dimensional set of grid points distributed over a plane that cuts the bubble longitudinally in the middle in figure 12. The cycle shown in this figure is represented by a series of time steps at a stage were the flow has reached a stationary state. The bubble can be easily discerned; it has lost the symmetry it had during the startup phase (figure 3 t=15.0) and undergoes a cyclic behavior. If the three-dimensionality of the flow is neglected and the analysis is done from a two dimensional point of view, the following dynamics can be noticed. At t=110, a well defined eddy exists in the upper half of the bubble. This eddy starts to drift forward while losing strength between t=111 and t=112. This is simultaneously accompanied by the formation of another eddy in the lower half of the bubble. The new eddy starts out weak then strengthens while drifting to the center of the breakdown region. At t=113, the top eddy has become very weak, while the bottom eddy has clearly formed and located itself in the center of the lower half of the bubble. The breakdown region then undergoes similar dynamics to the ones previously described, to end up at the beginning of the cycle with a well defined top eddy while the bottom one is virtually non-existent. If these two dimensional dynamics are thought of from a three dimensional perspective by relating the motion of the eddies to the rotation of the breakdown structure, then the observations made support the observations of Sarpkaya [37] and Brucker and Althaus [5]. They concluded the presence of a tilted toroidal vortex ring, inside the breakdown structure, that gyrates about the axis of the bubble at a certain frequency. Even though the author does not agree with the ring terminology, because the discrete vorticity represented by the filaments does not close on itself (figure 1), the presence of a structure inside the breakdown region carrying azimuthal vorticity is evident from the velocity field of figure 3. The two dimensional flip-flopping of the eddies represents the gyration of the structure in a planar cut. The difference in strength of the top and bottom eddies however suggests that the tilted structure is not symmetric about its own axis. A complete understanding of the exact dynamics of the internal structure of the breakdown requires a three dimensional analysis of both velocity and vorticity fields. This will be done in the next section, but for now we will limit ourselves to looking at the frequency of these internal fluctuations and try to relate that to the circulation number which is the main governing parameter of the flow.

A time averaged plot of the velocity field on the longitudinal cut reveals a symmetric velocity distribution (figure 13). This means that the breakdown bubble is symmetric in a time averaged sense and that it undergoes a periodic fluctuation. The non-dimensional frequency of the fluctuation, or of the gyration of the structure as described by Sarpkaya, is visually estimated to be about 0.16. This frequency is also equivalent to the frequency of the periodic oscillation of the flow in the wake of the breakdown region (figure 14), which was estimated using the peak to peak distance between two waves and the average axial velocity at that location. For a more accurate calculation of the dominant frequency in the bubble, the fluctuating axial and azimuthal velocity components are computed at two fixed locations inside the bubble, downstream of the front stagnation point at x=11.5. The front stagnation point being at x=10.5. The two fixed probing points are located off the centerline, at a radius r=0.1 and r=0.25. The axial and azimuthal velocity fluctuations are shown in figure 10. The graphs show a periodic fluctuation of both components of velocity. Power spectra plots of these fluctuations are presented in figure 16 and indicate that the dominant frequency is equal to 0.163 and is the same for both the axial and the azimuthal components of velocity at the two radial locations. This frequency is also equivalent to the one visually approximated from the two-dimensional fluctuations in figure 12 and the oscillation in the wake of the breakdown in figure 14.

Power spectral plots of the azimuthal velocity at the center of the bubble were also done for three flow cases of circulation numbers $\Omega=3.26$, $\Omega=3.7$ and $\Omega=4.27$. The plots are shown in figure 17 and again indicate that in each case there is one dominant frequency of fluctuation in the breakdown region. The dominant frequencies for the three simulations are St=0.154, St=0.175, and St=0.193 respectively. Figure 18 is a plot of the Strouhal number versus the circulation number, which yields a linear relationship between the two. This indicates that the frequency of fluctuation of the internal structure of the breakdown bubble and the shedding frequency in the wake region, are only affected by the rotation rate at the inlet of the domain, which is characterized by the non-dimensional circulation number Ω. These results are also compared with experimental data obtained from Garg and Leibovich[19] and Faler and Leibovich[17], who performed spectral analysis on the axial and azimuthal velocity fluctuations in the breakdown region. Note however that there are some differences between the experimental and the numerical flow conditions, such as the axial inlet flow profile, the experimental set-up of confined flow, and the circulation number which Faler and Leibovich base on the diameter of the test section rather than on the diameter of the vorticity core, as defined in chapter 2. We were able to compare with two runs in which a bubble breakdown occurred and in which the spectral analysis was done for the velocity fluctuations inside the bubble. With the appropriate transformations of the circulation number, for Ω equal to 3.6 and 4.4, the non-dimensional experimental dominant frequencies inside the breakdown bubble were 0.125 and 0.204 respectively. Considering the differences between the experimental and the numerical flow fields, and the errors associated with the transformation of the data for comparison, the results obtained numerically using the VEM compare well with the experiments as shown in the following table:

Ω_n (numerical)	Ω_{GL} (G F L)	St_n	St_{GFL}	Ω_{GFL}/Ω_n	St_{GFL}/St_n
4.27	4.4	0.19	0.204	1.03	1.05
3.77	3.6	0.175	0.125	0.95	0.72

3.3 Internal Structure of the Breakdown Bubble

3.3.1 Vorticity Field

A study of the internal structure of the breakdown bubble is necessary in order to reach a solid explanation regarding its formation and stability. The vorticity field is computed on a 36x17x17 computational grid by taking the curl of the corresponding velocity field which is obtained from a direct computation onto the grid points using the Biot-Savart representation. Figures 19 and 20 show a time sequence of the three-dimensional tangential and axial vorticity maps of the breakdown region. This sequence corresponds to the cycle shown in figure 12 for a circulation number of 3.52. The three-dimensional map is constituted of six transverse slices of the flow, ranging from the axial location 8.5 to 13.5 by steps of 1.0, the front stagnation point being at 10.5.

Upstream of the bubble (slice 1), the approach flow is symmetric and carries vorticity purely in the axial direction. The vorticity core is clearly defined in the first slice of the axial vorticity plot, while the azimuthal vorticity contour plot is uniform with values of vorticity near zero. As the nose of the bubble is approached (slices 2 and 3), one can clearly see the axisymmetric change of the vorticity distribution, and its transformation from axial vorticity into azimuthal vorticity. A symmetric structure carrying azimuthal vorticity starts appearing inside the bubble, while the axial vorticity is still decaying. Further downstream (slice 4) is a slice through the structure that shows a higher azimuthal vorticity. It also clearly shows a concentration of high azimuthal vorticity at a certain location on the structure. Figure 19 is not enough to guarantee the asymmetry; the same observations would also be valid if the structure was tilted and axisymmetric about its own axis rather than about the flow axis. However, this possibility is not valid if one looks at the velocity field plot of the midplane, shown in figure 12. The asymmetry of the two-dimensional eddy-like structures in that figure indicates that the vortical structure observed in figure 19 is not symmetric about any axis, but rather has a region of concentrated azimuthal vorticity at a certain azimuthal location. The time sequence shows that the region of high vorticity rotates around the azimuth of the bubble at the same frequency shown in figure 16 for the velocity fluctuations inside the bubble. Towards the tail of the bubble (slices 5 and 6), the magnitude of the azimuthal vorticity is reduced while the axial vorticity re-intensifies. The flow at this stage has clearly become asymmetric. The axial vorticity core is formed again, downstream of the breakdown region, but with less strength than it had before the breakdown.

It is important to note that the velocity fluctuations inside the bubble, the two-dimensional flip-flopping of the eddy-like structures in figure 12, and the fluctuations in the wake of the breakdown are all related to the asymmetric concentration of tangential vorticity observed in figure 19 and its rotation around the axis of the bubble. The next section examines the origin of the described asymmetry.

3.3.2 Asymmetry of the Breakdown Bubble

To analyze the non-axisymmetric features observed near the tail of the bubble in the vorticity plots of figures 19 and 20, we need to examine the behavior of the discrete vorticity field in the flow, represented by the vorticity filaments. Figure 22 is a three-dimensional view of the vorticity lines pertaining to the outer layer. They appear to have a symmetric azimuthal distribution in the breakdown region and can therefore be neglected in the analysis of the asymmetry. Figure 23 shows the time evolution of the vorticity lines pertaining to the inner layer, the time steps shown correspond to the series of figure 19. In the breakdown region, the filaments are cork-screw shaped with an opposite winding to the rotation of the flow. The combination of these helical filaments in the front section of the breakdown is a globally symmetric structure, which corresponds to slices 2 and 3 of the azimuthal vorticity contour plot, where a symmetric vorticity structure starts to appear. As the tail of the bubble is approached, the symmetry is lost and part of the filaments drift close to each other to form a pack. A comparison between figures 19 and 23 shows the correspondence between the location of the azimuthal vorticity concentration inside the breakdown region and the location of the concentrated pack of filaments around the azimuth. It is clear therefore that the asymmetry observed in figure 19 is a perturbation picked up by the flow, that results in an uneven distribution of the filaments around the azimuth.

In order to get a clearer understanding of the asymmetry, all seven filaments forming the inner layer are plotted individually in figure 24. If this figure is looked at in conjunction with figure 25 which shows the time evolution of one of the filaments, one can notice that each filament undergoes a cyclic evolution near the breakdown region, and that at any time step all the filaments are at different stages of this evolution. As shown in figure 25, an individual vorticity filaments undergoes the following dynamics. At t=110, the filament wraps in a helical fashion in the breakdown region then extends axially in the flow. The hairpin-like structure can be considered as inexistant as far as its effects on the dynamics of the flow since the total vorticity carried by both arms cancels out. As the flow develops further, the filament starts winding more and more near the tail of the breakdown. The filament which had a large winding diameter at the nose of the bubble because of the expansion of the core, decreases in winding diameter until it reaches a point where it gets ingulfed in the negative axial flow. Tracking the tip of a helical wave shows that this point travels downstream while wrapping on a helix with an increasing radius until t=112, then a decreasing radius until t=115. At that stage, the radius of the helical path has decreased enough for the filament to reach a region of negative axial flow near the centerline axis. The point in question stagnates in the flow while the rest of the helical wave continues to travel downstream. This causes the filament to stretch and both arms of the wave to collapse into a hairpin (t=123) with minimal vortical effect on the rest of the flow. The described dynamics show the process by which the azimuthal vorticity that was created at the nose of the bubble and that is responsible for the recirculating flow inside the breakdown zone, is eliminated near the tail of the breakdown resulting in a post-breakdown flow carrying vorticity mostly in the axial direction. The frequency for a complete cycle is about 0.9. Note that between t=113 and t=114, part of the filament is removed from the flow. This is due to the implementation of the mechanism described in section 2.7.2; it has already been shown in figures 2.7 and 2.8 that the implementation of this mechanism has a minimal effect on the flow since most of the double hairpin structure is downstream of the breakdown region and the vorticity that it carries is cancels itself out.

3.4 On the Formation and Stability of a Vortex Breakdown

This section is a recapitulation on the results obtained and presented in this chapter in order to provide a solid explanation for the vortex breakdown phenomenon. There are two major parts involved in such an explanation: (1) the study of the mechanisms leading to the formation of the breakdown in an initially axial vorticity core, and (2) the study of the mechanisms by which this phenomenon sustains itself in the stationary state regime. The focus of this work has been mainly on the sustainability and internal dynamics of the breakdown, which will be discussed in the next section. This study has nevertheless shed some light, in conjunction with previous experimental and theoretical works, on the origin of the breakdown, and this will be discussed in a separate section at the end of this chapter.

3.4.1 Dynamics and Sustainability of Vortex Breakdown

The three-dimensional plots of the vorticity contours and the vorticity filaments in figures 19, 20, 23, 24, and 25 provide a clear view of the dynamics of the flow. The presence of a breakdown is attributed to a negative gradient in axial vorticity in the flow field, which can be related to the negative gradient in axial velocity and to the consequent bulging of the filaments near the breakdown region. The resulting axial difference in rotational speed causes the incoming axially aligned vorticity filaments to tilt in the direction opposite the direction of rotation, which in turn contributes to maintaining the negative axial velocity gradient, and feeds back into the cycle. Moreover, the tilting of all the filaments around the periphery creates the azimuthal vorticity structure identified in figure 19. The mechanism by which the breakdown bubble sustains itself is therefore a self-feeding mechanism fundamentally governed by inviscid dynamics, which agrees with Brown and Lopez[4] and Althaus' [19] conclusions. Brown reports self-feeding inviscid vorticity dynamics similar to the ones observed from this model, while Althaus takes it further and develops a Feedback Model for the breakdown. The formed breakdown structure does not stagnate unless its azimuthal vorticity is enough to counteract the positive axial velocity of the potential flow. This requires the circulation of the filaments, and subsequently the circulation number characterizing the flow (figure 7), to be higher than a certain threshold value. Globally, the formation of the breakdown is axisymmetric while the discrete field is composed of cork-screw filaments wrapping helically in the region of the breakdown. On the other hand, the tail of the breakdown region is clearly asymmetric. Its dynamics follow the individual dynamics of the filaments described in the previous section. These dynamics are responsible for the elimination of the azimuthal vorticity from the tail of the bubble by means of capturing the helical filament as its radius decreases near the wake, and stretching it to form a hairpin structure with minimal vortical effect. This process is cyclic, but the filaments are always at different stages of it, which creates the asymmetry.

The analyzed dynamics of the flow indicate that the formation of the breakdown from an initially axial voritcity core in the pre-breakdown region is axisymmetric, while the return of the flow, near the tail of the breakdown, to a weaker and oscillating axial vorticity core is asymmetric. It is interesting to note though, that the asymmetry near the tail and in the wake of the breakdown does not have an effect on the incoming globally axisymmetric flow which remains axisymmetric as the breakdown region is formed.

3.4.2 Theories on the Onset of Vortex Breakdown

During the past forty years, several theories have been proposed to explain the occurrence of vortex breakdown. In this section, some of the most notable of these theories are discussed in light of the results obtained in the chapter. The theories can be classified under three major categories: the instability theory, the conjugate-state theory, and the wave theory.

Despite the fact that an axisymmetric theory cannot fully account for both the bubble and the spiral forms of vortex breakdown, most investigators have focused their efforts on finding a theoretical explanation based on axisymmetric dynamics, assuming that asymmetric features are secondary to the fundamentals of the phenomenon. Among those who have contributed to the study of breakdown stability are Howard and Gupta[22] and Garg and Leibovich[18] who have worked on finding criteria for the stability of vortex flows to axisymmetric disturbances. Even though the results obtained from our model and discussed in this chapter present no evidence that opposes the theory of attributing a breakdown to instabilities created by axisymmetric disturbances in the flow field, there is no evidence of the slow continuous growth which is a characteristic feature of hydrodynamic instabilities (Figure 25). Ludwieg[31], on the other hand, has gone to the opposite extreme. He has given all the emphasis to asymmetric features by attributing the breakdown to non-axisymmetric disturbances. His model predicts instability for approach flows. This is not valid in light of our results, figure 1, in which the transition from an axial vorticity core in the approach flow to a bubble carrying mainly azimuthal vorticity appears to be globally axisymmetric. Asymmetric features are only apparent near the tail and in the wake of the breakdown. It is important to note, however, that subsequent work has clearly shown that vortex flows are less stable to spiral disturbances than to axisymmetric ones (Escudier [15]).

The conjugate-states theory was first advanced by Benjamin[3] in 1962. In an analogy to the hydraulic jump in open channel flows, Benjamin attributes vortex breakdown to a transition between two conjugate swirling flow states; the one upstream of the breakdown being supercritical, while the one downstream of it is subcritical. Swirling flows can be classified as "supercritical" if the phase speed is in the downstream direction, and "subcitical" if the phase speed is in the upstream direction. The critical point separating this transition allows the presence of standing waves of extreme length. Benjamin concludes that the momentum flux is larger in the subcritical region, and since there are no forces applied on the flow, in the inviscid case, he attributes the difference in momentum flux to the presence, on the subcritical flow, of weak standing waves, which are replaced by turbulence in the case of strong transitions (Escudier [15]). As noted by Escudier and supported by our results, the transition shown in figures 22 and 23 by the divergence and tilting of the vorticity lines, which correspond to material lines in inviscid flows, are smooth and do not support the proposed sudden turbulent transition.

The wave theories are based on Squire's [41] theory of wave propagation. Squire's model also involves a transition between two conjugate states. He attributes the breakdown to the propagation, in the upstream direction, of waves created by a downstream disturbance in the subcritical regime. The travelling waves cannot pass the critical point into the supercritical region; instead they create an accumulation of disturbances that results in the observed breakdown. This idea was however refuted by

Benjamin[62] who showed that even though the phase velocity of these waves is upstream, their group velocity is positive and thus the energy cannot be convected upstream in the flow.

Other wave theories followed Squire's work such as Randall and Leibovich[35], but they will remain beyond the scope of our work because of their dependance on adverse pressure gradients created by slowly diverging confinements, while our model is an unconfined flow model.

This section is in no way meant to provide a complete and comprehensive analysis of all the theories behind vortex breakdown. The aim is to gain a clearer view of where the results obtained in this work stand with respect to some of the available theories and what features our model still lacks, for a more complete evaluation of these theories . In the future, a more comprehensive model, that includes expanding geometries and variable inlet velocity profiles and vorticity distributions, needs to be achieved in order to reach a final conclusion regarding the origin of all axisymmetric and non-axisymmetric aspects of vortex breakdown.

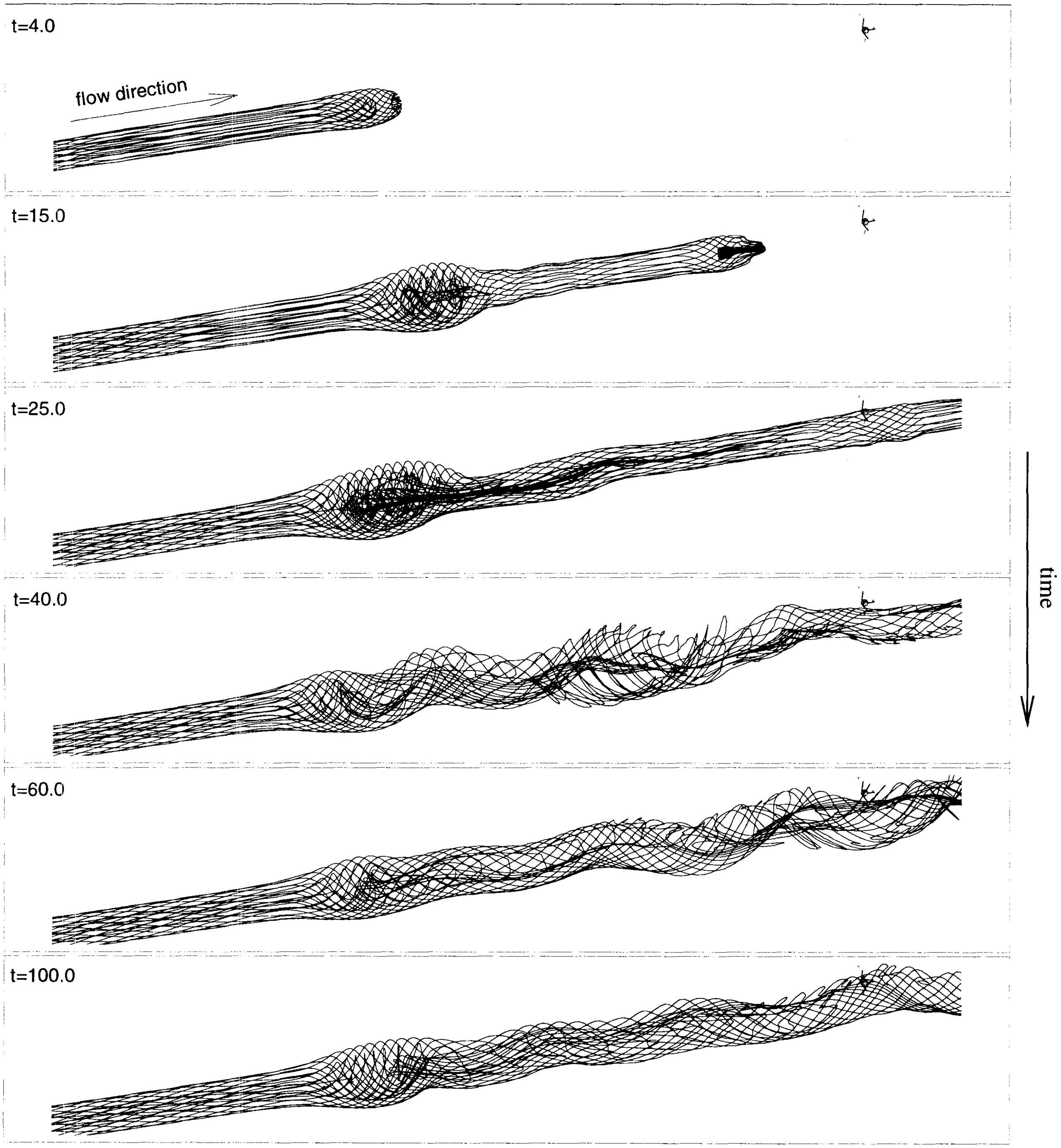

Figure 3.1: Three dimensional visualization of the vorticity filaments. (circulation number = 3.52) Flow direction is in the positive x direction, and flow rotation is counter-clockwise.

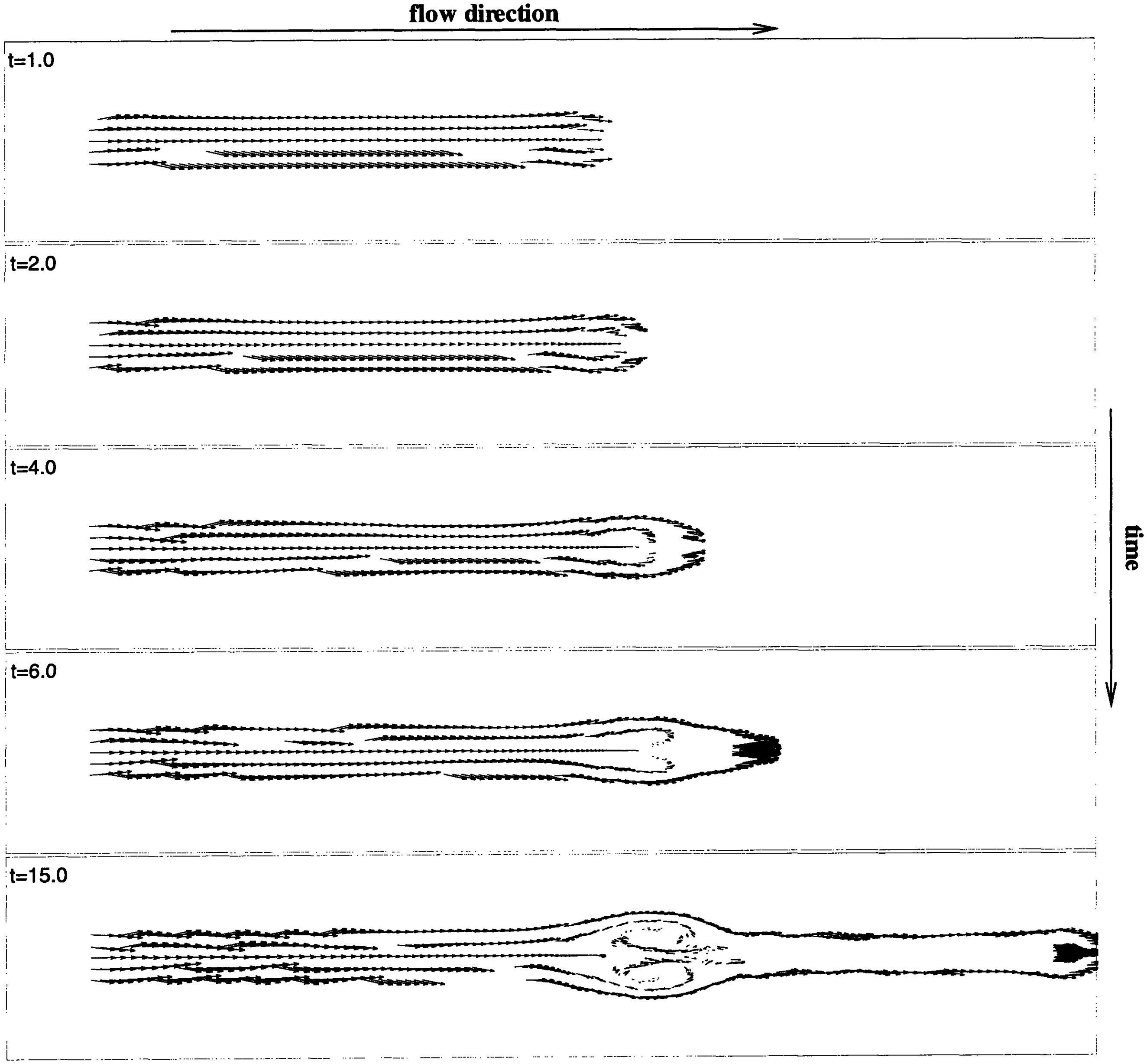

Figure 3.2: The location and velocity of the elements in a longitudinal cut of the flow, of thickness 0.2. (circulation number = 3.52)

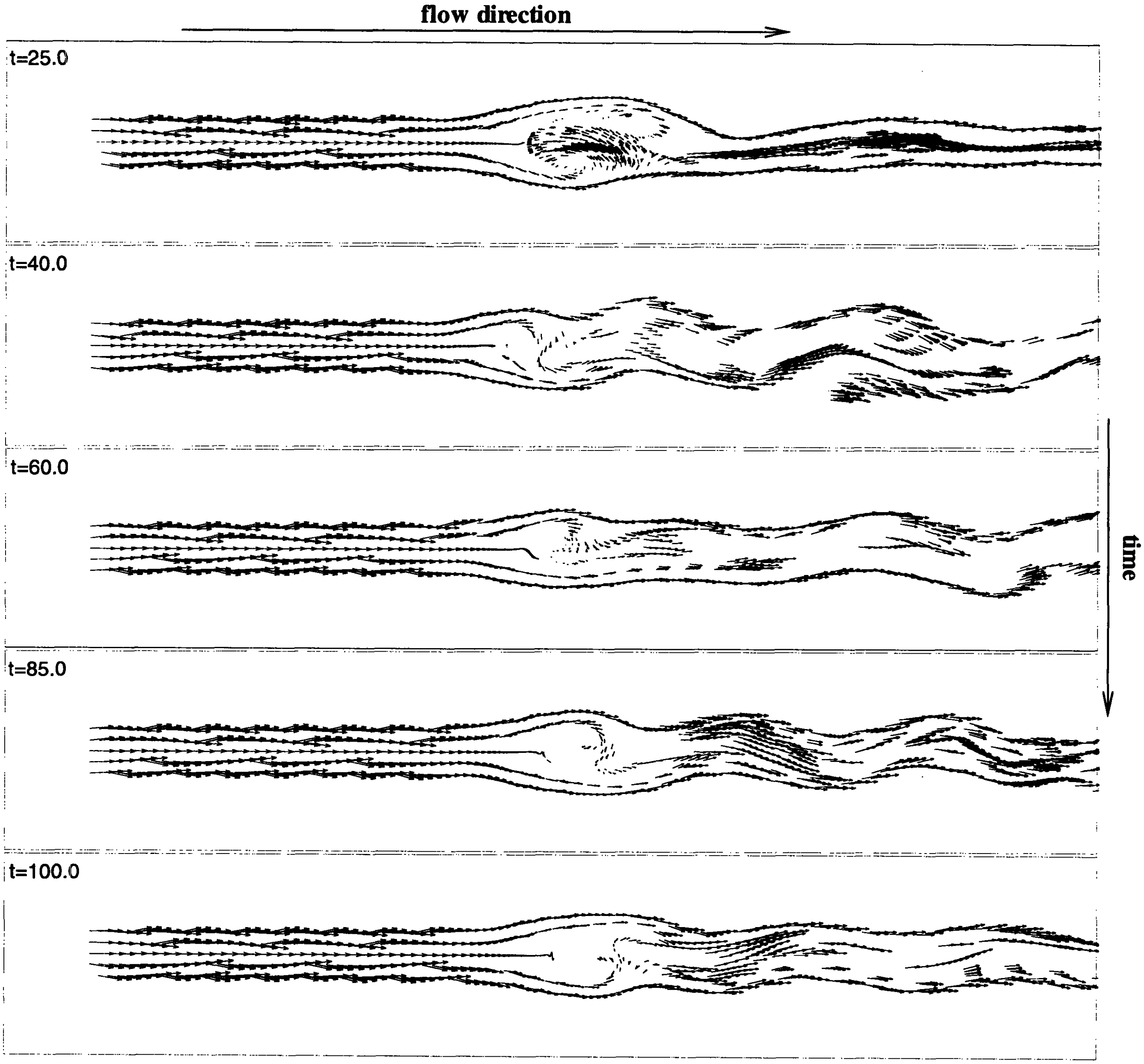

Figure 3.2: continued

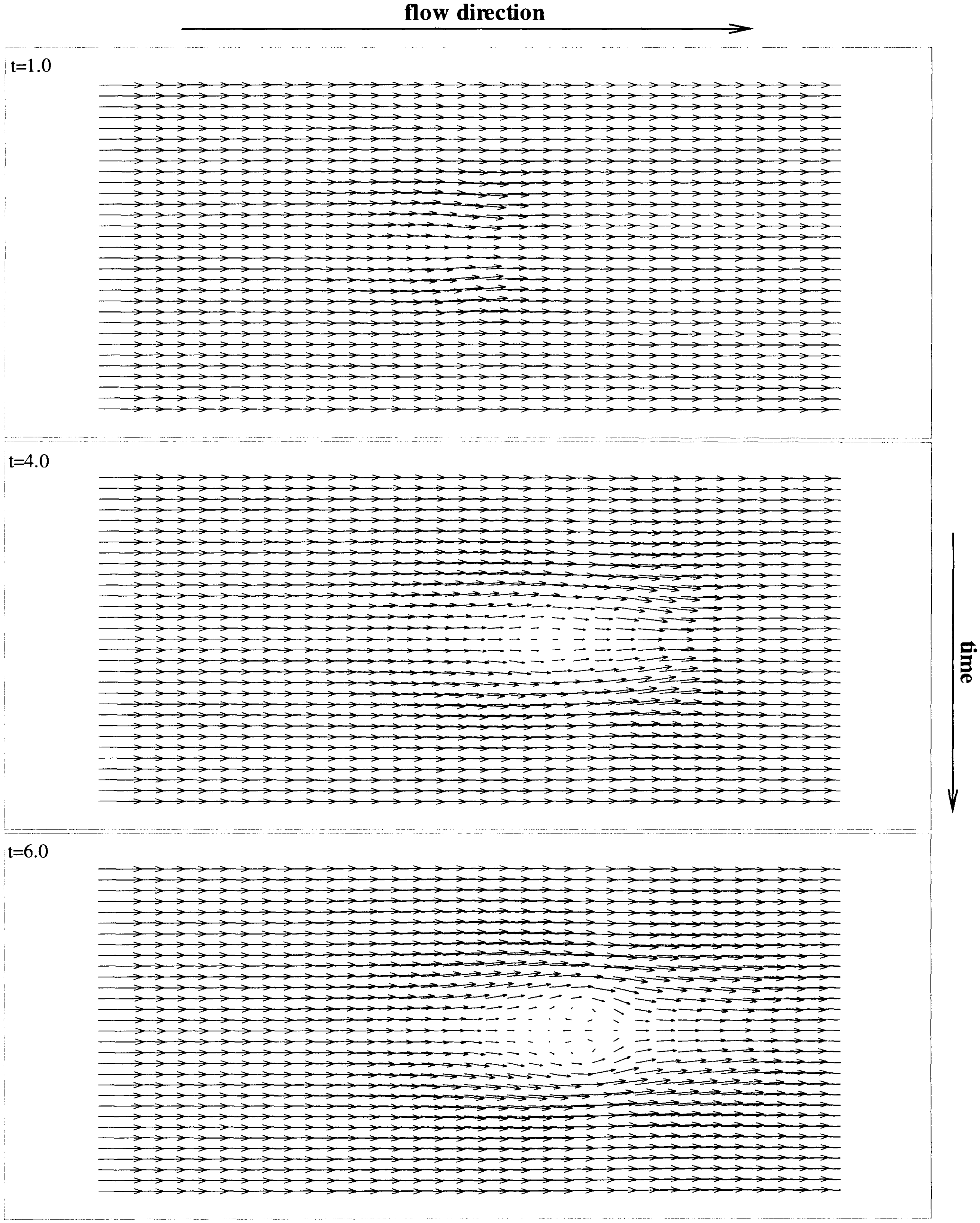

Figure 3.3: Two dimensional velocity plot on a grid longitudinally cutting the flow in the middle. (circulation number = 3.52)

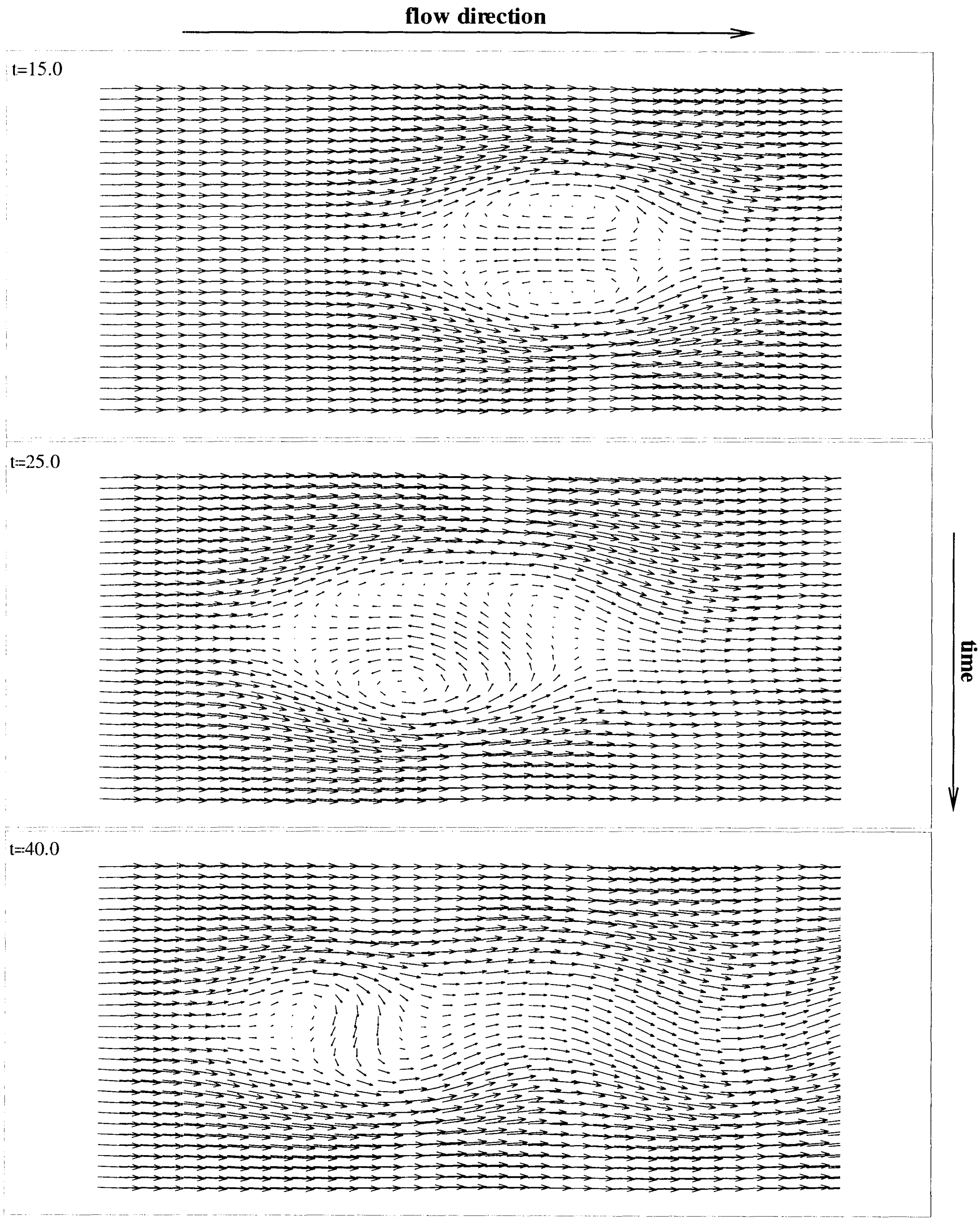

Figure 3.3: continued

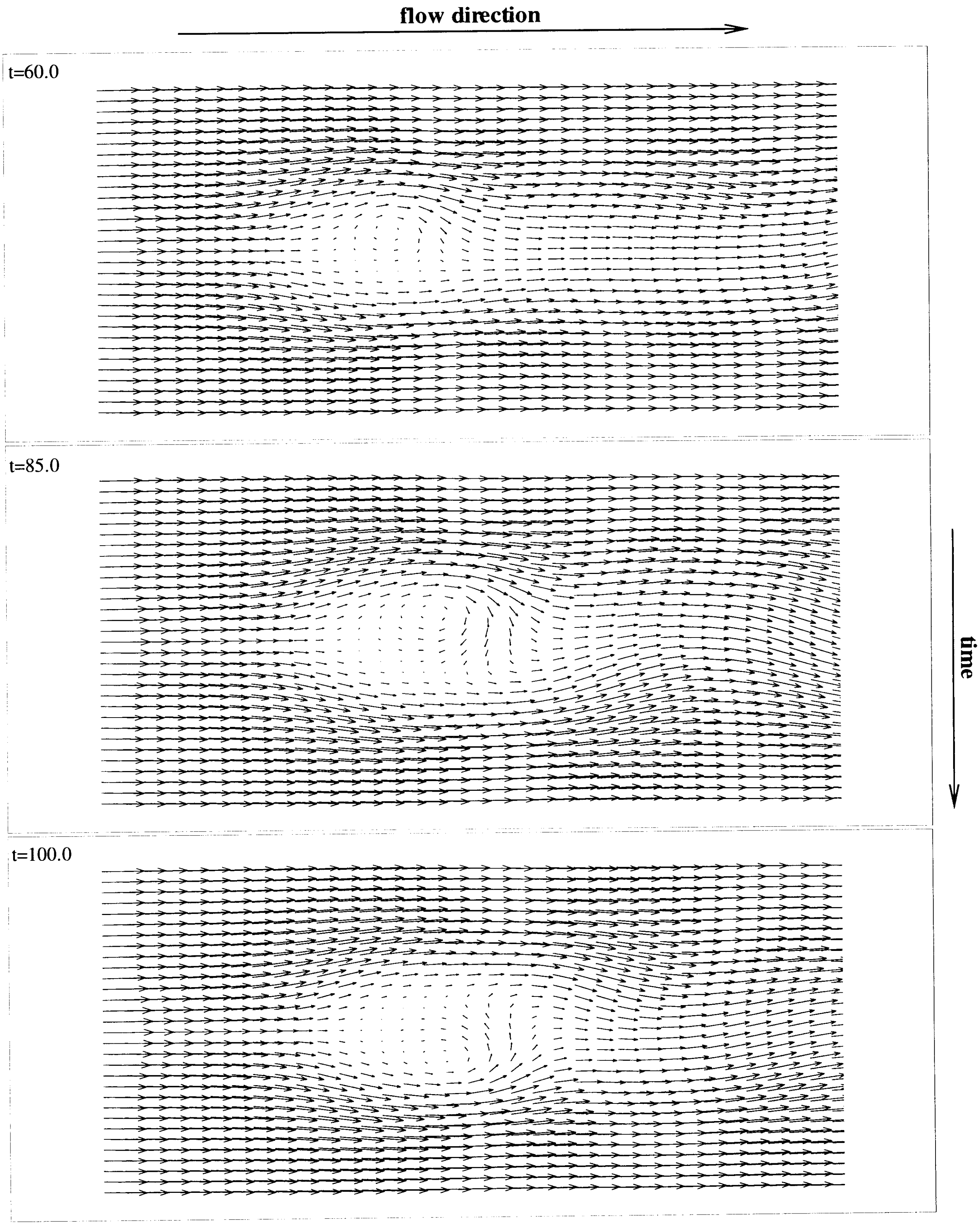

Figure 3.3: continued

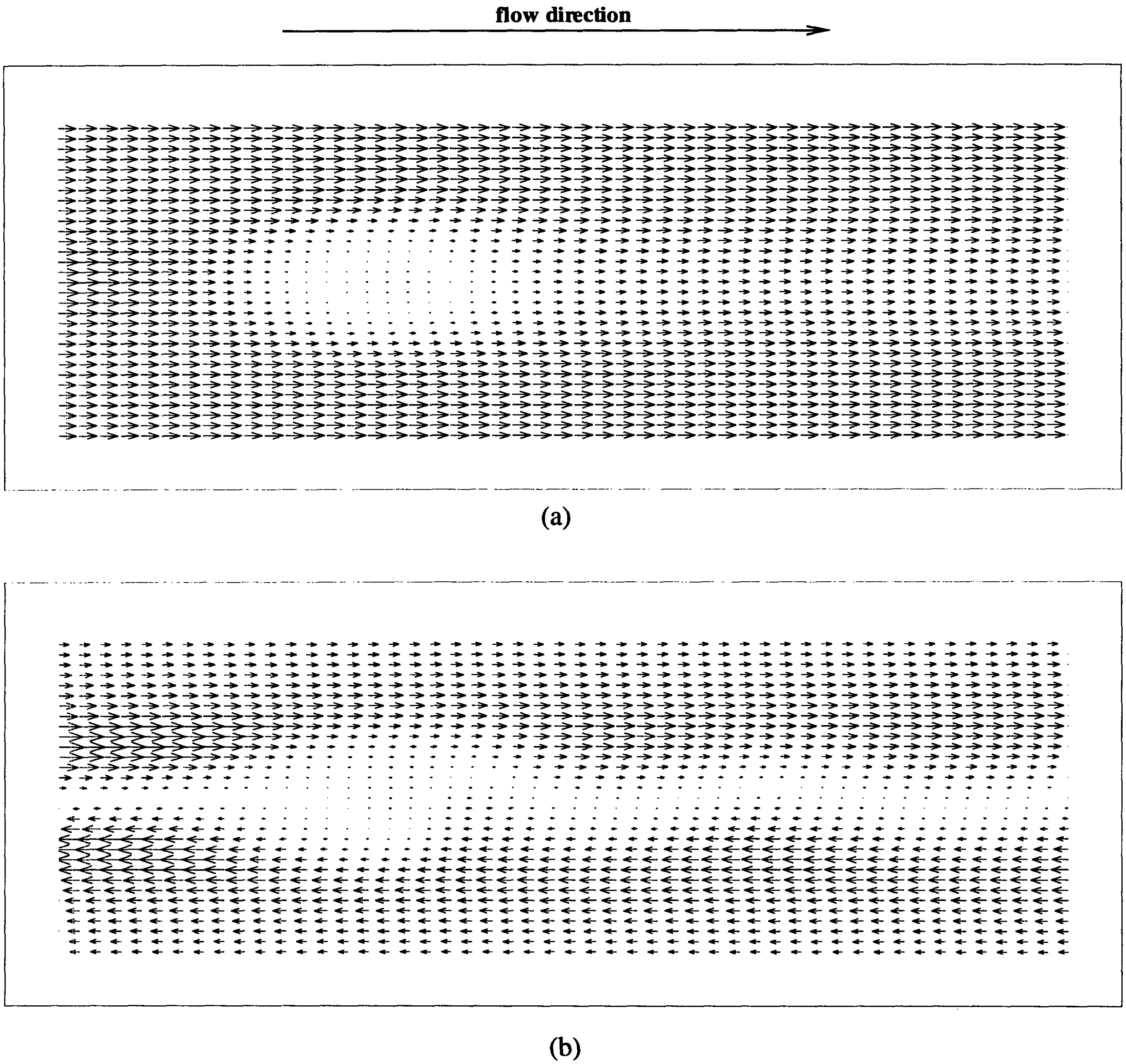

Figure 3.4: (a) axial and (b) azimuthal velocity profiles on a two dimensional grid longitudinally cutting the flow in the middle. (circulation number = 3.52) (t=100.0)

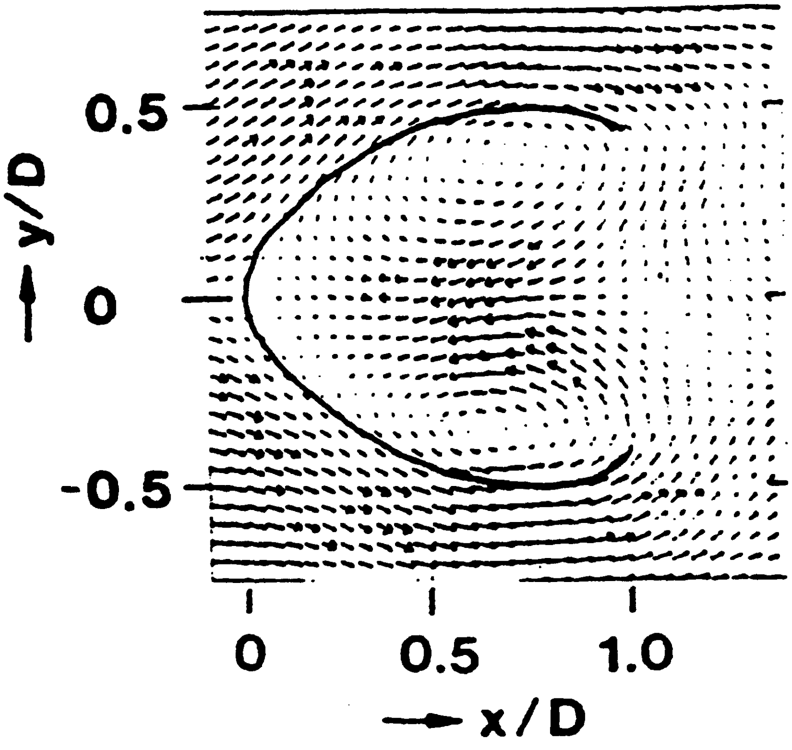

Figure 3.5: Instantaneous velocity field in the midplane of the bubble (Brucker and Althaus, 1992).

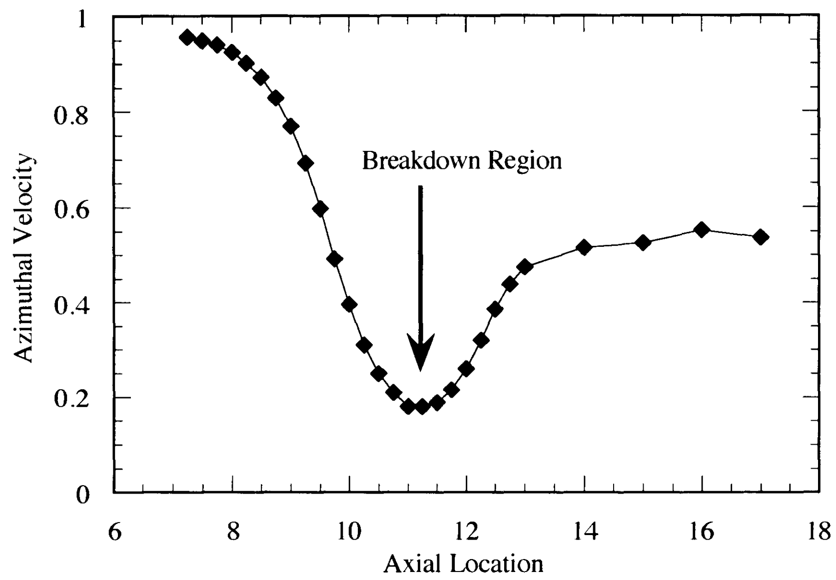

Figure 3.6: Change of azimuthal velocity with axial location, at a radial location where the inlet azimuthal velocity is maximum, r=0.625. (time averaged)

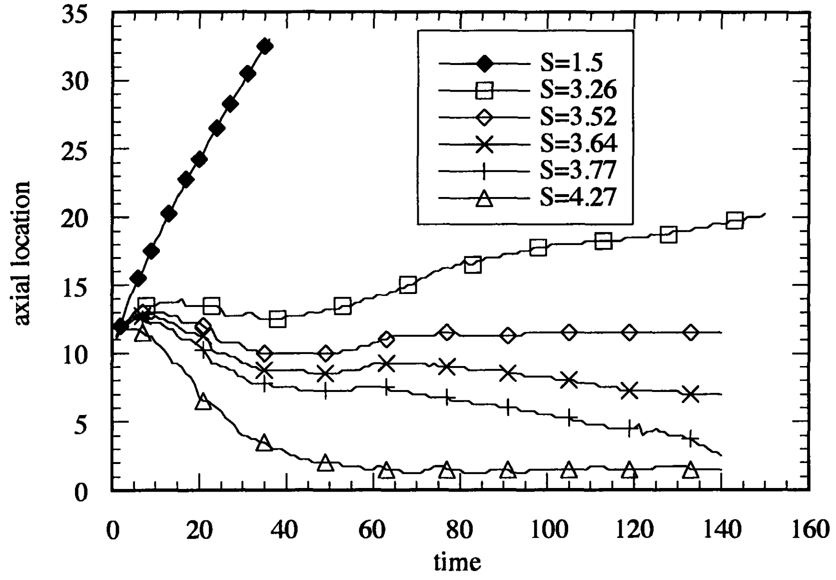

Figure 3.7: Axial location of the point of minimum axial velocity for different values of the circulation number Ω (S).

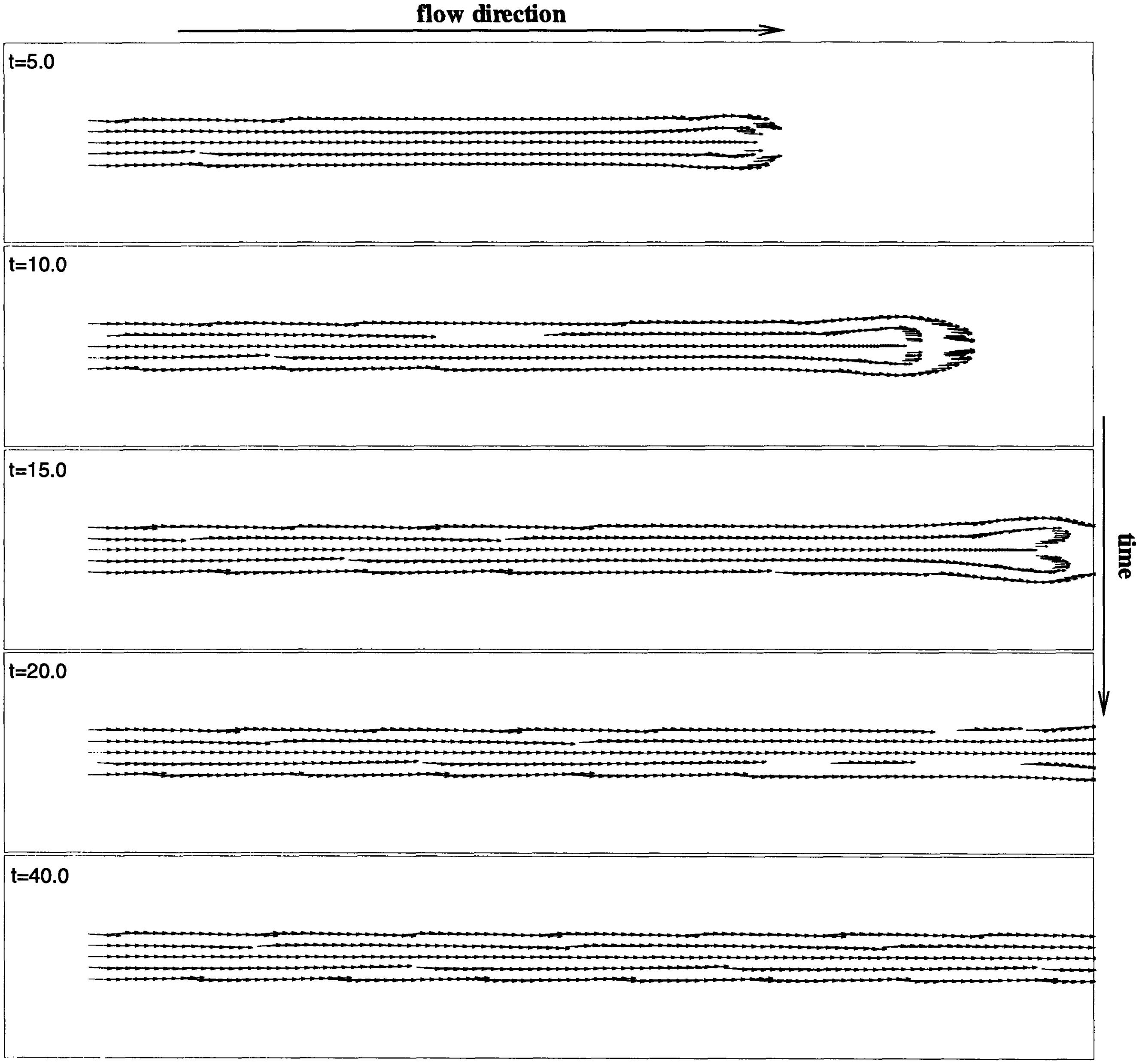

Figure 3.8: The location and velocity of the elements in a longitudinal cut of the flow, of thickness 0.2. (circulation number=1.5)

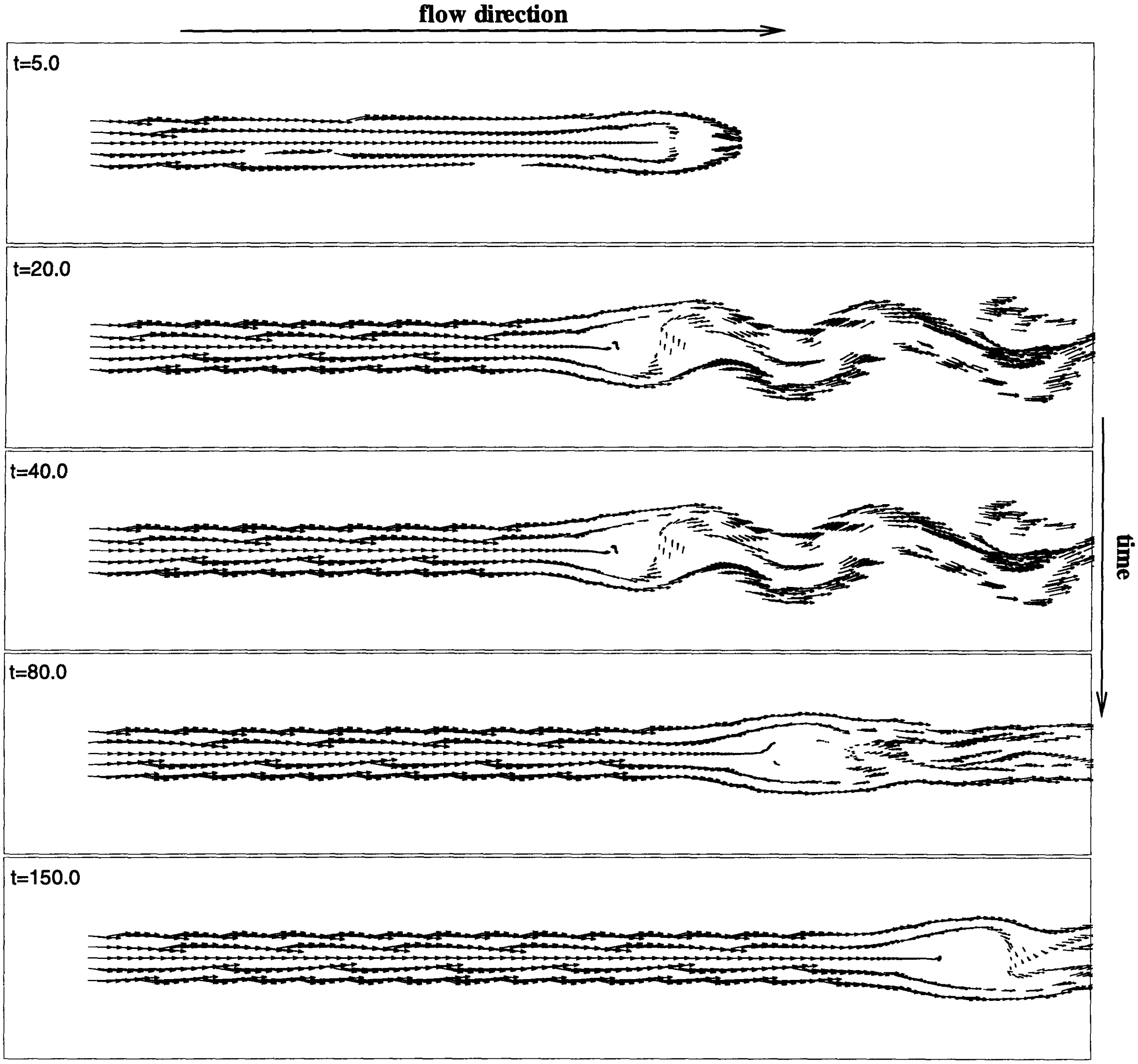

Figure 3.9: The location and velocity of the elements in a longitudinal cut of the flow, of thickness 0.2. (circulation number=3.26)

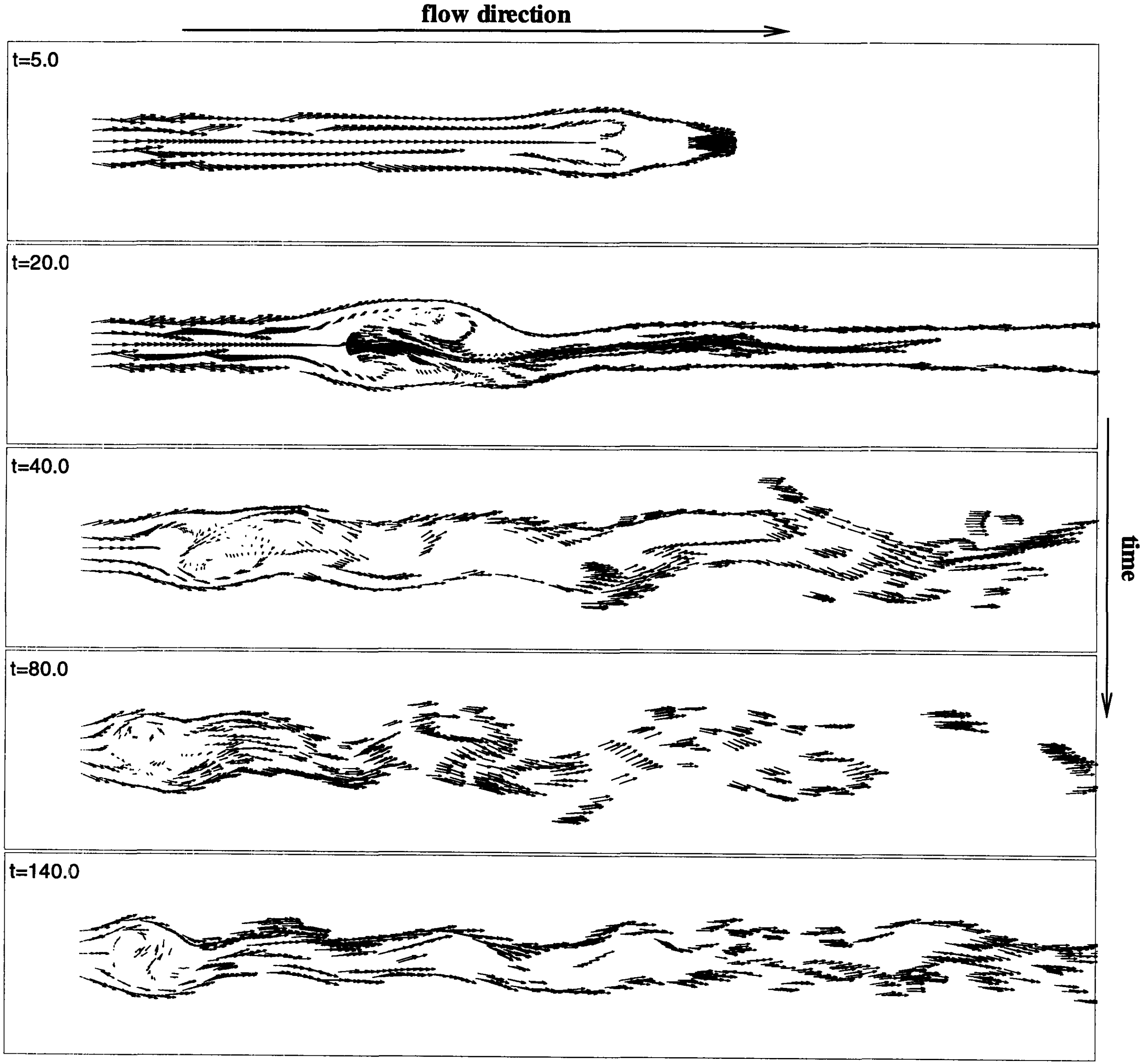

Figure 3.10: The location and velocity of the elements in a longitudinal cut of the flow, of thickness 0.2. (circulation number=4.27)

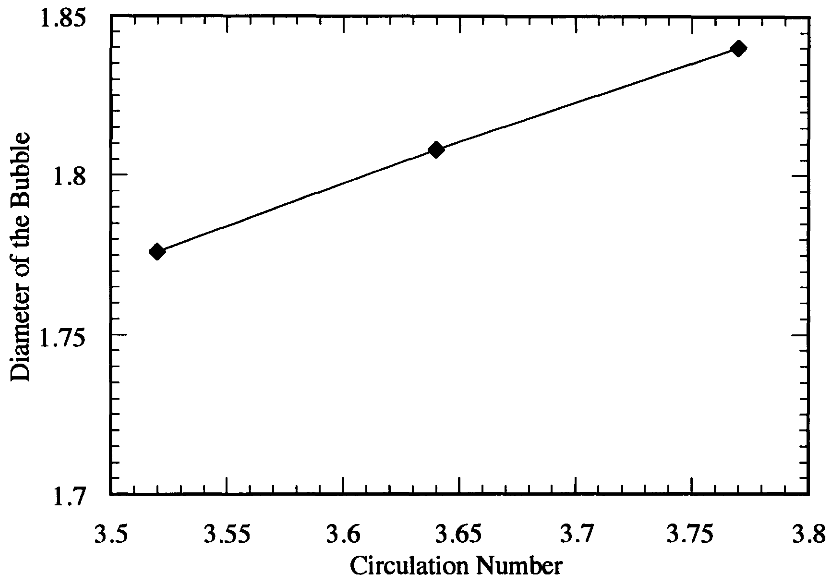

Figure 3.11: Time averaged diameter of the breakdown bubble as a function of the circulation number.

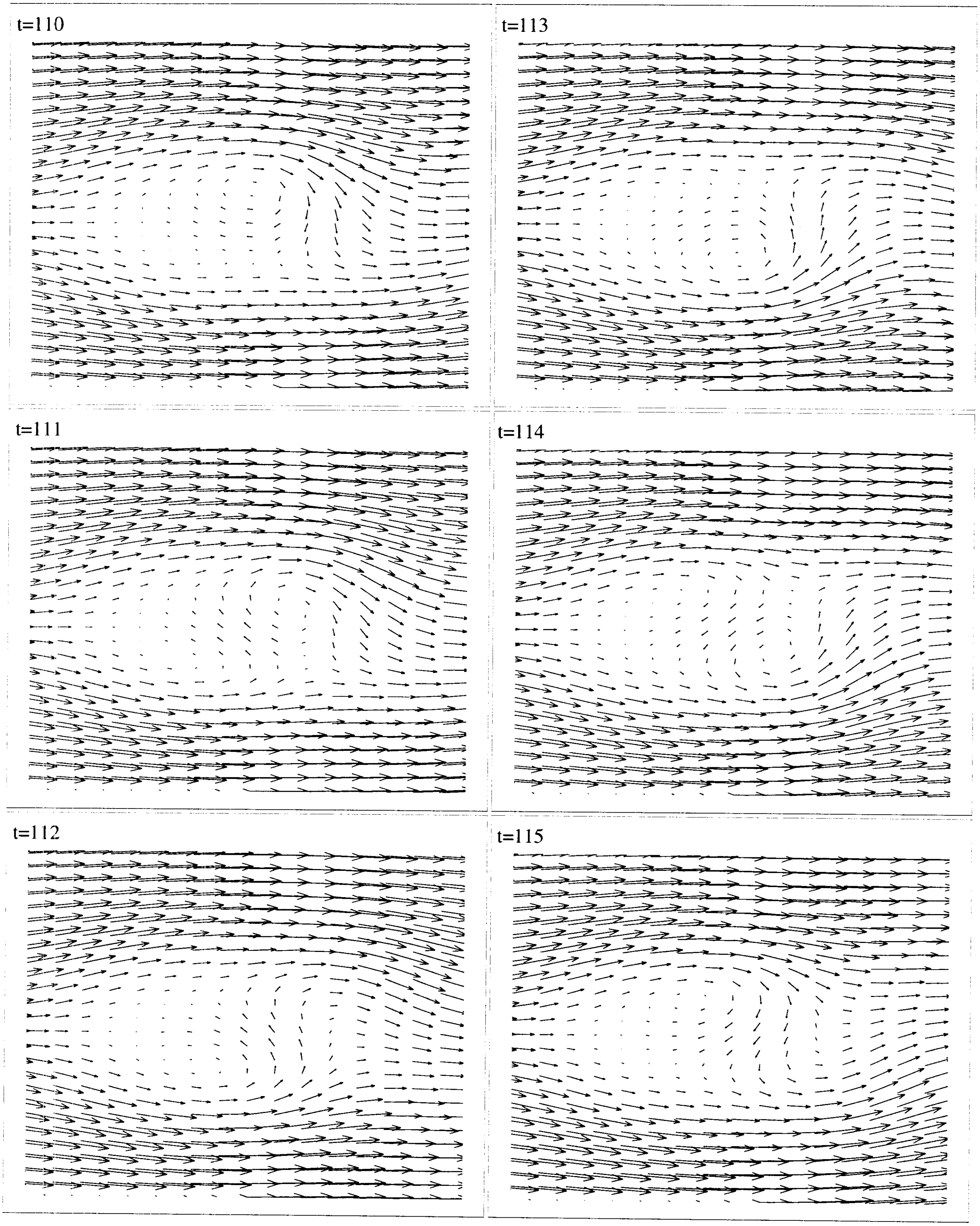

Figure 3.12: A fluctuation cycle shown by the velocity field on a grid cutting the flow longitudinally in the middle.

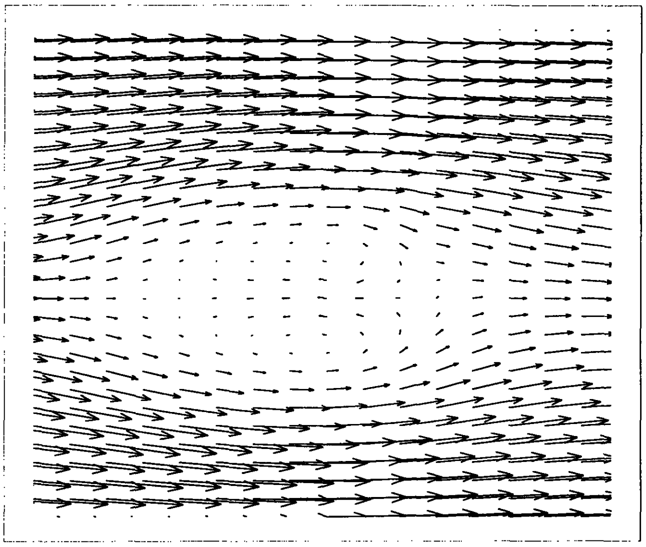

Figure 3.13: Time averaged velocity field on a grid cutting the flow longitudinally in the middle.

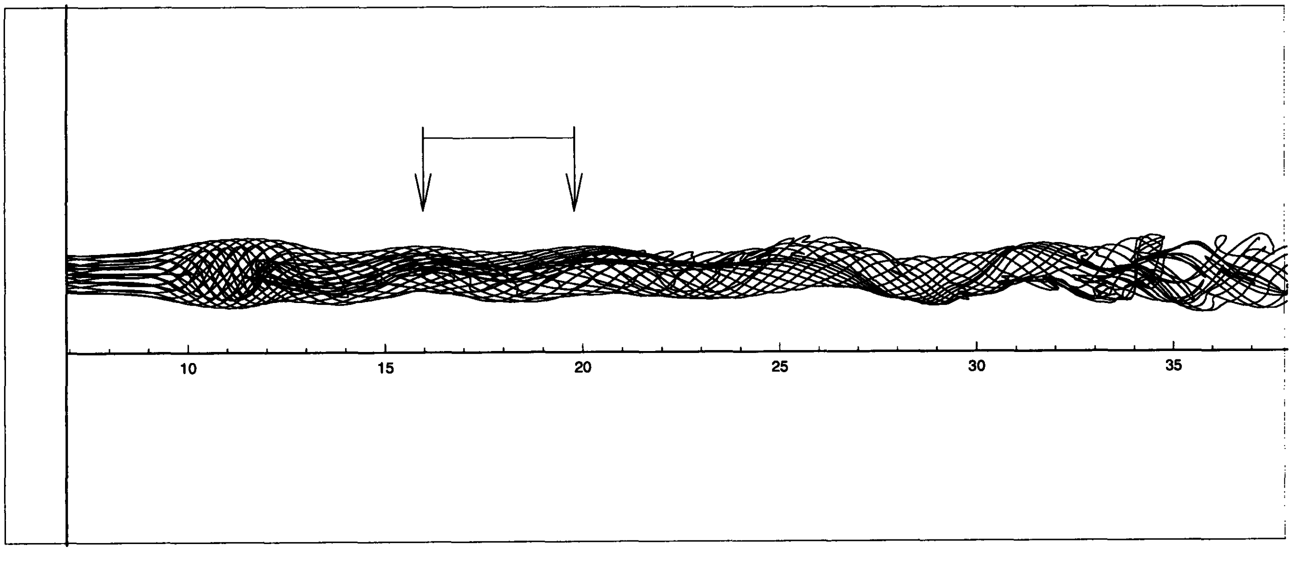

Figure 3.14: Periodic oscillations in the wake of the breakdown bubble.

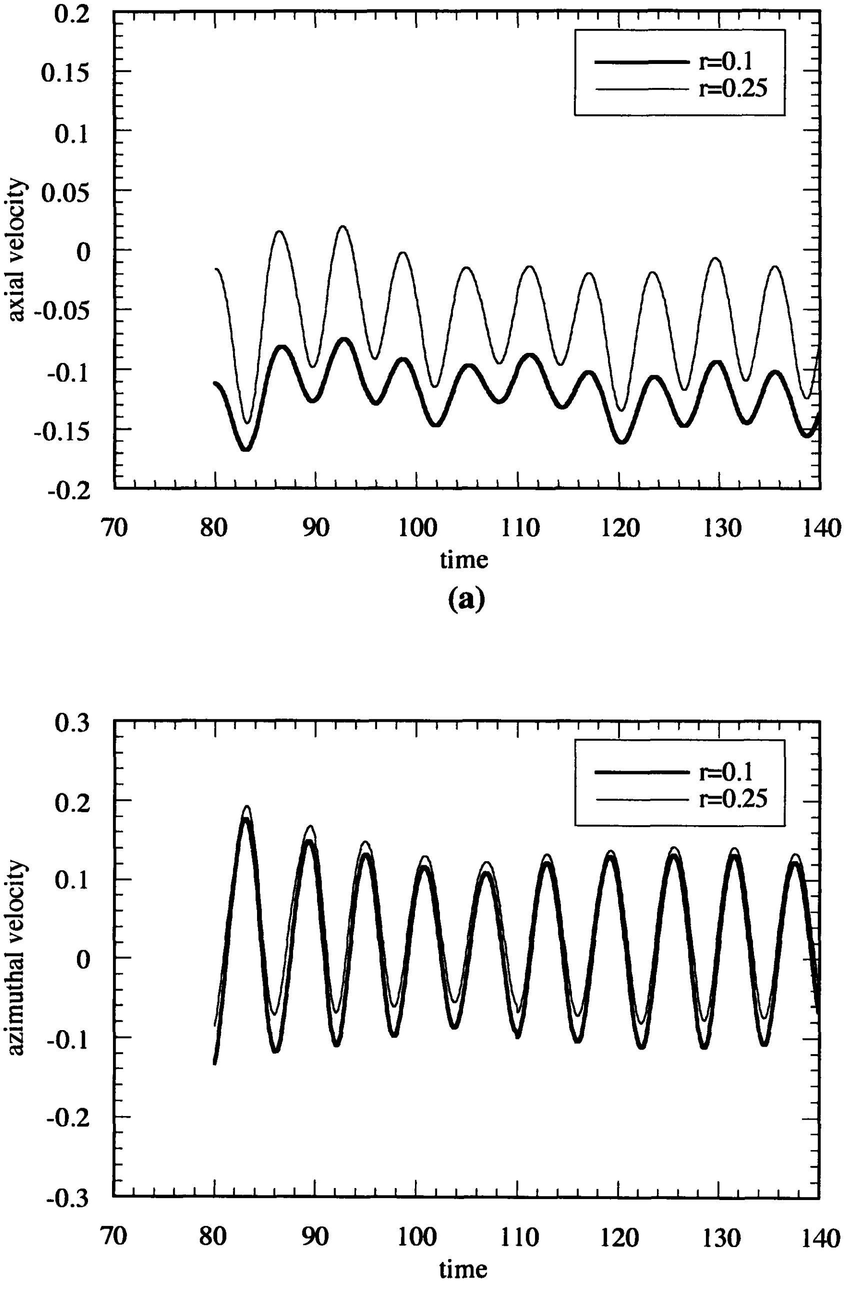

Figure 3.15: Velocity fluctuations inside the bubble downstream from the front stagnation point at an axial location x=11.5 and radial locations r=0.1 and r=0.25. Front stagnation point is at x=10.5. (circulation number Ω=3.52)
(a) axial velocity fluctuations.
(b) azimuthal velocity fluctuations.

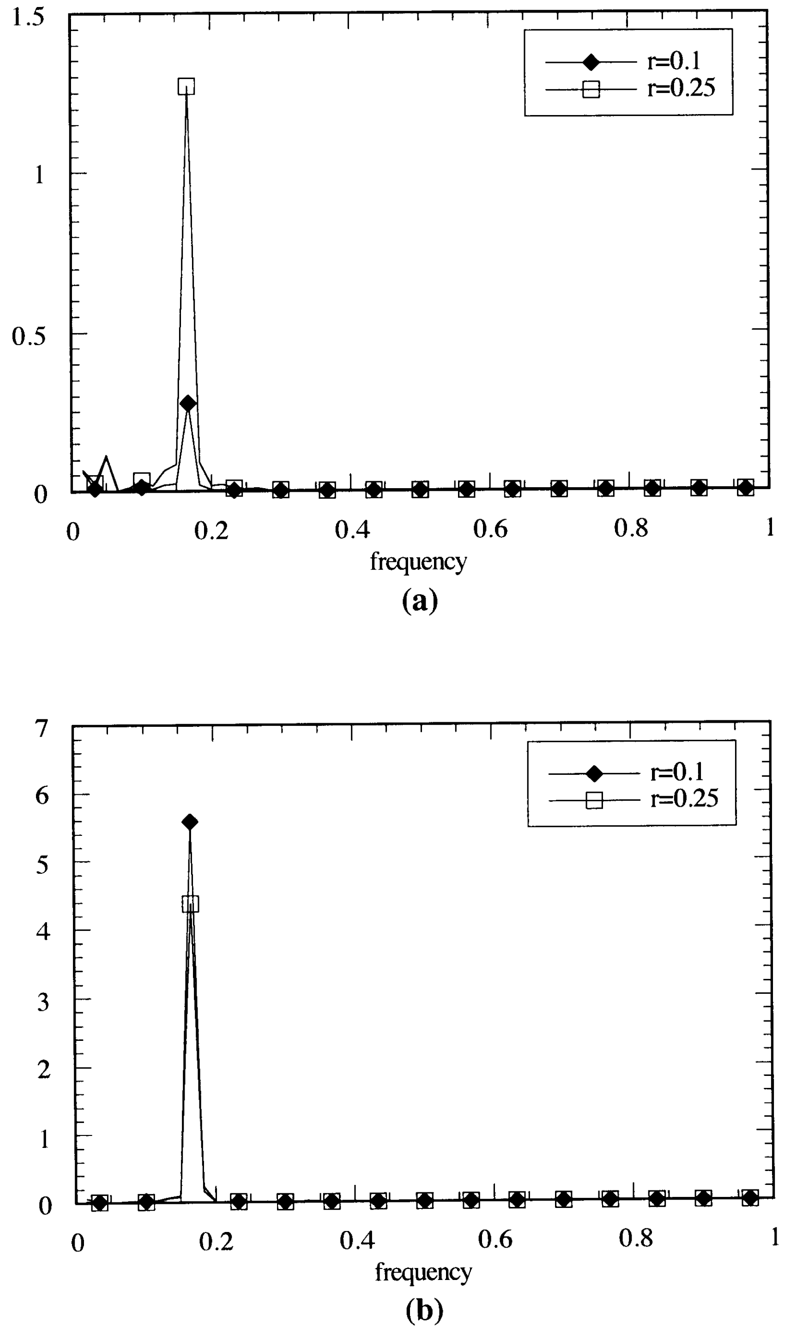

Figure 3.16: Power spectra of the axial (a) and the azimuthal (b) velocity components at two points inside the bubble, downstream from the front stagnation point at an axial location x=11.5 and a radius r=0.1 and r=0.25. Front stagnation point is at x=10.5. (circulation number Ω=3.52)

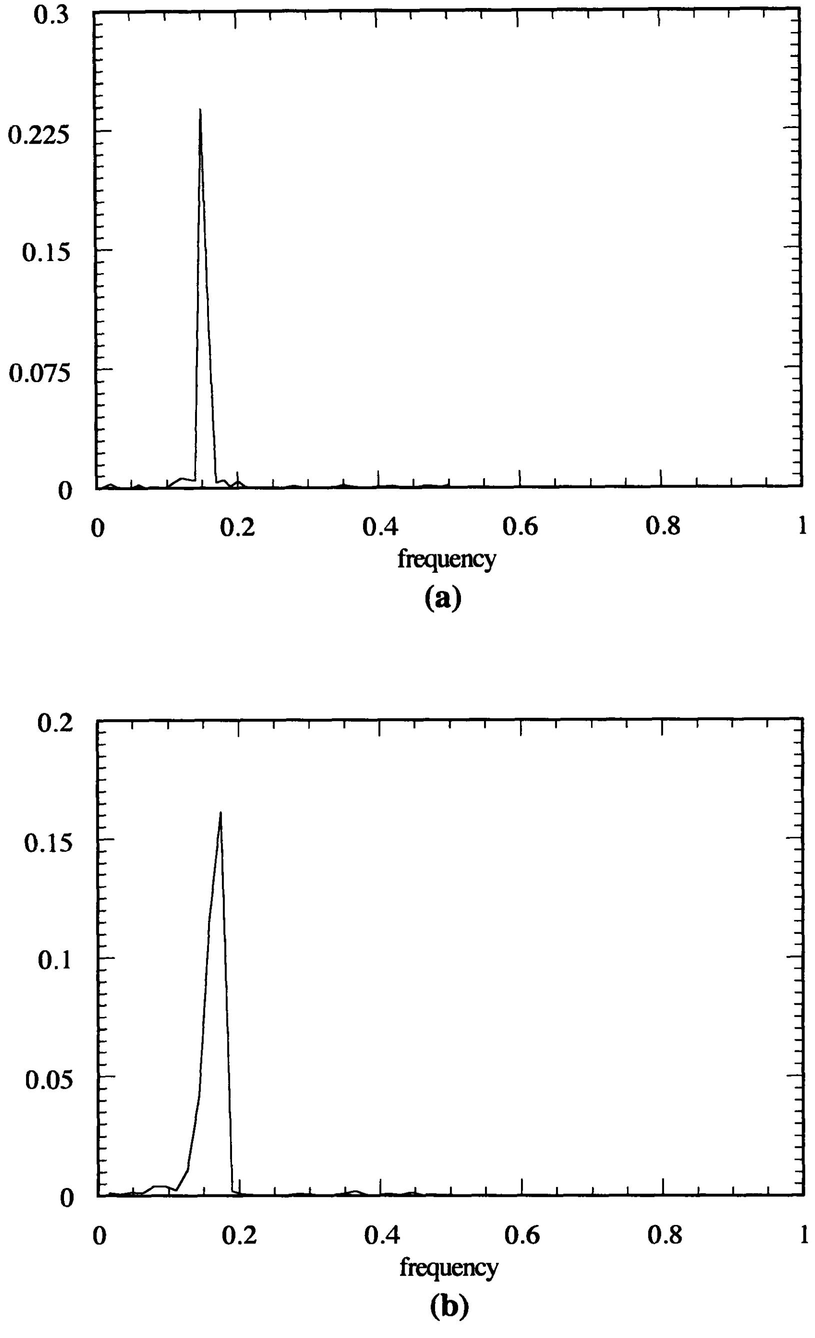

Figure 3.17: Power spectra of the azimuthal velocity fluctuations at the center of the bubble for (a) $\Omega=3.26$, (b) $\Omega=3.77$, and (c) $\Omega=4.27$. The dominant frequencies are 0.154, 0.175, and 0.193 respectively.

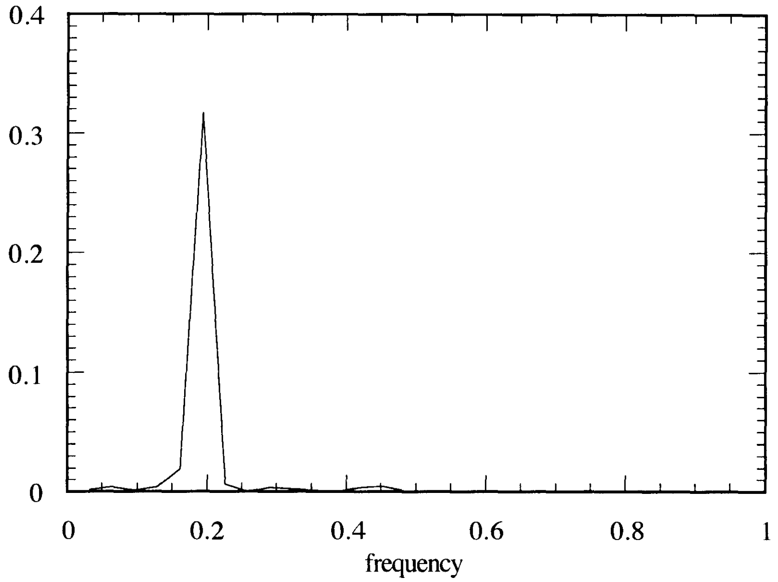

(c)

Figure 3.17: Continued

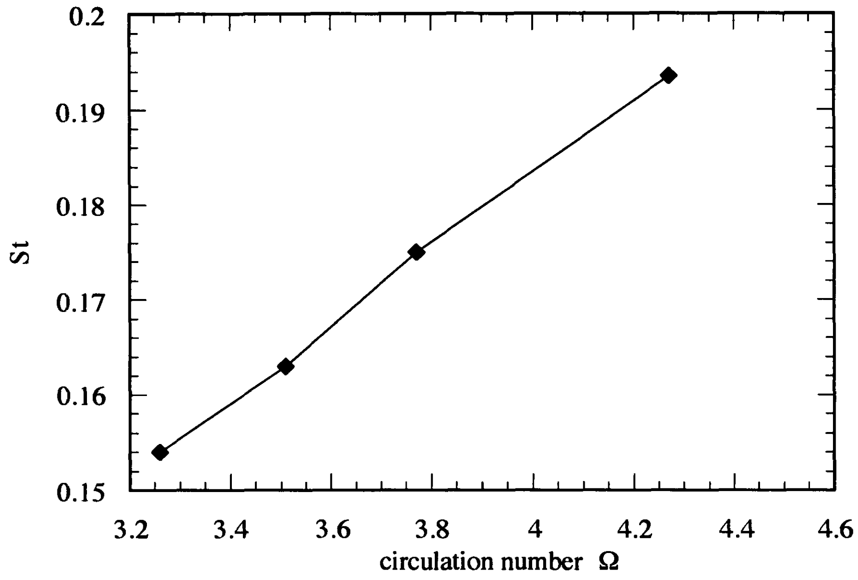

Figure 3.18: Frequency of the azimuthal velocity fluctuations inside the breakdown bubble (Strouhal number) as a function of the circulation number Ω.

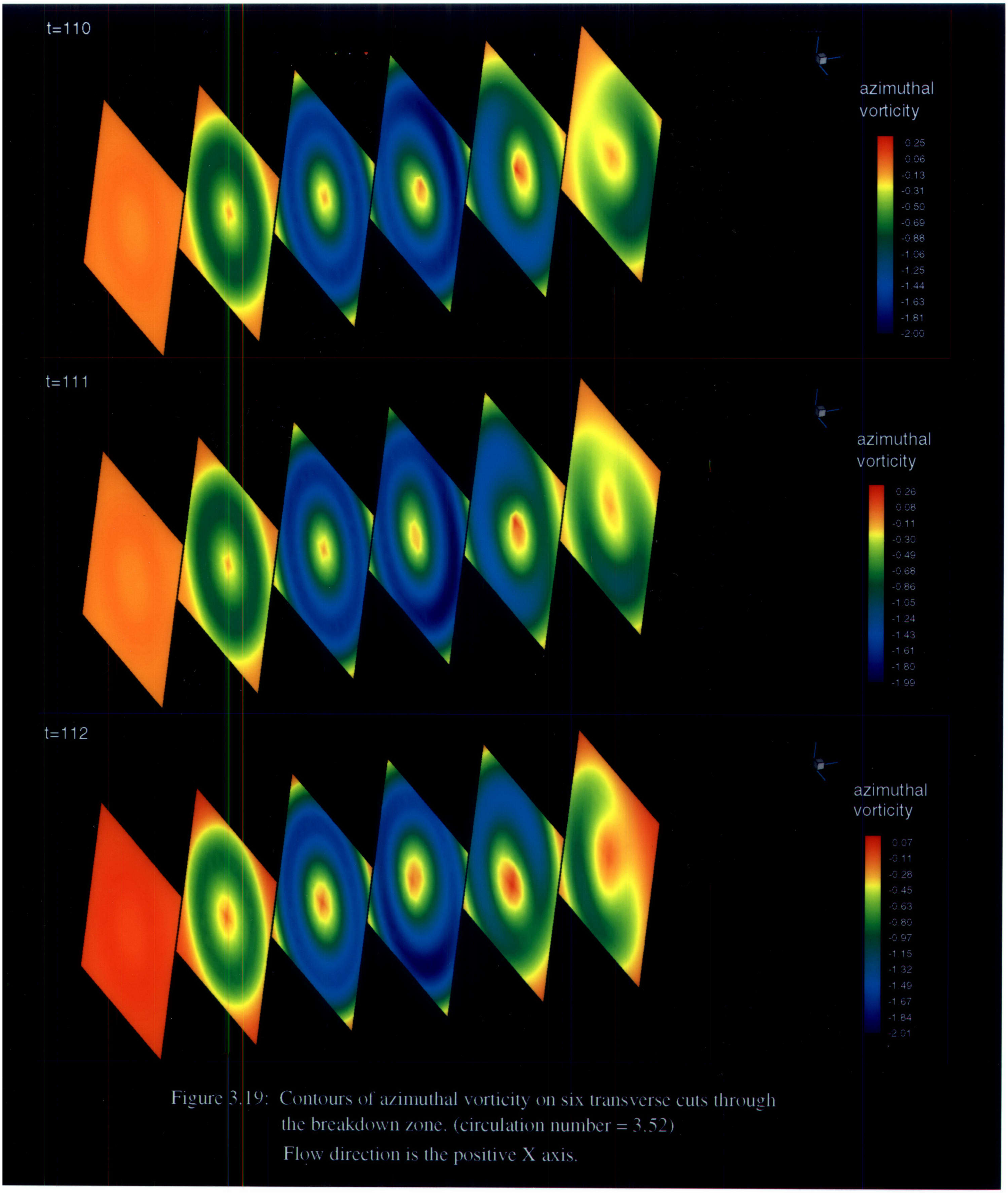

Figure 3.19: Contours of azimuthal vorticity on six transverse cuts through the breakdown zone. (circulation number = 3.52) Flow direction is the positive X axis.

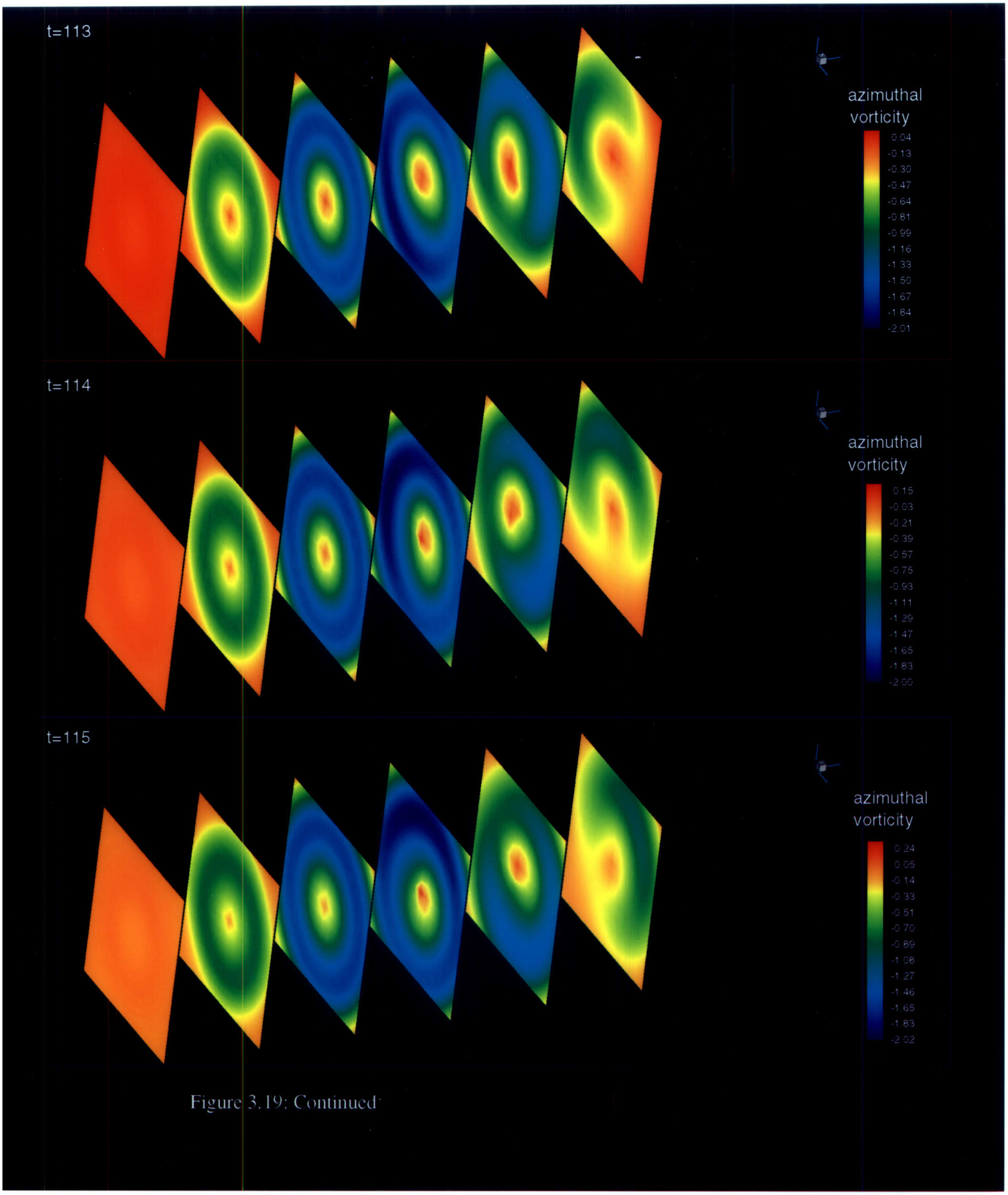

Figure 3.19: Continued

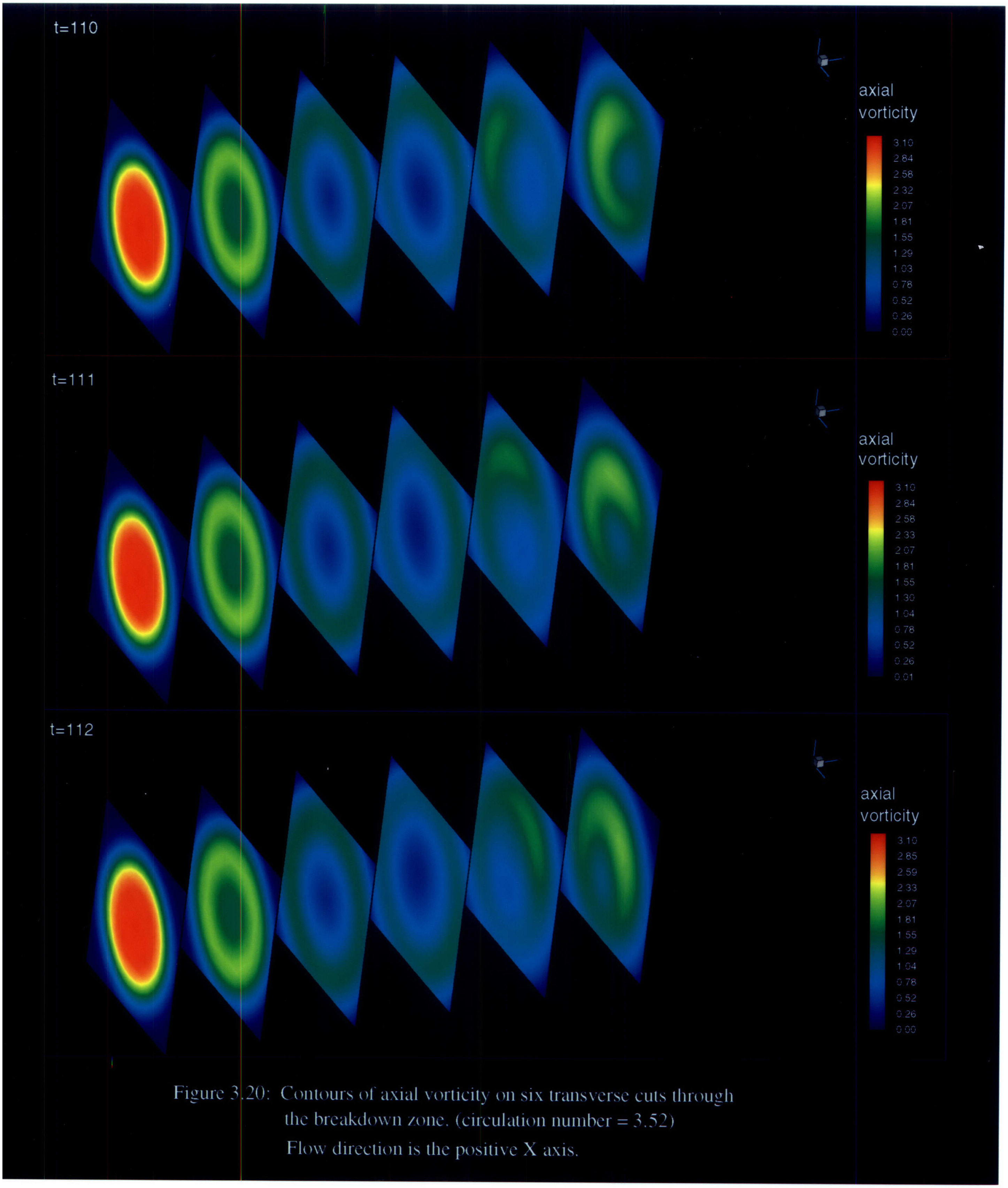

Figure 3.20: Contours of axial vorticity on six transverse cuts through the breakdown zone. (circulation number = 3.52) Flow direction is the positive X axis.

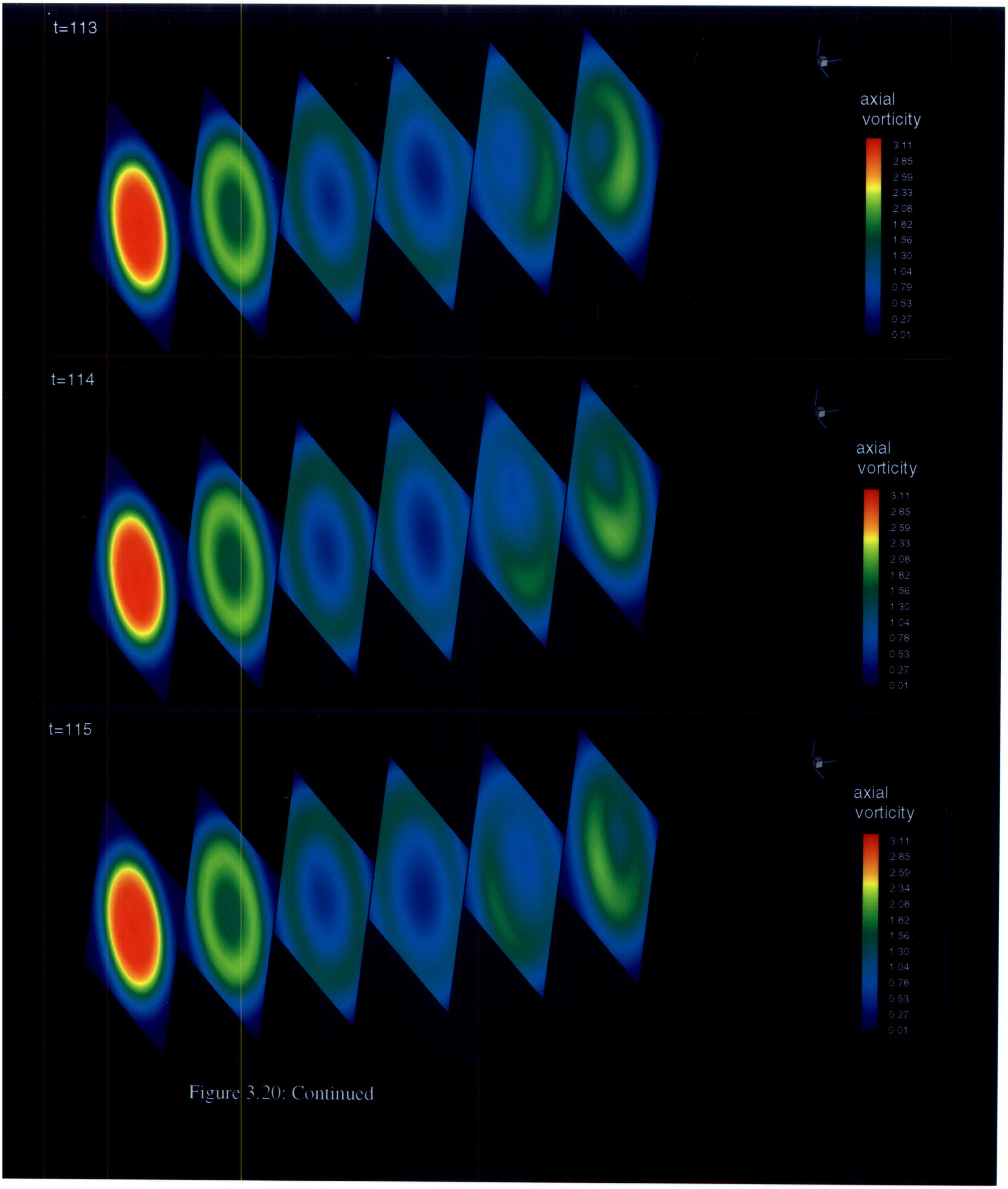

Figure 3.20: Continued

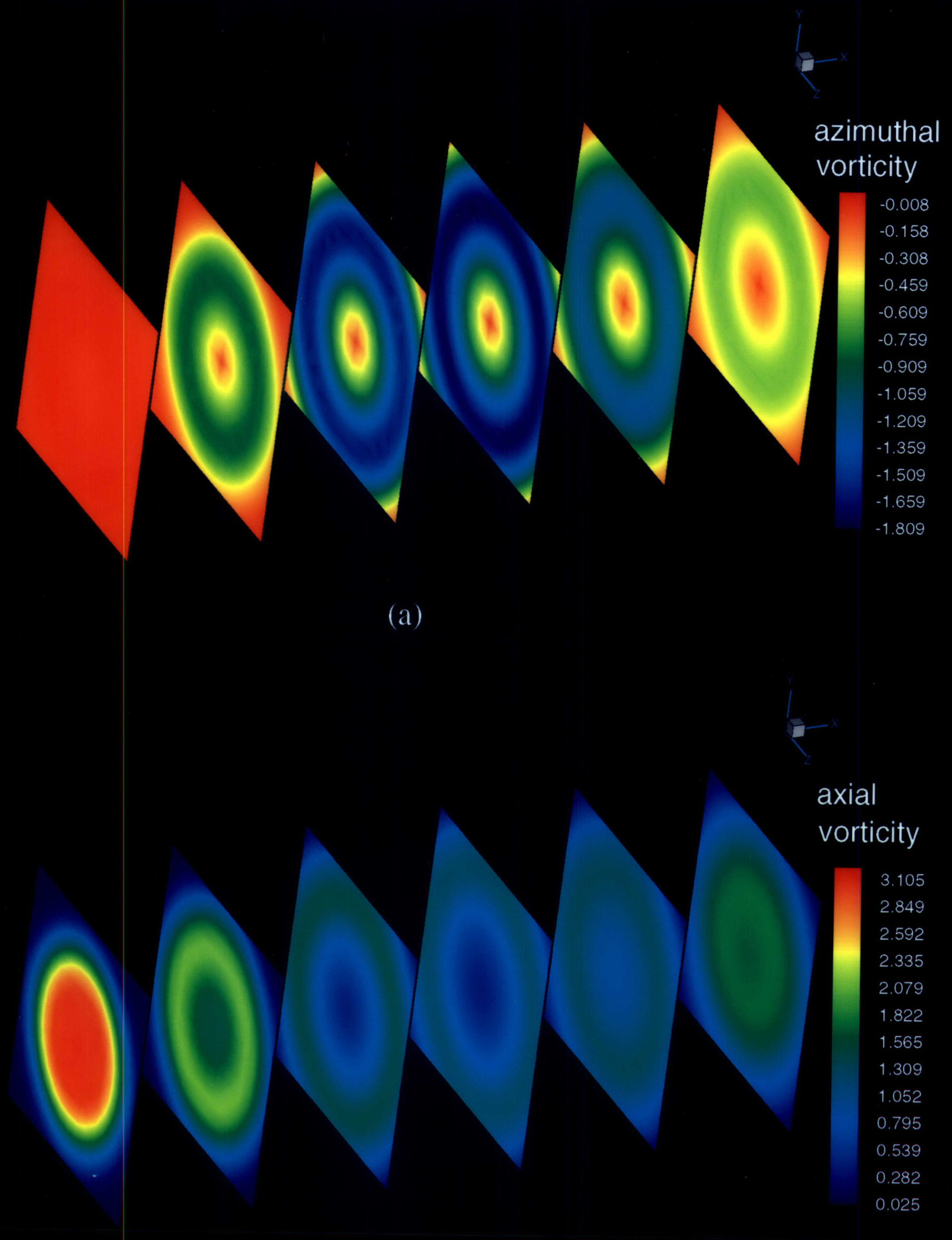

(a)

(b)

Figure 3.21: Time averaged contours of (a) azimuthal and (b) axial vorticity on six transverse cuts through the breakdown zone.

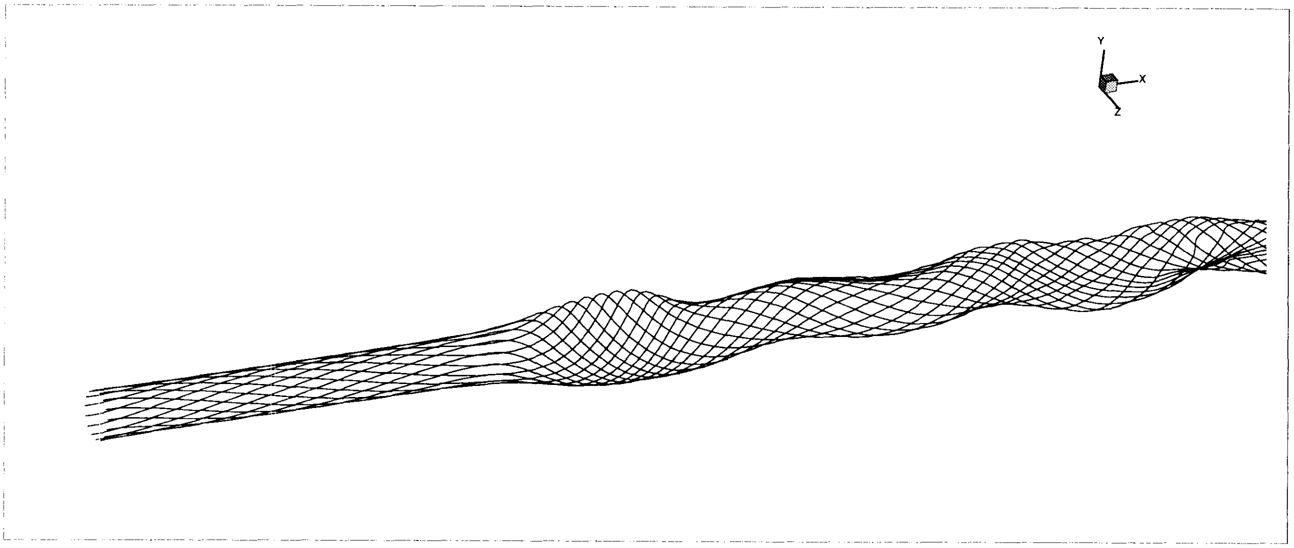

Figure 3.22: Filaments pertaining to the outer outer layer. (t=110)
Flow direction is in the positive X direction.

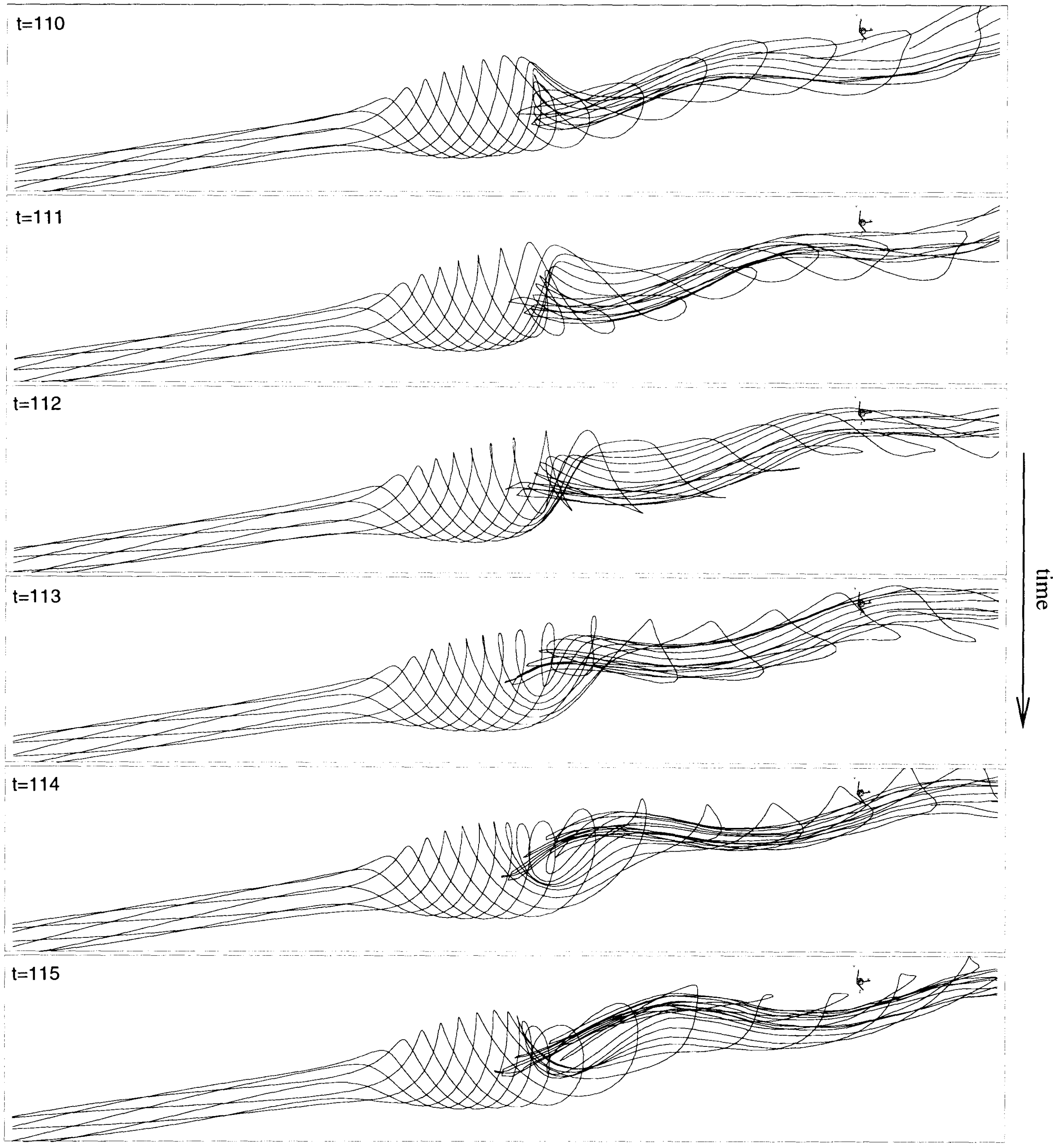

Figure 3.23: Filaments pertaining to the inner layer. Flow direction is in the positive x direction.

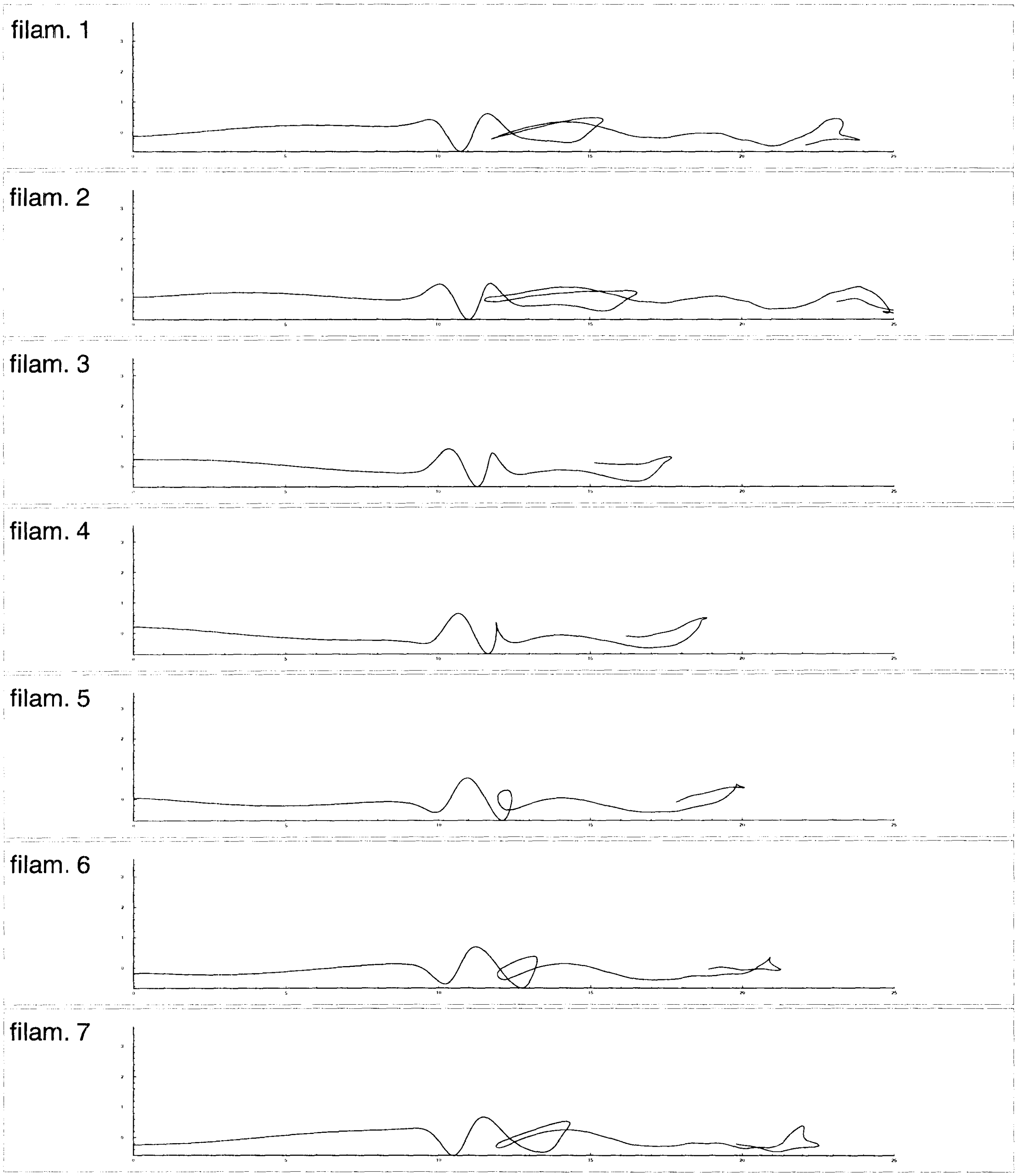

Figure 3.24: Individual vorticity lines forming the inner vorticity layer. (t=110)

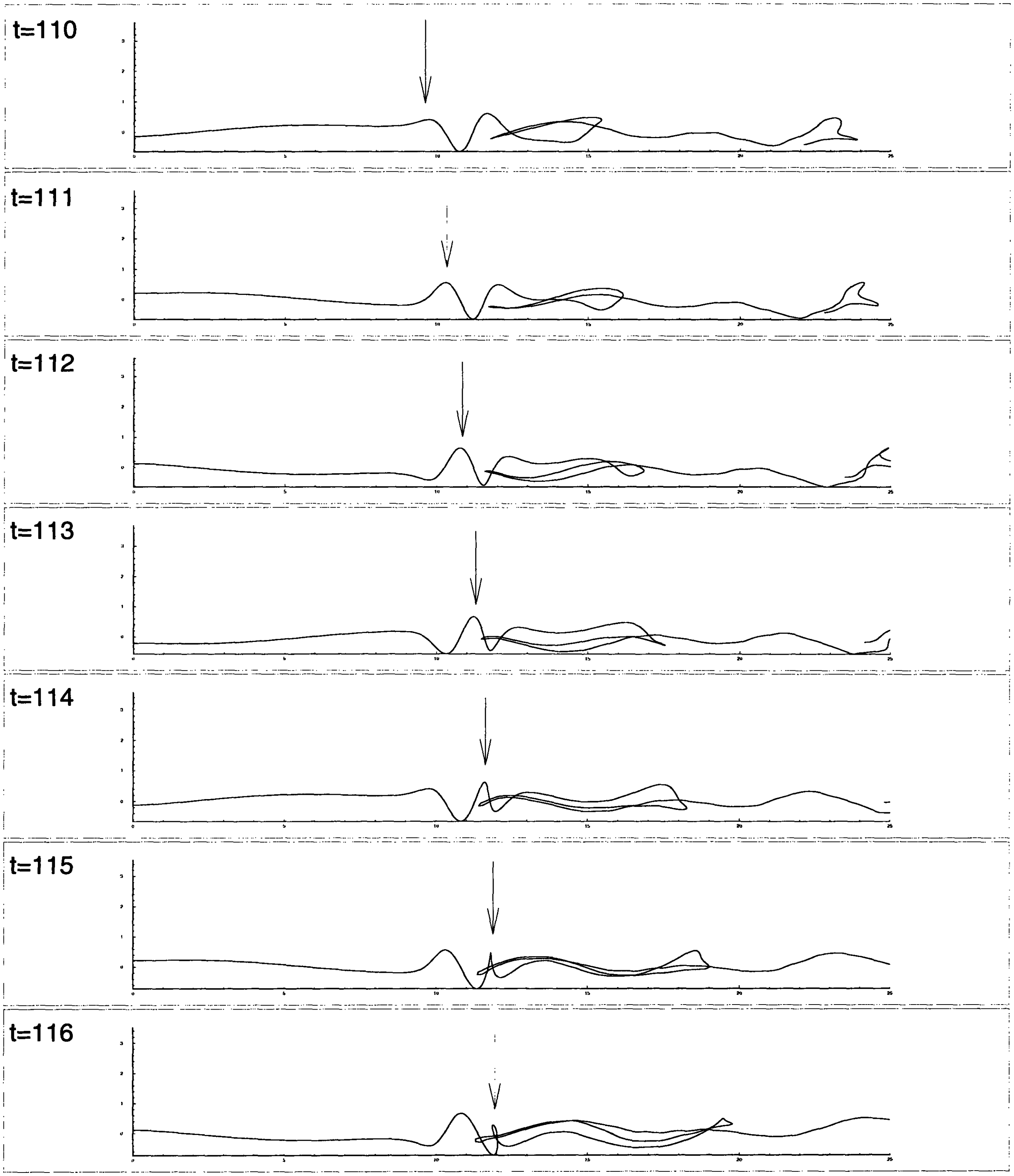

Figure 3.25: Evolution of a filament on the inner vorticity layer.

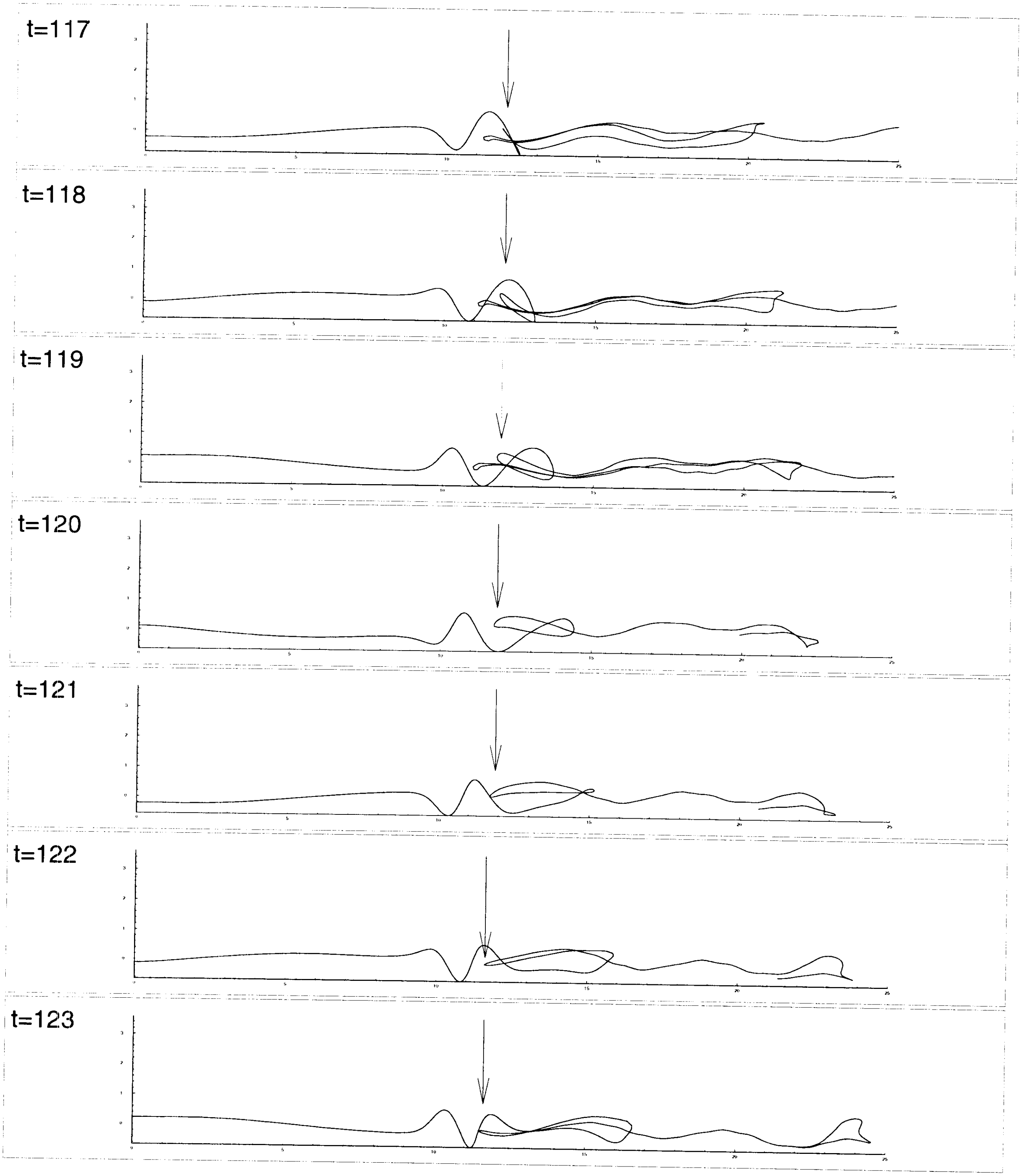

Figure 3.25: Continued

4. Parallel Implementation

4.1 Introduction

There are two main factors responsible for the high computational cost required to model the three dimensional dynamics of the vortex breakdown phenomenon using the vortex element method. The first factor is the $O(N^2)$ nature of the computation. As stated in chapter 2, the evaluation of the vortical component of velocity on N elements, using the Biot-Savart representation (2.15 and 2.20), requires a costly $O(N^2)$ computational effort. The second factor that increases the computational cost is the high strain field that evolves because of the convoluted nature of the breakdown region (figure 1). This evolving strain field continuously stretches the elements unidirectionally along the vorticity lines. In order to maintain the accuracy of the solution, the mesh refinement scheme described in detail in section 2.5, is implemented. It consists of splitting an element in two when its characteristic length $\delta\chi_i$, along the vortex line, exceeds a certain preset value. The objective is to maintain core overlap between neighboring elements, and therefore the "cut-off" value for splitting an element in two is equal to δ, the core radius of the spherical Gaussian distribution of vorticity. Each one of the child elements will have a characteristic length equal to half of the parent element $\delta\chi = \delta\chi_i/2$, and a circulation value equal to that of the parent element. The implementation of this redistribution of the vorticity field makes the rate of increase in the number of elements dN/dt proportional to the number of elements N; which means that N experiences an exponential growth with time as previously shown in figure 2.2.

To avoid this high, and sometimes irrealistic, computational cost; we implement a massively parallel version of the three dimensional vortex element method code. The objective is the reduce the $O(N^2)$ computations to an $O(N^2/npe)$, where npe is the number of processing elements used in the parallel implementation; which means having a smaller constant in front of the quadratic equation, and therefore a lower rate of increase of computational time with N. This solution turns out to be very appealing and efficient because of the inherently parallel nature of the vortical solution of velocity using the Biot-Savart representation. A more elaborate description is given in the next section.

4.2 The CRAY T3D and the Parallel Algorithm

4.2.1 Parallel Architecture and Hardware

The parallel code was developed for the CRAY T3D located at the Pittsburgh Supercomputing Center. One of the main reasons for choosing the T3D is the fact that it is a Distributed Memory machine, as opposed to a Shared Memory one (figure 2). Shared Memory machines, such as the C90 and the KSR-1 can only handle a limited number of processors (16 processors for the C90). They also experience conflicts when many processors share the same bus. Examples of Distributed Memory machines are the CM-2, the CM-5, the T3D, the Paragon, and the SP2. Note that the CM-2 is a Single Instruction Multiple Data (SIMD) machine, while all the others are Multiple Instructions Multiple Data (MIMD). Besides the processor power, the number of processors and the memory available, a very important factor affecting the performance is the network or communication between processors. This latter factor favored the T3D, which offers high bandwidth/low latency communication along with high speed synchronization, or Hardware Barrier, which is done at the hardware level.

The T3D has 512 DEC EV-4 (Alpha) microprocessors in a 3D Torus configuration. Each processors runs at 150 MHz and is theoretically rated at 150 Mflops. Each processing element has 64Mbytes of memory. The memory is physically distributed, but it is logically shared as shown in figure 3. This means that a processor can access a certain variable in memory, without it being necessarily in its own memory. Such access is about an order of magnitude slower than a local memory access, but in this case computational speed is sacrificed for ease of programming. A Global Addressing scheme is used to simulate the Shared Memory feature.

4.2.2 Implementation of the Parallel Algorithm

The purpose of a massively parallel implementation of an algorithm (or code) is to be able to use a large number of processors to simultaneously perform a set of computations in less effective time than a single processor would require. Ideally, the use of *npe* processors in parallel -as opposed to one serial processor- should reduce the effective computational time to *time(npe)=time(1)/npe*, where *time(1)* is the computational time required if the calculation was performed by a single processor. In reality, such parallel algorithms are irrealizable, and we create two variables to help us evaluate the performance of a parallel code. The first variable is the speedup, defined as *speedup=time(1)/time(npe)*, and the second one is the parallel efficiency *%eff=(speedup/npe)*100.00*.

There are three major factors that make a 100% parallel efficiency code not achievable. The first factor is the presence of inherently serial parts of a code, that are not parallelizable. This creates a bottleneck, and as the number of processors increases, the efficiency decreases continuously, while the speedup converges to an asymptotic value. This value is a result of the time consumed by the serial, non parallelizable, part of the code. The second factor that affects the efficiency of a parallel implementation is the load balancing problem. This occurs when the parallel computational load is not evenly distributed between the processors. The consequence is having idle processors at a synchronization barrier, waiting for other processors to finish a certain set of computations. The third and last factor is the communications cost. It is an unavoidable overhead which results from the need for processors to exchange data from their memory. Logically, the more processors there is, the more communication is needed between them; and the time impact of this communication on the overall parallel efficiency of the code increases.

In the massively parallel implementation of the three dimensional vortex element method, most of the parallelization effort is targeted towards the module that calculates the vortical component of the velocity. The velocity at a point **x**, induced by a collection of N vortex elements, each with strength Γ_i and length $\delta\chi_i$, is given by equation (2.20) as

$$\mathbf{u}(\mathbf{x}) = -\sum_{i=1}^{N} \frac{\Gamma_i}{4\pi} \frac{(\mathbf{x}-\mathbf{X}_i) \times \delta\chi_i}{|\mathbf{x}-\mathbf{X}_i|^3} (1-e^{-r^3})$$

where

$$\mathbf{r} = \frac{|\mathbf{x}-\mathbf{X}_i|}{\delta}$$

The velocity module is the most time consuming module taking up more than 95% of the total computational time. It involves an $O(N^2)$ computational effort in the form to two nested Do Loops. In the outer loop (i=1 to Nc) the points will be referred to as field points or active points, while in the inner loop (j=1 to N) they will be referred to as vortex source points. In our implementation, we parallelize the outer loop. The "physically shared logically distributed memory" feature that the T3D offers is not used. Instead, each processor maintains a copy of all the variables loaded in local memory. The approach is called the "Shared Memory" approach because each processing element accesses variables in memory as if it was shared, while in fact all memory accesses are local since all processors have the same copy. Each processor is assigned a different subset of the field points of size *N' =N/npe*. In the outer loop, the processor loops through the *N'* field points and computes the vortical velocity at each one of the points induced by the *N* vortex source points of the inner loop. Since *N'* is the same for all the processors to within one element, the scheme provides good load balancing. As stated previously, the effective computational time is reduced from $O(N^2)$ to $O(N^2/npe)$. The nested Do Loops are free from inter-processor communications, since all memory accesses are local. All the communication is done in a one shot deal at the end of the nested loops. All the processors "broadcast" the data (velocity values) of the field points they worked on, and the memories in the processing elements become identical again, and ready for the next time step. After the massively parallel implementation of the outer loop, the algorithm of the VEM that was presented in section 2.4 becomes the following:

```
(All the processors run simultaneously the same algorithm)
Begin
    Loop j=Ncmin,Ncmax
        $\mathbf{u}(\mathbf{x}_j,t) = -\sum_{i=1}^{N} \frac{\Gamma_i}{4\pi} \frac{(\mathbf{x}_j-\mathbf{X}_i) \times \delta\chi_i}{|\mathbf{x}_j-\mathbf{X}_i|^3} (1-e^{-(\frac{|\mathbf{x}_j-\mathbf{X}_i|}{\delta_i})^3})$
    EndLoop

    Processors exchange updated values of velocity

    Loop j=1,Nc
        $\mathbf{x}_j^* = \mathbf{x}_j(t) + \mathbf{u}(\mathbf{x}_j,t)\,\Delta t$
    EndLoop

    Update the vorticity of the elements

    Loop j=Ncmin,Ncmax
        $\mathbf{u}(\mathbf{x}_j^*,t) = -\sum_{i=1}^{N} \frac{\Gamma_i}{4\pi} \frac{(\mathbf{x}_j^*-\mathbf{X}_i) \times \delta\chi_i}{|\mathbf{x}_j^*-\mathbf{X}_i|^3} (1-e^{-(\frac{|\mathbf{x}_j^*-\mathbf{X}_i|}{\delta_i})^3})$
    EndLoop

    Processors exchange updated values of velocity
```

```
    Loop j=1,Nc
        $x_j(t+\Delta t) = x_j(t) + \frac{u(x_j,t) + u(x_j^*,t)}{2} \Delta t$
    EndLoop

    Update the vorticity of the elements
    $t=t+\Delta t$
Goto Begin
```

Ncmin and *Ncmax* are the minimum and maximum indices of the range of active points a processor operates on in the Biot-Savart calculation of velocity. They are chosen such that the range [1,*Nc*] is equivalent to [*Ncmin(1),Ncmax(1); Ncmin(2),Ncmax(2);* ... *Ncmin(npe),Ncmax(npe)*] and that *Ncmax-Ncmin* on any processor is equal to *Nc/npe* to within one element. This ensures good load balance of the parallel implementation.

This scheme parallelizes more than 95% of the computations. It takes advantage of the inherent parallel nature of the vortex element method for load balancing, and it limits communication to the end of the time step, while keeping all in-loop memory read/write's local and therefore fast. The performance results of the massively parallel implementation as far as speedup, efficiency, and comparison with C90 benchmarks are presented in the next section.

4.3 Performance Results

The T3D massively parallel code, SWIRL, was used in the simulation of the vortex breakdown to produce all the results given in chapter 3. The code was run on 1, 8, 16, 32, 64, and 128 processors for several values of the number of elements *N*. Figure 4.4.a is a plot of the speedup, as defined in section 4.2.2, versus the number of processing elements, for different values of the number of computational elements. One of the lines on the graph is an ideal speedup curve whose slope is equal to unity. In all cases the speedup is approximately linear, and as the number of elements increases, the speedup curves approach the ideal one. For example, using 128 processors and running the simulation with 15,000 computational elements, results in a speedup of 126.7. The parallel efficiency curves shown in figure 4.4.b, indicate that as the number of elements increases, the efficiency approaches more and more the ideal (100%) line. At 15000 elements, a remarkable 98.7% efficiency is obtained with a 128 processor run. This graph also shows that an increase in the number of processors for a fixed number of computational elements produces a decrease in parallel efficiency.

Figure 4.5 is a comparison in required computational time between the CRAY C90 and the T3D, with the number of processors ranging between 8 and 128 processors. As expected, the elapsed run time increases as the square of the number of elements for both the C90 and the T3D. The break-even point between the Vector implementation on the C90 and the Massively parallel implementation on the T3D is at exactly 16 processors. With a higher number of processors, the "elapsed time" versus "number of elements" curve is still a quadratic but with a smaller constant, which results in a lower rate of increase of computational time with N. Thus, the benefit of a parallel implementation over a serial implementation is higher for a large number of computational elements.

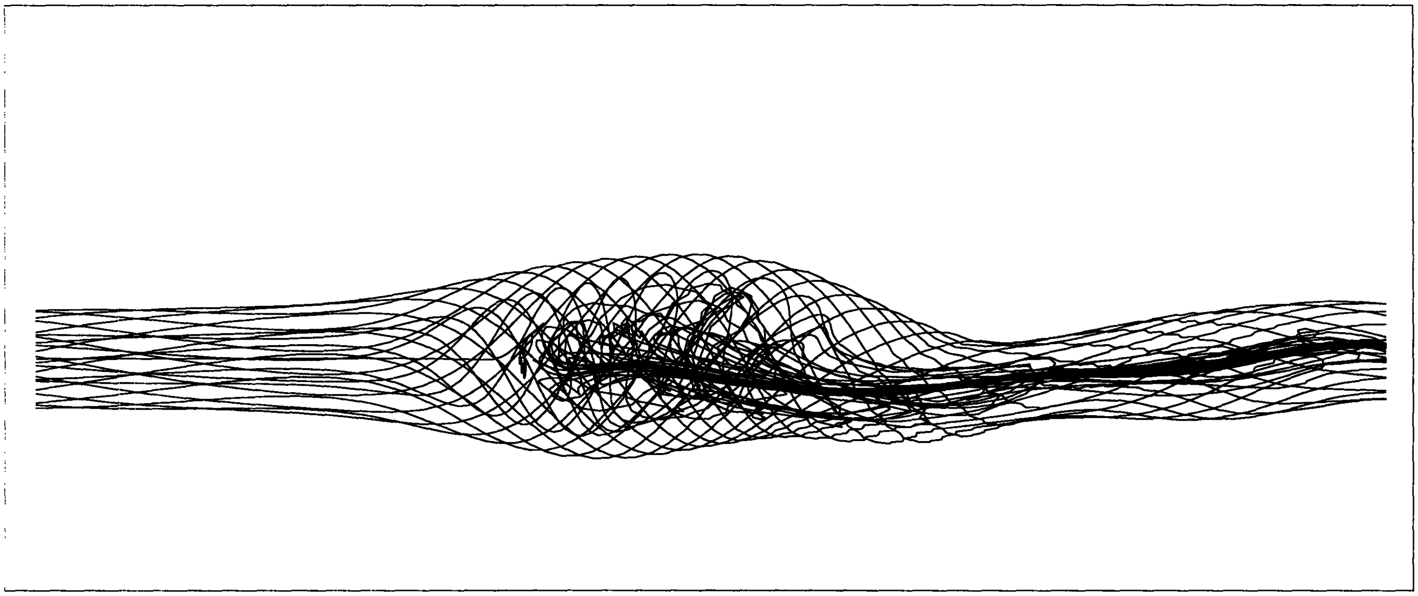

Figure 4.1: Close-up on the breakdown bubble, showing its highly convoluted nature.
Circulation number = 3.52, t=25.0

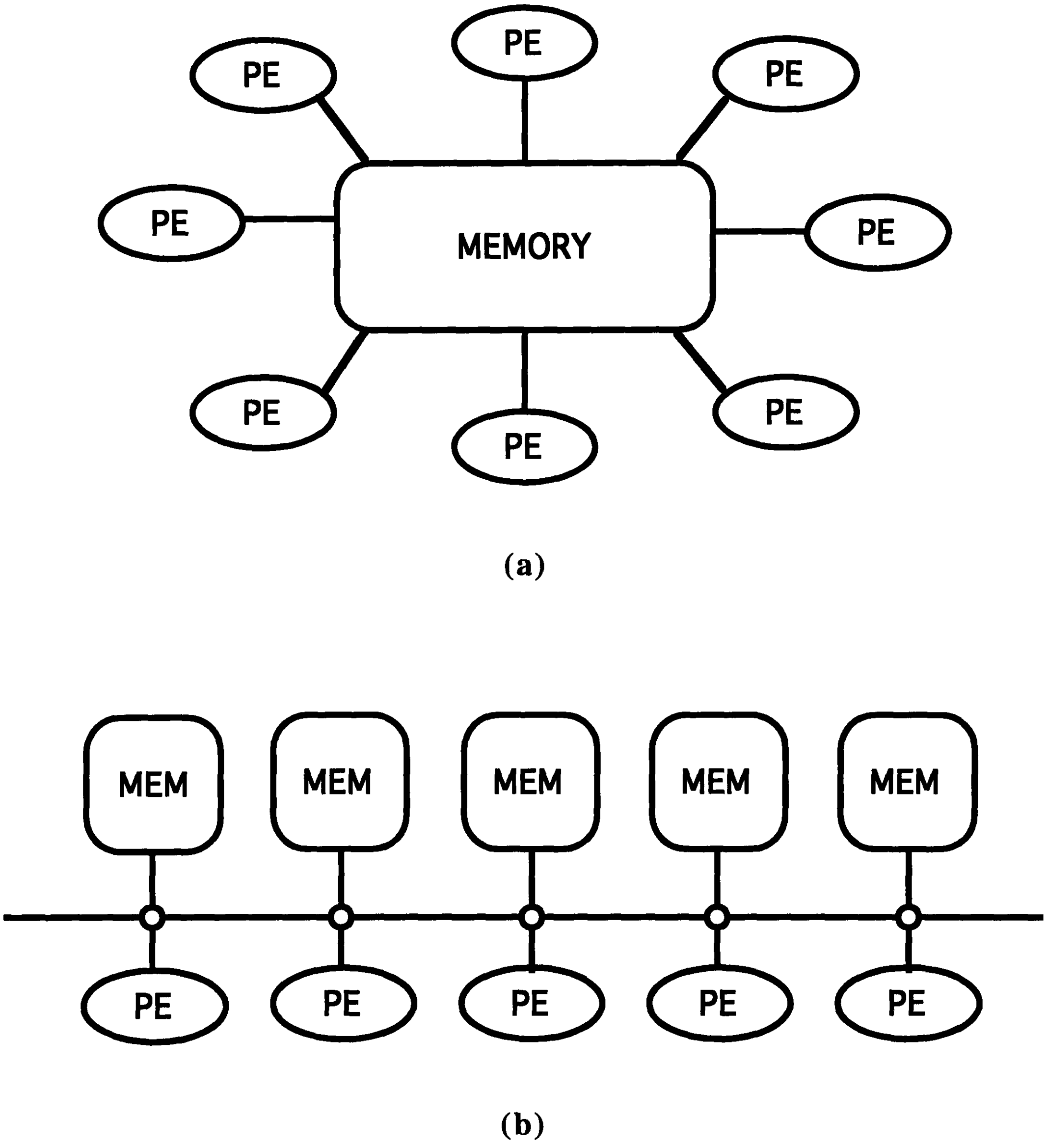

Figure 4.2: Schematic diagram of two different types of parallel architectures.
a) Shared memory.
b) Distributed memory.
(PSC Supercomputing Techniques)

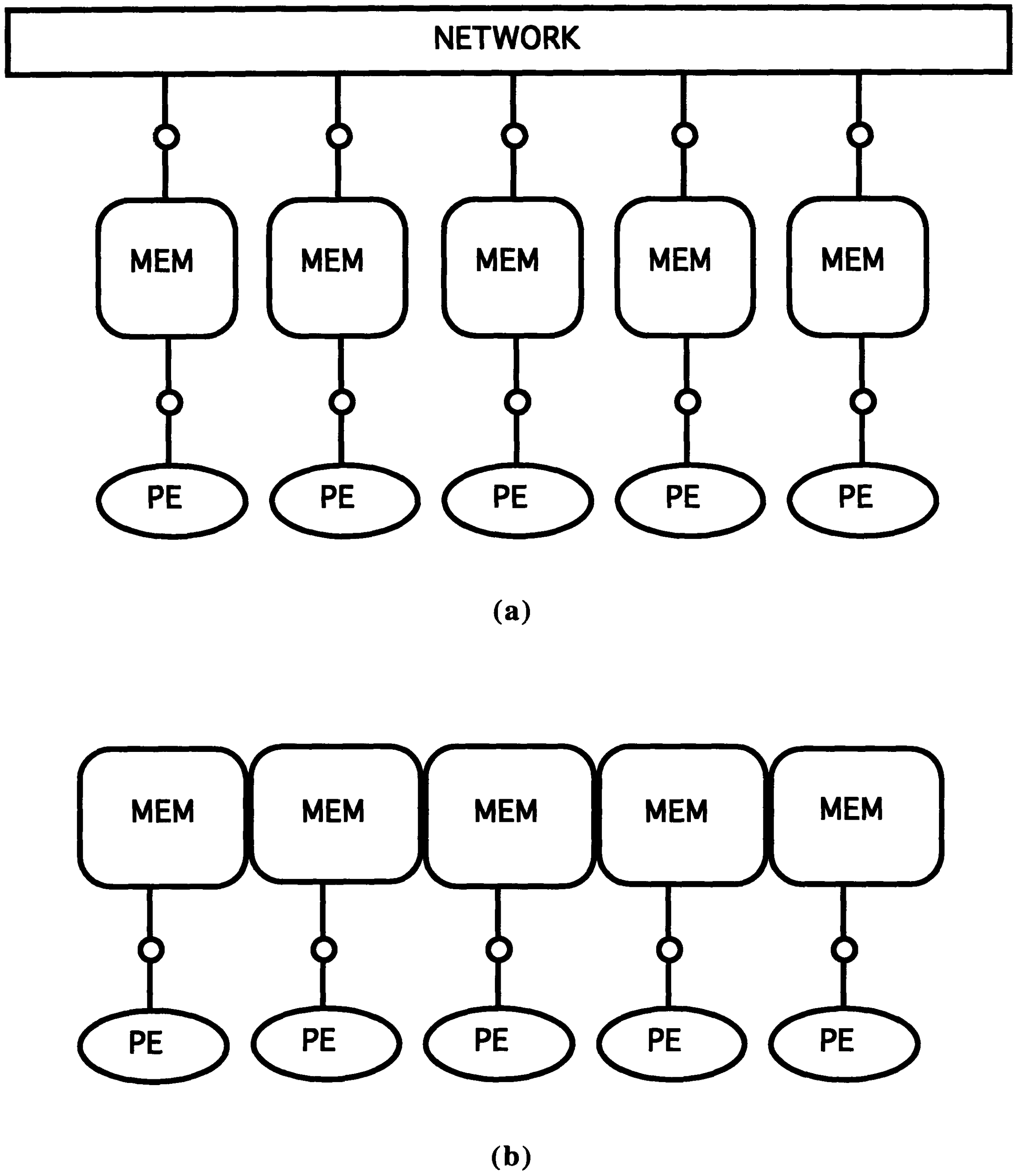

Figure 4.3: Schematic diagram showing a Physically Distributed (a) and Logically Shared (b) memory configuration. (PSC Supercomputing Techniques)

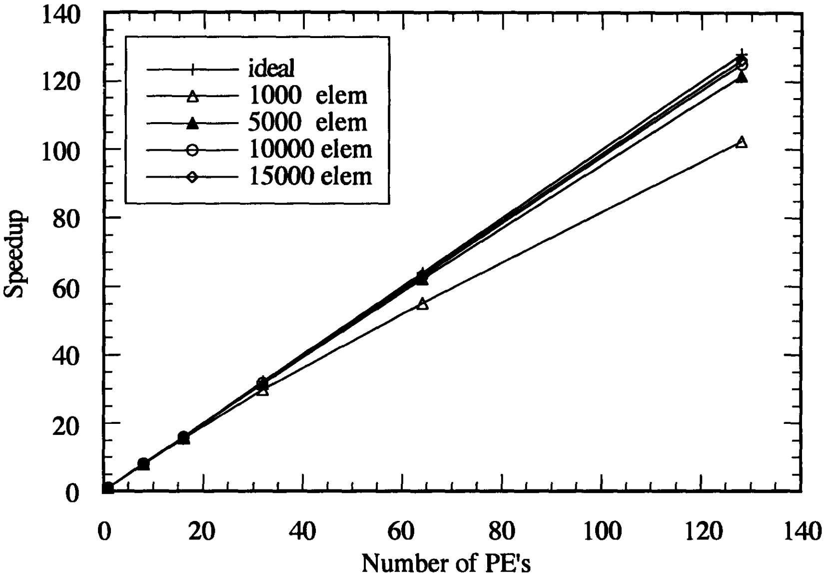

(a)

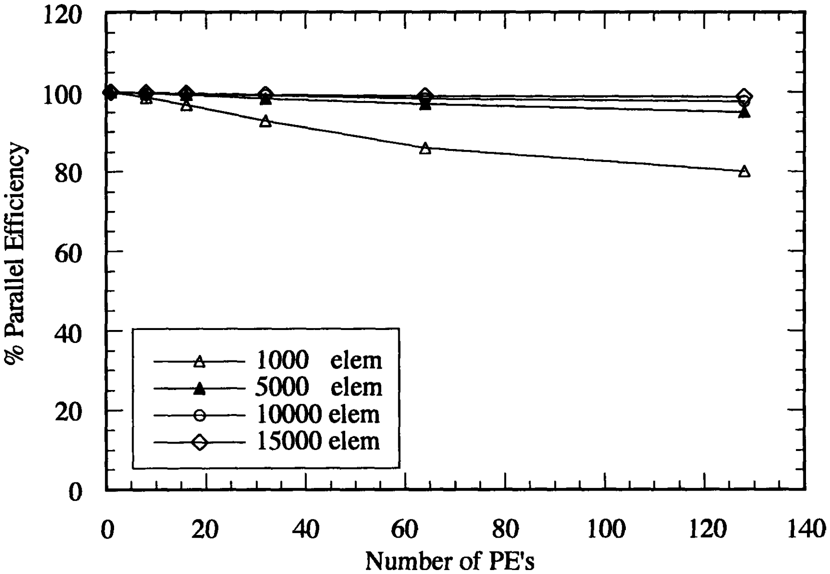

(b)

Figure 4.4: Performance evaluation of the massively parallel implementation of the Vortex Element Method for several values of the number of computational elements.

a) Speedup as a function of the number of processors.

b) Efficiency as a function of the number of processors.

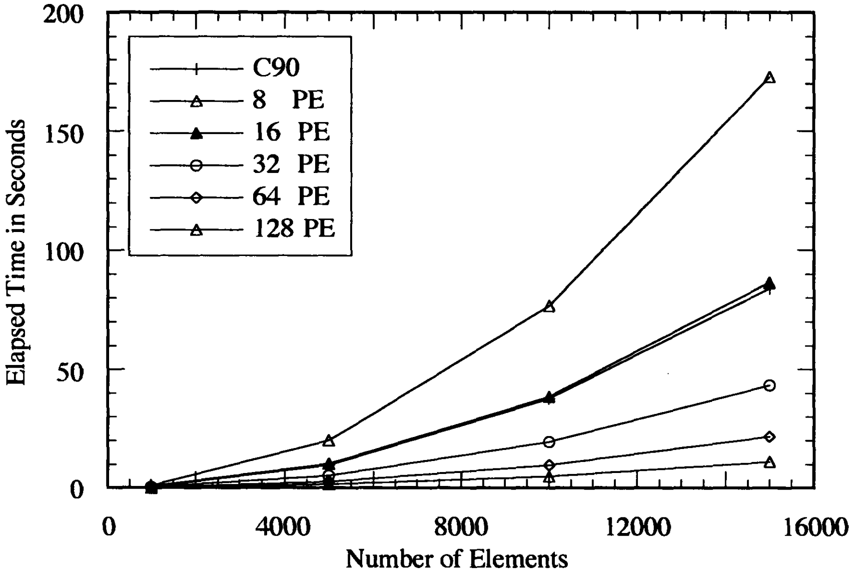

Figure 4.5: Comparison between the performance of the C90 and the performance of the T3D.

5. Conclusion

A massively parallel high efficiency implementation of the three-dimensional vortex element method was developed to study the dynamics of vortex breakdown in swirling flows. Several runs were performed to simulate the breakdown of an axial vorticity core and the following characteristics of the breakdown region were analyzed: the recirculating nature of the flow; the spiraling of the vorticity filaments; the filling and emptying of the breakdown zone; the dependence of the flow on the circulation number; the axial and azimuthal velocity profiles across the entire flow region; and finally the internal structural and velocity fluctuations of the breakdown. The internal vorticity field was also three-dimensionally mapped and examined in conjunction with the discrete vorticity field represented by the filaments. Using the obtained results and their analysis, a hypothesis was formulated explaining the fundamental dynamics behind the existence of the breakdown along with a discussion on the observed asymmetric features and the extent of their importance in fundamentally affecting the flow behavior.

Some forty years after the first reported incident of vortex breakdown, this phenomenon is unfortunately still surrounded by misconceptions and contradicting theories. This work has helped in providing a solid explanation to the vorticity dynamics involved in the formation and stability of the breakdown, and in shedding some light on the dynamics behind some reported experimental observations; but it has fell short of providing a definite explanation for the onset of breakdown in an initially breakdown-free swirling flow. This unresolved question will be addressed in future work along with a comparative study between the bubble type and the spiral type breakdown. The goal behind this study is to reach a final conclusion regarding the visual differences observed and whether or not the two phenomenas are fundamentally governed by the same dynamics.

REFERENCES

1. Althaus, W. And Krause, E., Progress Report, EC Contract SC1-0212, 1990.
2. Batchelor, G. K., An introduction to Fluid Dynamics, Cambridge University Press, Cambridge, 1967.
3. Benjamin, T. B., Journal of Fluid Mechanics, **14**, 593 (1962).
4. Chorin, A. J., Journal of Fluid Mechanics, **57**, 785 (1972).
5. Chorin, A. J., Journal of Computational Physics, **27**, 428 (1978).
6. Brown, G. L. And Lopez, J. M., Journal of Fluid Mechanics, **221**, 553 (1990).
7. Brucker, C. and Althaus, W., Experiments in Fluids, **13**, 339 (1992).
8. Brucker, C., Experiments in Fluids, **14**, 133 (1993).
9. Bruer, M., Hanel, D., Kloker, J. and Meinke, M., Computer Fluids, **22**, 229 (1993).
10. Bruer, M., Hanel, D., Computer Fluids, **22**, 467 (1993).
11. Bushnell, D. M, Aeronautical Journal, 293 (Oct 1992).
12. Elle, B. J., J. R. Aero. Soc., **64(596)**, 491 (1960).
13. Escudier, M. P., Bornstein, J. And Zehdner, N., Journal of Fluid Mechanics, **98**, 49 (1980).
14. Escudier, M. P. and Zehdner, N., Journal of Fluid Mechanics, **115**, 105 (1982).
15. Escudier, M., Progress in Aerospace Science, **25**, 189 (1988).
16. Faler, J. H. and Leibovich, S., Physics of Fluids, **20**, 1385 (1977).
17. Faler, J. H. and Leibovich, S., Journal of Fluid Mechanics, **86**, 313 (1978).
18. Garg, A. K. and Leibovich, S., Physics of Fluids, **22**, 2053 (1979).
19. Althaus, W., Brucker, C. And Weimer, M., "Breakdown of Slender Vortices", Fluid Vortices, Green, S., eds., Kluwer Academic Publishers, Dordrecht, 1995.
20. Gupta, A. K., Lilley, D. G., and Syred N., Swirl Flows, Abacus Press, Kent, 1984.
21. Hall, M. G., Annual Review of Fluid Mechanics, **4**, 195 (1972).
22. Howard, L. N. And Gupta, A. S., Journal of Fluid Mechanics, **14**, 463 (1962).

23. Knio, O. M., Ph.D. Thesis, Massachusetts Institute of Technology, Cambridge MA, 1991.
24. Knio, O. M. And Ghoniem, A. F., Journal of Computatiuonal Physics, **97**, 172, (1991).
25. Knio, O. M. And Ghoniem, A. F., Journal of Fluid Mechanics, **243**, 353, (1992).
26. Lambourne, N. C., and Bryer, D. W., Aeronautical Research Council, Reports and Memoranda No. 3282, 1961.
27. Leibovich, S., Annual Review of Fluid Mechanics, **10**, 221 (1978).
28. Leibovich, S., AIAA Journal, **22**, 1192 (1983).
29. Leonard, A., Annual Review of Fluid Mechanics, **17**, 523 (1985).
30. Leonard, A., and Chua, K., Physica D, **37**, 490 (1989).
31. Ludwieg, H., Z. Flugwiss, **10**, 242 (1062).
32. Menne, S., AIAA Paper 88-0506.
33. Peake, D. J. And Tobak, M., AGARD CP 342, 1983.
34. Peckham, D. H., and Atkinson, S. A., A. R. C. Technical Report C. P. No. 508, 1957.
35. Randall, J. D. And Leibovich, S., Journal of Fluid Mechanics, **53**, 495 (1973).
36. Rosenhead, Proceedings of the Royal Society (London), **A134**, 170 (1931).
37. Sarpkaya, T., Journal of Fluid Mechanics, **45**, 545 (1971).
38. Sarpkaya, T., AIAA Journal, **12**, 602, (1974).
39. Sherman, F. S., Viscous Flow, McGraw-Hill Publishing Company, New York, 1990.
40. Spall, R. and Gatski, T., AIAA Paper 90-1624.
41. Squire, H. B., Aero. Dept., Imperial College, London, Rep. 102, 1960.
42. Werle, H. La Recherche Aeronautique, **74**, 23 (1960).